Coil Performance Evaluation Based on Electrodynamics: Tools for Hardware Design and Validation in Magnetic Resonance Imaging

by

Riccardo Lattanzi

Laurea, Electronic Engineering
University of Bologna (Italy), 2000
S.M., Electrical Engineering and Computer Science
Massachusetts Institute of Technology, 2006

SUBMITTED TO THE HARVARD-MIT DIVISION OF HEALTH SCIENCES AND TECHNOLOGY IN PARTIAL FULFILLMENT OF THE REQUIREMENTS FOR THE DEGREE OF

DOCTOR OF PHILOSOPHY IN ELECTRICAL AND MEDICAL ENGINEERING
AT THE
MASSACHUSETTS INSTITUTE OF TECHNOLOGY

SEPTEMBER 2008

Signature of Author:

Harvard-MIT Division of Health Sciences and Technology
July 18, 2008

Certified by:

Daniel K. Sodickson, M.D., Ph.D.
Associate Professor of Radiology, Physiology & Neuroscience
Director, Center for Biomedical Imaging
New York University Medical Center
Thesis Supervisor

Accepted by:

Martha L. Gray, Ph.D.
Edward Hood Taplin Professor of Medical and Electrical Engineering
Director, Harvard-MIT Division of Health Sciences and Technology

Coil Performance Evaluation Based on Electrodynamics: Tools for Hardware Design and Validation in Magnetic Resonance Imaging

by

Riccardo Lattanzi

Submitted to the Harvard-MIT Division of Health Sciences and Technology
on July 18, 2008 in Partial Fulfillment of the
Requirements for the Degree of
Doctor of Philosophy in Electrical and Medical Engineering

ABSTRACT

Parallel MRI techniques allow acceleration of MR imaging beyond traditional speed limits. In parallel MRI, radiofrequency (RF) detector coil arrays are used to perform some degree of spatial encoding which complements traditional encoding using magnetic field gradients. As the acceleration factor increases, coil design becomes critical to the overall image quality. The quality of a design is commonly judged on how it compares with other coil configurations. A procedure to evaluate the absolute performance of RF coil arrays is proposed. Electromagnetic calculations to compute the ultimate intrinsic signal-to-noise ratio (SNR) available for any physically realizable coil array are shown, and coil performance maps are generated based on the ratio of experimentally measured SNR to this ultimate intrinsic SNR.

Parallel excitation, which involves independent transmission with multiple RF coils distributed around the body, can be used to improve the homogeneity of RF excitations and minimize the RF energy deposited in tissues - both critical issues for MRI at high magnetic field strength. As its use is explored further, it will be important to investigate the intrinsic constraints of the technique. We studied the trade-off between transmit homogeneity and specific absorption rate (SAR) reduction with respect to main magnetic field strength, object size and acceleration. We introduced the concept of ultimate intrinsic SAR, the theoretical smallest RF energy deposition for a target flip angle distribution, and we calculated the corresponding ideal current patterns. Knowledge of these optimal current patterns will serve as an important guide for future high-field coil designs.

Thesis Supervisor: Daniel K. Sodickson, M.D., Ph.D.
Title: Associate Professor of Radiology, Physiology & Neuroscience,
New York University Langone Medical Center

Thesis Committee: Elfar Adalsteinsson, Ph.D.
Title: Associate Professor, Department of Electrical Engineering and Computer Science, Harvard-MIT Division of Health Sciences and Technology, MIT

Thesis Committee: Aaron K. Grant, Ph.D.
Title: Instructor in Radiology, Harvard Medical School

Thesis Committee: Yudong Zhu, Ph.D.
Title: Senior Research Scientist, GE Global Research

Thesis Committee: Fa-Hsuan Lin, Ph.D.
Title: Assistant Professor in Radiology, Harvard Medical School

Biographical Note

I was born on December 22nd, 1975 in Porto San Giorgio, Italy and I grew up in Porto Sant'Elpidio, a small town on the Italian Adriatic coast. After primary and secondary school in my hometown, I attended the scientific high school "*Liceo Scientifico Temistocle Calzecchi Onesti*", in Fermo, Italy, from which I received the "*maturità*" in 1994. I spent one academic year as an exchange student at Enid high school, in Oklahoma, from which I graduated as well in 1993.

From 1994 to 2000 I studied electronics engineering at the University of Bologna, specializing also in biomedical engineering. My "*laurea*" thesis was entitled "Evaluation of the effectiveness and the usability of a multimodal user-interface for a surgical simulator for orthopaedic surgery" and the research work was carried out at the Laboratory for Medical Technology (LTM) of the Rizzoli Orthopaedic Institutes (IOR), under the supervision of Prof. Angelo Cappello and Dr. Marco Viceconti.

From 2001 to 2003 I worked as a research scientist at LTM, on a project aimed to develop an innovative software for preoperative planning of total hip replacement surgery. From September 2002 to March 2003 I was a visiting Fulbright scholar at the Medical Robotics and Computer Assisted Surgery (MRCAS) laboratory of Carnegie Mellon University, in the group of Dr. Branislav Jaramaz.

In 2003 I started a Ph.D. program, of which this thesis is the culmination, in medical engineering and medical physics at the Harvard-MIT Division of Health Sciences and Technology (HST). In January 2004 I began working as a research assistant in the

group of Dr. Daniel Sodickson in the Radiology Department of the Beth Israel Deaconess Medical Center (BIDMC) in Boston. In 2006 I obtained a Master of Science degree from the Department of Electrical Engineering and Computer Science (EECS) at MIT, with a thesis entitled "Radiofrequency detector coil performance maps for parallel MRI applications".

In the past years I was awarded a Spinner scholarship from the Emilia Romagna region, a Fulbright scholarship from the Italian Fulbright Commission and the first prize in the abstract competition at the 2nd conference on biotechnologies and bioengineering (BIONOVA 2001) in Padova, Italy. In 2008, at the 16th annual meeting of the International Society for Magnetic Resonance in Medicine (ISMRM) in Toronto, I was awarded the I. I. Rabi Young Investigator Award based on my work on "Electrodynamic constraints on homogeneity and RF power deposition in multiple coil excitations".

I am a member of the ISMRM and the Institute of Electrical and Electronics Engineers (IEEE). In 2006 I was elected member of the Sigma-Xi scientific research honor society and since 2008 I am an Aspen Junior Fellow of the Aspen Institute Italia.

I currently live in Cambridge, Massachusetts, with my wife and daughter.

Acknowledgements

Looking at this acknowledgements page, the last page of my thesis to be completed, brings back many memories about the past five years that I have spent in Cambridge. I remember arriving on a hot summer day and wandering around with a completely lost taxi driver, looking for the apartment that was waiting for Marta and me in Somerville. We were so excited for the beginning of this new adventure! It has been a wonderful journey, with its difficult days, but mostly full of great moments that I shared with extraordinary people. I wish to begin by expressing my greatest gratitude and love to my wife Marta, for her continuous support in these years. Almost all our life together is framed with the colors of New England, and Boston will always stay in our hearts after the birth of our daughter Beatrice here last year.

I am grateful to my parents, who taught me the values that have guided me throughout my life. My mom Marisa has raised me to be tolerant and open-minded — useful attributes that have helped me living in different places around the World. There is one episode about my dad Renato which I must recall here. He was showing me the encyclopedia of science and technology he had recently bought and he told me to work hard in school, so that one day I would go to MIT. I was about ten years old and he never mentioned MIT again, but it is incredible how those words stuck with me and probably steered my unconscious. I cannot forget to thank my brother Gianluca, who has been my best friend and has always been sincerely proud of what I was doing. I have missed him a lot in these years.

Special thanks go to my in-laws, Mario and Gabriella, who have lived in Cambridge in the past and have always understood what Marta and I were doing here. My brother-in-law Pierfrancesco's recommendations about fast food restaurants were particularly precious in the first year...then I took some medical courses and I learned about cholesterol!

I must spend a few words about Marco Viceconti, who had been my advisor for almost four years before I arrived in Cambridge, and who has been a good friend since the day we met. Thanks to him I fell in love with research, and if it were not for the work I did with him I would have never come to MIT.

I do not know what the likelihood is, but I have been blessed twice in a row in the choice of supervisors. I remember when Daniel Sodickson presented his research projects during an HST seminar and concluded by mentioning he was looking for students. I had been captivated by his talk and I sent him an email the same evening. A few days later I was in his office discussing my CV and I was lucky to become his student. I owe to him most of what I have learned about MRI, but he has been more than a supervisor for me. He has been a mentor whose curiosity and enthusiasm have sustained me when results were not coming and have given me the confidence to step into unknown territories. Thank you Dan!

At the Beth Israel Deaconess Medical Center I met fantastic researchers and good friends. First of all, Aaron Grant, who has been my co-supervisor and with whom I have shared many passions in these years. Having him next door to check the physics of my work was reassuring and I was always sure I could move on after his OK on a theoretical derivation. However, that is nothing compared to the comforting feeling of knowing he always had a cartridge for the Lavazza espresso machine! Michael Ohliger, who preceded me as a graduate student working on inherent limitations on the performance of RF coils, was fundamental in getting me started with the research work that became my thesis project. He and Ernie Yeh were also good friends, who shared with me their experience as HST graduate students and were helpful big brothers at my first ISMRM conference in Miami Beach. Charlie McKenzie, whom unfortunately now I meet only at conferences, has been a friend and was also a teacher during my

first months in the lab. Speaking of people who have moved to different places, I am thankful to Steve Suddarth, Connie Cheng, Shmuel Cohen and Thoralf Niendorf for all their help. This thesis would have been different if Neil Rofsky, Bob Lenkinski and Dave Alsop had not allowed me to continue working in my office after Dan had moved to New York. I must also thank them for their continuous support and friendship over the past years. It has been a privilege getting to know and spending enjoyable evenings with Elena, Alex, Philip, Fotini, Ananth, Niki, Joao and Melissa. It is hard to condense into few words how grateful I am to all the people I have met at the Beth Israel Deaconess Medical Center, so I will just say a heartfelt thank you to Lois, Linda, Ivan, Anand, Susan, Rob, Barbara, Donna, Claire, Xiaoen, Jesse, Yael, Aya, Weiying, Reza, etc...

The members of my thesis Committee deserve a lot of my gratitude. Although they work in different institutions and live in different states, they have always been present for me and their advice has contributed to my success in the young investigator award competition. I also must thank Florian Wiesinger and Randy Giaquinto from General Electric, as well as a number of other people from the Martinos Center and from NYU Medical Center.

A special thanks goes to all HST friends and professors, with whom I share many memories: Martha Gray, who has been a friend before being my academic advisor, Blanca and Nate, Valerie and the 2007 ICM stars, Francisca, Lisa, Megan and many others. Finally I would like to thank Leonardo and all the other great Italians and Italian-Americans I met during my three years as President of MITaly.

a Marta e Beatrice

Table of Contents

Chapter 1

Introduction

1.1 Background

From its first steps in the 1970s (1-4), Magnetic Resonance Imaging (MRI) has come a long way to become today a fundamental diagnostic tool, whose applications range from imaging anatomical structures at high resolution (5-7), to visualizing in real time brain function or metabolism (8,9), with the promise of tracking stem cells injected into the body (10,11). Recent scientific and technological developments, for example in the area of hyperpolarization techniques (12,13), have the potential to cause a quantum leap and open the field of MRI to new clinical horizons. One significant and continuing advance in the fundamental capabilities of MRI began about a decade ago with the advent of phased arrays (14) and parallel imaging techniques (15-17), which have allowed intrinsic speed limits of MRI to be overcome.

Standard sequential MRI

In a magnetic resonance experiment, the signal, which relates to the physical and biochemical properties of the sample, is detected in the form of a radiofrequency (RF) voltage induced in a detector coil in response to the application of alternating magnetic fields to the object of interest. In order to reconstruct an image, the signal is spatially encoded by imposing magnetic field gradients during the acquisition.

The downside of such a method is that the gradients have to be re-applied many times to encode the entire field of view (FOV) and thus the acquisition time becomes longer as the resolution increases. Long acquisitions, besides being unpleasant for the patient and increasing the cost of the examination, can promote motion artifacts, which may limit the diagnostic value of some examinations. In recent years scientific advances in imaging hardware, as well as the development of fast imaging sequences (2,18-20), have contributed to substantial increases in the speed of MRI scans. However, the nature of the MR signal, together with physical and safety issues regarding the rate of application of radio frequency pulses and the switching rate of the magnetic field gradients used in the acquisition, imposes complex constraints on the maximum achievable speed.

Parallel MRI

The problem of lengthy acquisitions is intrinsic to standard Fourier encoding. The gradient fields manipulate directly the nuclear magnetization to be imaged and each encoding step produces a snapshot of a particular state of the magnetization. Clearly, only one state at a time can be portrayed, resulting in long scan durations for high-resolution images. Since it is not possible to acquire multiple gradient-encoded echoes simultaneously, methods which aim to accelerate data acquisition either must accelerate the process of gradient encoding (e.g. via improvements in gradient switching speed) or must acquire fewer gradient-encoded echoes and make up somehow for the missing information with supplementary encoding by other means. This latter approach is what is accomplished in parallel imaging. The first effort in this direction dates back to the late 1980 s, with the proposal of a hybrid method using dual receiving coils to reduce by ½ the number of phase-encoded echoes (21). There were other early proposals for parallel data acquisition with a higher number of receive coils (22-25), but, for reasons relating perhaps to the technological and intellectual readiness of the field, it was only in the late 1990 s that parallel magnetic resonance imaging was successfully applied to clinical scanning protocols (15,16). Parallel MRI is a revolutionary technique that uses arrays of RF coils to increase imaging speed, without increasing gradient switching rate or RF power deposition.

Coil arrays are commonly used in MRI because they provide images with a high signal-to-noise ratio (SNR) across a large FOV (14). The sensitivity of a detector coil to signal is high in the region directly below it and falls off with increasing distance from the coil center. Thus, in the case of a coil array, each detector captures a strong signal from a local region and the contribution, to both signal and noise, from the rest of the sample is negligible. This argument clearly shows the SNR advantage in using an array of coils to cover an extended region, rather than a large single coil with the same total area. Optimal SNR can be achieved using standard sequential MRI, by treating the complex-valued coil sensitivities as modulations of the magnetization, and by combining single-coil images into a composite reconstructed image via an appropriate matched filter (14).

Parallel MRI methods similarly take advantage of the local nature of the reception pattern of each array element, but exploit it to extract spatial information about the detected magnetization. Complementing such additional data with the spatial information obtained from the externally applied magnetic field gradients, images can be reconstructed from undersampled datasets. In this case, the complex-valued coil sensitivities are treated as a modulation of the gradient-derived encoding functions (26) and the omission of phase-encoding gradient steps enables scanning of the same FOV in less time.

It was in 1997 that parallel MRI was successfully applied *in vivo* with the simultaneous acquisition of spatial harmonics (SMASH) technique (15). SMASH emulates the effect of the omitted phase encoding gradients, shaping linear combinations of coil sensitivity functions into spatial harmonics. The method was made more robust and generally applicable in successive improved implementations (27,28). In 1999, the sensitivity encoding (SENSE) technique for parallel MRI was introduced and also employed to acquire accelerated *in vivo* images (16). SENSE is based on a different approach, which was first proposed in the early nineties (25), that involves using measured information about coil sensitivities to reconstruct an image from a set of aliased images, acquired with a reduced FOV.

Numerous other approaches have been proposed since the introduction of SMASH and SENSE (17,26,29-33) and parallel MRI is now a well-established technique in many areas of clinical medicine. Among those applications that strongly benefit from accelerated image acquisition are dynamic contrast enhanced angiography (34-37), real-time cardiac imaging (38), and abdominal imaging (39,40).

Despite the many advantages of parallel imaging, there are some disadvantages, including both practical issues (such as hardware compatibility and increasing system complexity) and intrinsic tradeoffs associated with fast scanning. For example, the penalty for using fewer *k-space* samples in the reconstruction is a reduced time averaging of noise, which leads to a loss in the SNR of the reconstructed image. Furthermore, parallel MRI reconstructions require non-orthogonal transformations, which lead to spatially dependent noise amplifications, commonly characterized in terms of the geometry factor (g) (16).

Despite these practical issues, substantial scan accelerations have been achieved in robust implementations, and efforts towards an ever greater number of receive channels have continued, raising the prospect of a complete replacement of gradient phase encoding by spatial encoding using many-element arrays. Unfortunately, in addition to practical considerations related to the complexity of many-channel MR systems, there are theoretical limitations. Inherent limits of parallel MRI performance were the subject of two articles, in which the ultimate intrinsic SNR was calculated for objects with uniform electrical properties, and its dependence on acceleration rate, main field strength and position in the sample was analyzed (41,42). Both investigations demonstrated that the largest achievable undersampling in parallel MRI is intrinsically limited by electrodynamics, as the ultimate SNR performance decays exponentially after a threshold reduction factor, which varies slightly depending on the main field strength, the electrical properties and the size of the sample. The good news is that this threshold is higher if the same degree of acceleration is achieved by undersampling in two dimensions, rather than one. In the past several years examples of 24-fold acceleration with a 32-element array have been reported for volumetric imaging and multidimensional spatial encoding (43). Highly parallel MRI is possible with

volumetric imaging thanks to the presence of multiple phase-encoded direction suitable for acceleration, as well as to the gain in baseline SNR provided by the increased quantity of acquired data, which compensates in part for SNR losses associated with undersampling. The possibility of large volumetric acquisitions with reasonable imaging time is very appealing, as it would lead to a major simplification of scanning procedures, eliminating for example the complex planning of oblique slabs in cardiac imaging. With the advent of ultra-high-field (UHF, 7T and above) MR systems, further increases in baseline SNR and acceleration capability may be envisioned, once the challenges associated with ultra-high field strength are addressed.

High field MRI

The first UHF-MRI system was developed about eight years ago (44) and today the number of systems at or above 7T is estimated around 30. Although MR systems operating at 1.5 T remain the first choice for routine clinical imaging, the push toward higher fields continues, driven by the promise of higher spectral and spatial resolution and higher SNR, which is in some approximate limits proportional to magnetic field strength (45). The first whole body 4 T MR magnet was installed in the early 1990 s and, although the quality of the first images was poor due to inhomogeneities and low contrast (46-49), technological improvements in coil design (50) soon highlighted the potential advantages of high field MRI. More convincing still were implementations of functional MRI (fMRI) at 4 T using the Blood Oxygen Level-Dependent (BOLD) effect (51). In 1999 the first images at 8 T were reported (52) showing a spectacular spatial resolution. However, soon after that, 7 T MR systems, which allowed for larger bore sizes (900 mm instead of 800 mm) and less expensive installations, became the UHF choice for all major MR vendors. There are only a few research groups focusing on 9.4 T (53) or even 11.74 T (54) systems, and 7 T is currently the most promising candidate for bringing UHF-MRI into clinical practice.

As the budget for hospital equipment is shared among an increasing number of medical technologies, impressive practical applications of UHF-MRI will need to be demonstrated in order to justify the substantial costs of UHF systems. Parallel imaging will play a fundamental role in enabling such applications. UHF-MRI and parallel

imaging are in many ways synergistic. Parallel MRI allows for faster acquisitions, minimizing artifacts present at high magnetic field strengths and, in turn, UHF-MRI can improve parallel imaging performance due to increased baseline SNR and improved encoding capabilities of high-frequency coil sensitivity profiles. Theoretical studies have shown that ultimate intrinsic SNR and acceleration efficiency benefit greatly from use of RF fields at higher frequencies (41,42).

However, there are still significant challenges which must be addressed for *in-vivo* applications of UHF-MRI. Some of these challenges relate to inhomogeneities in the static magnetic field, and others are associated with the high-frequency behavior of RF fields. The operating wavelength of the RF fields decreases as field strength increase, becoming ever smaller as compared to the dimensions of the human body, and resulting in ever larger interactions between electromagnetic fields and dielectric tissues. These interactions lead to local focusing of the RF magnetic field B_1, both in excitation and in reception, resulting in spatially-dependent signal variations or dropouts, which compromise the underlying SNR. On the other hand, the focusing of the RF electric field in dielectric tissues may lead to the formation of dangerous local amplifications of the specific absorption rate (SAR) which measures RF energy deposition in tissue. In addition to that, the magnitude of these electric fields per unit flip angle of RF excitation grows with frequency, causing an overall increase in the dissipated heat in the body. In recent years, multiple coil excitations with transmit or transceiver arrays have been quite successful in addressing these issues.

Parallel Transmission

Traditionally, there have been two main approaches to multicoil excitations. In RF shimming (50,55-57), all coils share the same gradient waveform and there is usually a single driving current that is modulated in amplitude and phase at each transmit element. More recently, MR systems with multiple transmit channels have enabled time-varying control of the electromagnetic field, leading to the development of parallel transmit techniques (58,59). In parallel excitation, also known as parallel transmission or transmit SENSE, there is a common gradient waveform and each individual coil is driven with a distinct tailored current waveform. Similarly to parallel

MRI, these techniques can exploit the additional degrees of freedom, provided by the number of transmit elements, to accelerate complex excitation pulses. However, much recent interest in parallel transmission has been addressed at its potential for compensating B_1 inhomogeneities and managing SAR.

It has become clear nowadays that the synergies between parallelism and UHF-MRI may naturally include transmission as well as reception. For this reason, MR vendors have started delivering new prototype systems that combine high magnetic field strength with multiple transmit and multiple receive capabilities. In this scenario, coil arrays will play the important role of enabling technology, as the efficacy of parallel MR techniques depends strongly on the amount and quality of the information provided by a coil array.

The role of coil arrays

Highly parallel MRI for rapid volumetric acquisition will be possible only with a large number of receiver coils encircling the body. Design of such many-element arrays poses various challenges. To accommodate large numbers of coils in a fixed space, individual coil sizes will necessarily be small, and coil-derived noise (e.g. Johnson noise from coil conductors and other circuit elements) may become comparable to noise derived from the body. Furthermore, traditional coil decoupling strategies which rely upon geometric overlap may lose effectiveness as the number of non-adjacent neighbor elements increases. Preamplifier-based decoupling, in which preamplifiers with low input impedance are used to minimize circulation of induced currents in the coils, may continue to play an important role, but the use of large numbers of preamplifiers will be associated with other challenges of mechanical and electrical design. Indeed, the sheer number of electronic components and cables in many-element arrays represent a practical burden after a certain point.

Nevertheless, simulations have shown that with a sufficient number of coils it is possible to approach the theoretical SNR limit (60), driving efforts toward the design of ever larger arrays. For example, preliminary results with a 96-element head array and a 128-element cardiac array have recently been presented (61,62).

The development of independently addressable transmit arrays represents an even greater technological investment than is required for receive arrays. On the other hand, the benefits of transmit arrays for UHF systems are quite clear. Common excitation with a single large volume transmitter is not generally used for UHF MRI, due to prohibitive power requirements and also to the inability of such a coil to produce a uniform excitation over an extended region. Local transmit coils are the norm for UHF applications, and it is natural in this context to consider transmission with multiple elements in parallel. In parallel transmission each transmit element is separately controlled to achieve tailored excitations that improve homogeneity and minimize RF energy deposition. As in the receive case, optimal coil combination coefficients are calculated inverting a sensitivity matrix, and the numerical conditioning of this inversion is affected by the geometry of the array. In particular, SAR is expected to vary substantially depending on the dimensions, shape and arrangement of the transmit coils (63). An indicator of the performance of transmit arrays, similar to the *g* factor of parallel imaging, has recently been proposed for accelerated parallel excitations (64).

From what has been discussed so far, it is evident that RF coils will continue to play a fundamental role in the future of MRI.

1.2 Problem statement

The quality of a coil array design is commonly judged on how it compares with other coil configurations. However, as the number of available receiver channels on modern MR systems increases, the cost and difficulties associated with building many-element array prototypes will make such empirical evaluations unrealistic. In this thesis we propose a method to assess the absolute performance of any coil array with respect to the theoretical highest SNR. Knowledge of coil efficiency as a percentage of the optimum will help in deciding when a design is good enough to cease iteration, and when a given number of coils is sufficient for particular imaging applications.

The field of parallel transmission is on the rise and there are many unsolved problems and unanswered questions. For instance, how much freedom is there to compensate for B_1 inhomogeneities while simultaneously minimizing RF energy deposition? In order to legitimate the large investments required for multiple transmit channel technology, it will be important to investigate the intrinsic constraints of parallel transmission techniques. In this thesis we investigate the trade-off between transmit homogeneity and SAR reduction, with respect to main magnetic field strength, sample size and acceleration. We introduced the concept of ultimate intrinsic SAR, the theoretical smallest RF energy deposition for a given flip angle distribution. Our work provides physical insight on the potential benefits of multiple coil excitations for ultra-high field MRI.

As the number of available transmit and receive channels increases, the design of many-element RF coil arrays will rely ever more on computer simulations. Numerical simulation techniques are lengthy and limited by computational power. In this thesis we derive a rigorous electrodynamic formulation for expressing the electromagnetic field inside homogeneous samples. Our method allows rapid computation of ultimate intrinsic SNR and SAR. It can be extended to simulate the case of particular coil geometries, allowing a direct comparison of coil performance with the theoretical limit. Ideal current patterns, corresponding to optimal performance, can be calculated, and they will serve as an important guide for improving existing coil designs and for developing innovative coils for high field applications.

Thesis outline

This thesis consists of this introduction, three main chapters and a final conclusion. The next chapter (Chapter 2) is an extended version of an abstract presented in 2006 at the fourteenth annual meeting of the International Society of Magnetic Resonance in Medicine in Seattle. It describes the method of coil performance mapping for evaluation of detector arrays. First, an expression for the ultimate intrinsic SNR is derived using electrodynamic theory, and then the scaling factors necessary to compare

the optimum with experimental SNR data are discussed. The method is demonstrated with a 32-element head array, and performance maps are reported for two different samples and various acceleration factors.

Chapter 3 is adapted from a manuscript in press at "Magnetic Resonance in Medicine" and it reports the results of a theoretical study of the fundamental limitations of multiple coil excitations. A pulse design strategy that enables excitation of a desired flip angle distribution with minimum SAR is described for the case of both RF shimming and parallel transmission. The strategy is then implemented using a complete set of basis functions that simulate the behavior of an infinite array in order to find ultimate intrinsic SAR. The dependency of SAR and transmit homogeneity on various practical factors is then investigated.

Chapter 4 describes in detail the electrodynamic formulation used to calculate optimal SAR and SNR. The derivation of electromagnetic fields from surface current distributions using dyadic Green's functions is shown for the case of spherical and cylindrical geometries. An expression for optimal SNR and SAR is derived in the ultimate case, as well in the case of finite coil arrays, with particular shapes and geometrical arrangements. Ideal current patterns are compared with optimized current distributions in finite coils, for different values of the main magnetic field strength.

The last chapter summarizes the main points of the thesis and discusses possible future work.

Chapter 2

A practical Method to Evaluate Coil Performance with Respect to the Ultimate Intrinsic SNR

Abstract

The quality of an RF detector coil design is commonly judged on how it compares with other coil configurations. The aim of this article is to develop a tool for evaluating the absolute performance of RF coil arrays. An algorithm to calculate the ultimate intrinsic signal-to-noise ratio (SNR) was implemented for a spherical geometry. The same imaging tasks modeled in the calculations were reproduced in reality using a 32-element head array. Coil performance maps were then generated based on the ratio of experimentally measured SNR to the ultimate intrinsic SNR, for different acceleration factors associated with different degrees of parallel imaging (for which similar assessments of absolute coil performance have not been reported previously). The relative performance in all cases was highest near the center of the samples (where the absolute SNR was lowest). The highest values were found in the unaccelerated case and a maximum of 94% was observed with a phantom whose electrical properties are consistent with values in the human brain. The performance remained almost constant for 2-fold acceleration, but deteriorated at higher acceleration factors. The method proposed here can serve as a tool for the evaluation of coil designs, as well as a tool to develop original designs which may begin to approach the optimal performance.

Introduction

Parallel MRI methods exploit the local nature of the reception pattern of the individual elements of coil arrays to extract spatial information about the detected magnetization (15-17). When this coil sensitivity information is combined with the spatial information obtained from externally applied magnetic field gradients, images can be reconstructed from undersampled datasets acquired in less time that would otherwise have been required with gradient encoding alone. Despite the many advantages of parallel imaging, one disadvantage is that parallel MR image reconstructions require the inversion of a non-unitary encoding matrix, which leads to spatially dependent amplifications of noise. This additional source of signal-to-noise ratio (SNR) loss has been used to assess the performance of coil arrays in parallel MRI applications and has been referred to as the geometry factor (g), since it depends on the shape of the coil sensitivity functions (16).

The dependency of g factor upon coil array geometry suggests that the SNR of the reconstructed image can be improved by optimizing the design of the receiver coil array. Nowadays it has in fact become common practice to include simulations of g in the design process (65,66). Although effective in improving existing array configurations, such a method does not necessarily aid in developing innovative designs and, furthermore, it gives no indication of how well a given design performs in comparison to the maximum achievable SNR.

Prior work has shown that there is in fact an inherent electrodynamic limit to the achievable SNR for any physically realizable receiver coil, and have modeled the behavior of ultimate intrinsic SNR (assuming sample-dominated noise) either in the absence (67) or in the presence (41,42) of parallel acceleration. The existence of an upper bound, independent of coil array design, on the performance of parallel MRI, may be very useful for coil optimization. The comparison of the ultimate SNR with the SNR of a coil array under development can indicate whether there is room for further improvement and can help to choose the best design for given field strengths and sample properties. Ocali *et al.* introduced a method to express the SNR

performance of a coil as a percentage of the best possible performance, in the case of standard gradient-encoded MRI (67). In the present work, following preliminary results presented at the 2006 meeting of the ISMRM in Seattle, Washington (68), we extend this method to include the effects of parallel imaging. Previous studies (41,42) of ultimate intrinsic SNR for parallel MRI have investigated the dependence of relative SNR on acceleration, without any absolute comparison to an actual coil array. Here we extend these previous studies to include just such absolute comparisons.

In order to achieve absolute comparisons, it was necessary to scale computed ultimate intrinsic SNR values by all known experimental factors influencing baseline SNR. We computed the ultimate intrinsic SNR, so scaled, at different points within an arbitrary section of two modeled phantoms, for a variety of acceleration factors. We then scanned the actual phantoms and measured the SNR at the corresponding pixel locations and for the same acceleration factors. In each case, the experimentally measured SNR values at each pixel were divided by the ultimate achievable values and displayed as two-dimensional maps. Coil performance maps were used to evaluate the effectiveness of a close-fitting 32-element head array design.

Methods

Review of the theoretical basis for an ultimate intrinsic SNR

The source of noise that inherently limits the SNR performance of MRI systems is electromagnetic fluctuations caused by thermal agitation of particles in the sample, as the contribution of other noise sources can in principle be diminished through technological improvements. For this reason, our derivation of the best possible SNR starts from the concept of intrinsic SNR, which is defined as the ratio of the NMR signal to the RMS noise voltage produced by the randomly fluctuating noise currents in the sample (41,42,67,69). The complex-valued signal voltage induced in a receiving coil by a nuclear magnetic moment $\boldsymbol{M}$ precessing at position $\mathbf{r}_0$ with the Larmor frequency ω about the z-axis, immediately after a 90° pulse, can be expressed, using

the principle of reciprocity (70), in terms of the RF magnetic field that would be transmitted at the same position by a unit current of frequency ω flowing around the coil:

$$v_S = \omega \boldsymbol{M} \cdot \tilde{\boldsymbol{\mathcal{B}}}_1^-(\boldsymbol{r}_0)^* = \omega M_O \left(\mathcal{B}_{1,x}(\boldsymbol{r}_0) - i\mathcal{B}_{1,y}(\boldsymbol{r}_0) \right), \tag{2.1}$$

where M_O is the equilibrium magnetization per unit volume and the net coil sensitivity is defined as the complex conjugate of $\tilde{\boldsymbol{\mathcal{B}}}_1^-(\mathbf{r}_0)$, the left-hand circularly polarized component of the RF magnetic field. The RMS noise voltage per root unit receiver bandwidth is given by:

$$v_N = \sqrt{8k_B T P_L} = \sqrt{4k_B T \int_{sample} \sigma(\mathbf{r}) \left| \mathcal{E}(\mathbf{r}) \right|^2 d^3\mathbf{r}}, \tag{2.2}$$

where k_B is the Boltzmann's constant, T is the absolute temperature of the sample and P_L is the power loss within the load (or sample). Resorting once again to the principle of reciprocity, P_L can be calculated with a volume integral as the Ohmic loss due to the RF electric field $\mathcal{E}$, which would be generated within a sample with conductivity σ by the coil if it were driven by a unit current (71).

An expression of the intrinsic SNR received by the coil, per unit sample volume and root unit receiver bandwidth, can be found by combining Eq. (2.1) and (2.2):

$$\mathrm{SNR}(\mathbf{r}_0)_{intr} = \frac{\omega M_O \left(\mathcal{B}_{1,x}(\mathbf{r}_0) - i\mathcal{B}_{1,y}(\mathbf{r}_0) \right)}{\sqrt{4k_B T \int_{sample} \sigma(\mathbf{r}) \left| \mathcal{E}(\mathbf{r}) \right|^2 d^3\mathbf{r}}} \tag{2.3}$$

The ultimate value of intrinsic SNR at any particular position **r** is found by maximizing the ratio in Eq. (2.3). The net coil sensitivity is directly related to the electromagnetic (EM) fields responsible for both signal reception and Ohmic losses in the sample; therefore signal and noise are linked by Maxwell's equations and cannot be treated separately in the search for the optimum SNR. The EM field can be expanded in an infinite basis set:

$$\mathcal{B}_1(\mathbf{r}_0) = \sum_{\gamma=1}^{+\infty} \alpha_\gamma(\mathbf{r}_0)\mathcal{B}_{1\gamma}(\mathbf{r}_0)$$
$$\mathcal{E}(\mathbf{r}_0) = \sum_{\gamma=1}^{+\infty} \alpha_\gamma(\mathbf{r}_0)\mathcal{E}_\gamma(\mathbf{r}_0) \qquad (2.4)$$

and each EM mode can be associated to a hypothetical coil, so that it is possible to specify a complete basis of coil sensitivities and the total noise power associated with any linear combination of them. The best possible SNR would then be given by the weighting coefficients $\alpha_\gamma(\mathbf{r}_0)$ that result in the highest intrinsic SNR (41,42,67). In the present work we use the weak Cartesian SENSE algorithm (16), which is an SNR-optimal reconstruction algorithm for parallel imaging that yields unit net coil sensitivity at the reconstructed voxel position $\mathbf{r}_o$ and zero at all aliasing positions $\mathbf{r}_n$. For this particular case, the search for maximum SNR is therefore equivalent to finding the reconstruction weights that minimize the total noise power in the denominator of Eq. (2.3), subject to the following constraint:

$$\mathcal{B}_{1,x}(\mathbf{r}_n) - i\mathcal{B}_{1,y}(\mathbf{r}_n) = \delta_{n0} \qquad \text{for n = 0...R-1,} \qquad (2.5)$$

where δ is the Kronecker delta and R is the reduction, or acceleration, factor. The solution was given by Pruessmann et al. (16) and an expression for the ultimate intrinsic SNR per unit volume and unit bandwidth at any pixel position $\mathbf{r}_o$ was derived in Ref. (42):

$$\mathrm{SNR}(\mathbf{r}_0)_{\text{ult intr}} = \frac{\omega M_0}{\sqrt{4k_B T\left[\mathbf{S}^\dagger \boldsymbol{\Psi}^{-1}\mathbf{S}\right]^{-1}_{0,0}}} \qquad (2.6)$$

In this expression, where any scaling factor related to the particular pulse sequence has been removed, the superscript ^{H} indicates conjugate (Hermitian) transpose and **S** denotes the [L × R] encoding matrix (16), containing the sensitivities of all chosen L basis elements (or a subset of the full basis that is sufficient for the convergence of the calculation) at the reconstructed voxel position $\mathbf{r}_0$ and all aliased positions in case of undersampling:

$$\mathbf{S}_{\gamma n} = \mathcal{B}_{1\gamma,x}(\mathbf{r}_n) - i\mathcal{B}_{1\gamma,y}(\mathbf{r}_n) \tag{2.7}$$

$\boldsymbol{\Psi}$ is the [L × L] noise covariance matrix, which characterizes the noise received by each coil and the correlated noise between coils (72):

$$\boldsymbol{\Psi}_{\gamma,\gamma'} = \int_{sample} \sigma(\mathbf{r})\mathcal{E}_{\gamma}(\mathbf{r}) \cdot \mathcal{E}_{\gamma'}(\mathbf{r})^* d^3\mathbf{r} \tag{2.8}$$

The "0,0 subscript in the denominator of Eq. (2.6) indicates the diagonal element of the matrix in square brackets with an index associated with the target position $\mathbf{r}_0$.

Ultimate intrinsic SNR depends on the modeled object geometry and is independent of the particular choice of the basis functions. However, previous studies have shown that the numerical complexity involved in calculating SNR from Eq. (2.6) is affected by the choice of basis functions, and have selected basis functions tailored to the object geometry (41,42). In the present study, the EM modes inside a spherical object were derived by performing a full-wave EM field expansion into vector spherical harmonics.

Ultimate intrinsic SNR calculation

Ultimate intrinsic SNR was calculated inside a sphere with uniform electrical properties. The net EM field was derived by performing a mode expansion with dyadic Green's functions (DGF) (73), following a method recently described (74). We chose this approach over others relying on EM field-based sensitivity basis set (41,42), as the DGF formalism enables calculating the current patterns corresponding to the optimized SNR (74). Given any spatial current distribution **J**, the electric field can be calculated as:

$$\mathcal{E}(\mathbf{r}) = i\omega\mu_o \int_{sample} \mathbf{G}(\mathbf{r},\mathbf{r}') \cdot \mathbf{J}(\mathbf{r}) d^3\mathbf{r}', \tag{2.9}$$

where μ_o is the magnetic permeability in free-space and $\mathbf{G}(\mathbf{r},\mathbf{r}')$ is the branch of the DGF associated with the region indicated by **r**. We started by defining a complete basis set of surface current modes, distributed on a spherical surface at 5 mm distance from the surface of the modeled sphere. The generic surface current mode was expressed as:

$$\mathbf{K}_{lm} = W_{lm}^{(M)}\mathbf{X}_{l,m}(\theta,\varphi) + W_{lm}^{(E)}\hat{\rho}\times\mathbf{X}_{l,m}(\theta,\varphi), \tag{2.10}$$

where l, m are the expansion indices, $\mathbf{X}_{l,m}$ is a vector spherical harmonic and $W_{lm}^{(M)}$ and $W_{lm}^{(E)}$ are the series expansion coefficients representing divergence-free and curl-free surface current contributions, respectively. Dyadic Green's functions associated with a dielectric sphere were defined as double series of vector wave functions in spherical coordinates (74):

$$\begin{aligned}\mathbf{M}_{l,m}(\mathbf{r},k) &= j_l(k\rho)\mathbf{X}_{l,m}(\theta,\varphi)\\ \mathbf{N}_{l,m}(\mathbf{r},k) &= (1/k)\nabla\times j_l(k\rho)\mathbf{X}_{l,m}(\theta,\varphi)\end{aligned}, \tag{2.11}$$

where k is the complex wave number, ρ is the radial coordinate and j_l is a spherical Bessel function of order l. Once the electric field is computed, the magnetic field can be derived as $\mathcal{B}(\mathbf{r}) = (-1/i\omega)\nabla\times\mathcal{E}(\mathbf{r})$.

We assumed that the hypothetical coils derived from the basis set were made of perfect conductors, to guarantee that only sample noise contributed to the ultimate intrinsic SNR. In this way, the denominator of Eq. (2.6) does not require any additional term and the encoding matrix and the noise covariance matrix in Eq. (2.7) and (2.8) can be constructed using Eq. [B8] and [B7] of Ref. (42), respectively. Eq. [B7] was multiplied by the conductivity of the sample, to correct for a minor typographical error.

The modeled sphere was chosen to match the geometry and the electrical properties of two existing spherical MR phantoms, henceforward referred to as "Phantom 1 and "Phantom 2 . Phantom 1 is a "Braino" phantom (GE Medical Systems, Milwaukee, WI, USA) and Phantom 2 is a low-conductivity phantom (Siemens Healthcare, Erlangen, Germany). Both phantoms have diameter equal to 16.86 cm (Figure 2-1).

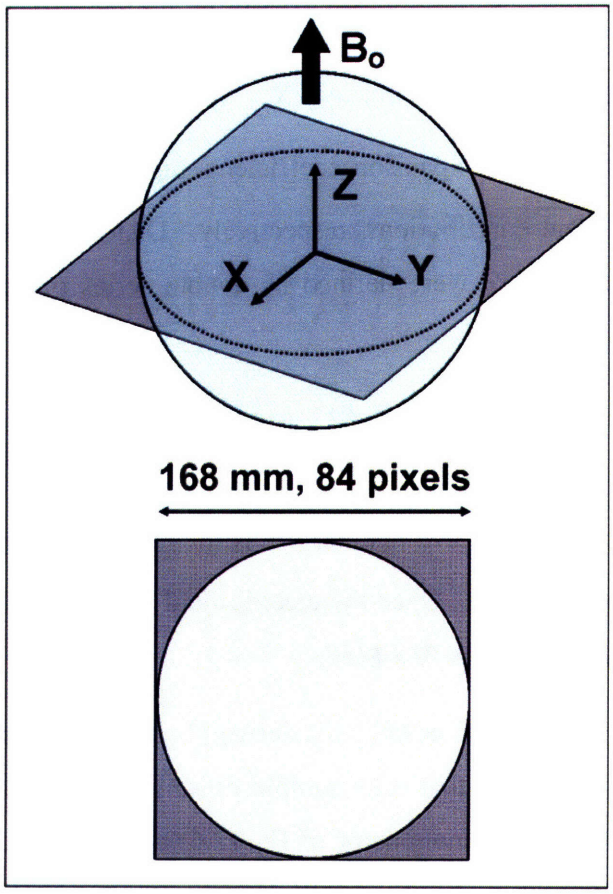

Figure 2-1. Schematic diagram of the image plane and the FOV used to calculate ultimate intrinsic SNR for the spherical phantom. The FOV is a square with a side of 16.8 cm, just large enough to contain the entire circular section. It is uniformly divided into an 84 x 84 grid of pixels.

Water solutions equivalent to the content of each phantom were mixed and their conductivity and permittivity at 123.22 MHz (the operating frequency of the MR scanner used in our experiments) were measured using an Agilent 85070E dielectric probe (Agilent Technologies, Palo Alto, CA, USA). Conductivity and relative permittivity were 0.97 $Ohm^{-1}m^{-1}$ and 81.3 for Phantom 1, whereas for Phantom 2 they were 0.084 $Ohm^{-1}m^{-1}$ and 80. Magnetic permeability of free space was used in both cases. A transverse section through the center of the sphere was divided into an 84 by 84 grid of square pixels with 2 mm side (Figure 2-1) and ultimate intrinsic SNR was calculated at each position, assuming 2.89 T static magnetic field strength and room

temperature of 298 degrees Kelvin. Calculations were implemented in Matlab (MathWorks, Natick, MA, USA).

Experimental data acquisition

The spherical phantoms were scanned on a Siemens TIM Trio 3T scanner (Siemens Healthcare, Erlangen, Germany) using the same image planes modeled in the ultimate intrinsic SNR simulations (see Figure 2-1). The RF receive coil used in the SNR measurements was a receive-only head coil array (Figure 2-2) consisting of 32 overlapping circular surface coil elements arranged over the entire dome of the head (75), with the scanner body coil used for transmit. The coil was tuned and matched for a human head.

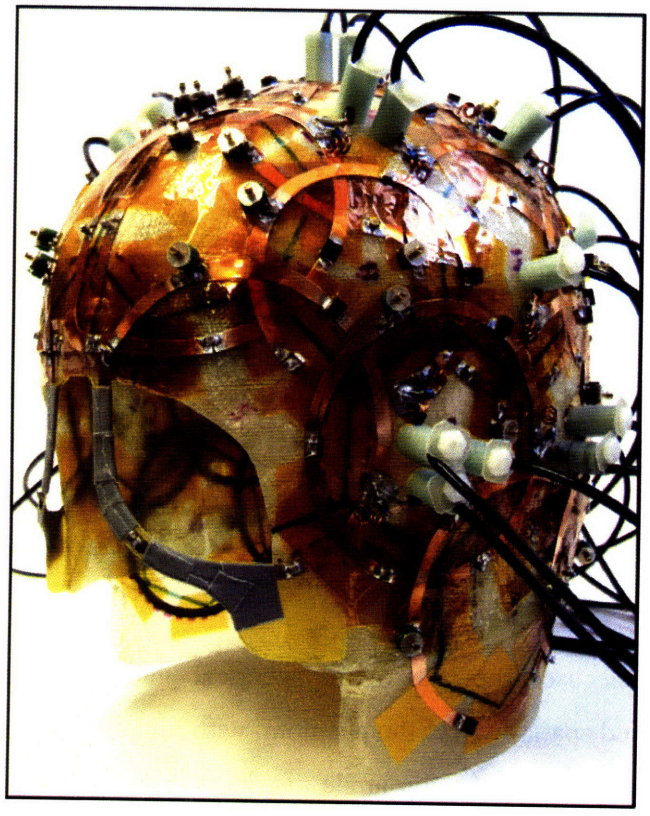

Figure 2-2. 32-element receiver coil array employed in the experimental study. The surface coils are packed on a thin helmet-shaped plastic frame that minimizes the distance from the sample.

A single proton density weighted two-dimensional gradient echo image was obtained with parameters TR = 2000 ms, TE = 3.8 ms, flip angle = 20°, slice thickness = 3 mm, 128×128 matrix, FOV = 256 mm, pixel half-bandwidth = 25.6 kHz (line bandwidth = 200 Hz/pixel). A long TR was chosen to avoid any T1 dependence in the image. To map the flip angle distribution over the phantom, eight additional images were acquired with identical pulse sequence parameter values but with increasing transmit voltages to achieve several nominal flip angles ranging from 60° to 150° in 15° increments and receiving with the body coil, including a body coil noise reference acquired at 0° flip angle.

For each acquisition, raw *k*-space data were saved for offline analysis, and magnitude images reconstructed online were also saved for comparison. Each image acquisition was accompanied by a noise reference measurement obtained by recording complex-valued data with the array coil during the same pulse sequence used for the image acquisition but with no RF excitation; this ensured that the noise samples were bandwidth-matched with the image acquisition and that a sufficient number of noise samples were acquired to accurately estimate the noise.

Experimental SNR calculation

All image reconstruction and analysis was performed offline with custom software written in MATLAB (The Mathworks, Natick, MA). Image data were acquired with a Cartesian *k*-space sampling and two-dimensional Fourier imaging, thus a standard image reconstruction consisting of standard FFT operations for each individual coil channel was carried out. No apodization or filtering was applied at any stage of the image reconstruction.

Due to the dielectric properties of the spherical phantoms, the flip angle of the RF excitation varied spatially over the phantom, with higher flip angles at the center of the phantom (76,77). Since the flip angle distribution affects image SNR, these transmit effects were identified and removed from the empirical SNR calculation. To compute the flip angle distribution, we fit a sinusoidal model of image intensity as a function of transmit voltage across the eight body coil reference images to each image pixel with

the MATLAB function "*fminsearch*". The fit produced two parameters at each pixel from which the achieved flip angle map $\hat{\theta}(x,y)$ was calculated. The flip angle correction map was then generated as $\sin\left(\hat{\theta}(x,y)\right)/\sin(\theta_0)$, where θ_0 is the desired flip angle (which in this case was 20°, as specified above). This correction was applied to the individual coil images to normalize the effect of the intensity non-uniformity caused by the flip angle distribution, giving rise to a compensatory intensity increase in the periphery of the phantom.

Because the phantoms contained no internal structure, the resulting image from a given coil element after flip angle normalization provided a good approximation to the element's sensitivity profile. Although noise contributes some degree of error to this approximation, no smoothing or interpolation was applied to the images to avoid introducing bias into the sensitivity approximation and subsequent SNR calculation.

The noise covariance matrix $\mathbf{\Psi}$ was calculated from the statistics of the noise samples scaled by dividing the sample covariance matrix $\hat{\mathbf{\Psi}}$ by the noise equivalent bandwidth b_{noise} to account for noise correlations due to the filtering introduced by the data acquisition electronics and receiver, i.e. $\mathbf{\Psi} = \hat{\mathbf{\Psi}}/b_{noise}$ (78).

Images reconstructed for each coil channel from the fully sampled dataset were then combined with the optimal matched filter SNR combination method (14), which incorporates both the approximations of the coil sensitivity and the channel noise covariance matrices in the combination to boost the combined image SNR. Note that, because in the ultimate SNR simulations the signal is defined to be complex-valued, we adopt an observation model where the signal is assumed complex-valued and thus the image SNR calculated from the imaging data does not require an additional $\sqrt{2}$ scaling (see, e.g., Ref. (78,79)). In order to eliminate any phase variation in the experimental data, the absolute magnitude of the final complex-valued combined SNR image was taken. A final correction was applied to the resulting thermal SNR images for the SNR bias introduced by the magnitude detection (78-80), which is the

generalization of the well-known Rician distribution correction (81) to multiple-channel coil arrays.

The optimal Roemer combination method yields the same SNR of a fully-sampled (i.e. unaccelerated) SENSE reconstruction (16). The resulting 128×128 SNR image was cropped around the object boundaries, resulting in an 84×84 image with each pixel corresponding to a position in the grid of computed ultimate intrinsic SNR values. SNR and g images for acceleration factors 2, 4, and 6 were obtained from the fully sampled dataset, using the SENSE reconstruction algorithm (16) with one-dimensional undersampling on the x-y plane. To maximize coil performance in the accelerated cases, the images were first cropped to produce a tight FOV around the phantom, resulting in a cropped image size of 84×84. Estimates of the coil sensitivity profiles were generated by low-pass filtering the resulting image intensities with a two-dimensional Hanning filter (normalized for unity noise gain) with a cutoff set to include only the central 25% of k-space. Noise covariance matrices were estimated as described above, and the geometry factor was calculated directly from the analytic expression (16).

Coil performance maps

The ultimate intrinsic SNR is calculated considering the effects of a net EM field acting at particular positions inside a sample, without associating them to actual MR image pixels. The values computed are therefore relative measures of the optimal SNR and, without losing generality in the discussion, they can be used to theoretically investigate the behavior of the optimum for various acceleration factors and at different field strength.

On the other hand, in order to compare the experimental SNR data with the simulated data, the ultimate intrinsic SNR values must be properly scaled to account for the specific pulse sequence parameters and system characteristics:

$$\mathrm{SNR}'(\mathbf{r}_0)_{\text{ult intr}} = \mathrm{SNR}(\mathbf{r}_0)_{\text{ult intr}} \cdot \frac{V_{\text{voxel}}\sqrt{\mathrm{N_{acq}NEX}}\sin(\theta)}{\mathrm{F}\sqrt{\Delta f}} \qquad (2.12)$$

where V_{voxel} is the volume of the voxel, N_{acq} is the number of the acquired *k*-space samples, which accounts for the signal summation resulting from Fourier transform, NEX is the number of signal averages, θ is the nominal flip angle, F is the noise factor of the preamplifiers connected to the coils and Δf is the receiver bandwidth. The noise figure (*NF*), which is the noise factor expressed in dB, was measured experimentally using the "hot-cold resistor" method (82) and the noise factor was then derived from $NF = 10\log_{10} F$. Table 1 summarizes the numerical values of the scaling factors, as well as the values of the phantom's dielectric properties and of the other quantities used in the calculations. These quantities include the operating frequency ω and the equilibrium magnetization M_O at the field strength of interest, here 2.89 T. M_O appears in Eq. (2.6) for ultimate intrinsic SNR, and must be accounted for correctly. The final value of M_O listed in Table 1 was computed using the expression:

$$M_O = \frac{N\gamma^2\hbar^2 I(I+1)B_O}{3k_B T} \tag{2.13}$$

with the gyromagnetic ratio $\gamma = 2.68\times10^8$ rad T^{-1} s^{-1}, the temperature of the sample T = 298 K, the main magnetic field B_O = 2.89 T, I = 1/2 for hydrogen and the number of nuclear spins per unit volume $N = 6.691\times10^{28}$ m^{-3}. k_B is Boltzmann's constant and $\hbar$ is Planck's constant divided by 2π. It is also important to notice that, although final matrix size is 128×128, N_{acq} is equal to $(256\times128)/R_{accel}$, with R_{accel} being the acceleration factor, because there were 256 *k*-space samples for each readout, due to an automatic 2-fold oversampling performed by the MR system.

An accurate scaling of ultimate intrinsic SNR is critical to the absolute significance of coil performance maps, which are defined as the ratio of the experimental SNR images to the corresponding scaled ultimate intrinsic SNR images:

$$\mathrm{CPM}(\mathbf{r}_0) = \frac{\mathrm{SNR}(\mathbf{r}_0)_{\mathrm{array}}}{\mathrm{SNR}'(\mathbf{r}_0)_{\mathrm{ult\ intr}}} \tag{2.14}$$

Performance maps provide a measure of the efficiency of each coil array for the specific imaging task, as a function of position inside the sample of interest. Maps were generated for various acceleration factors.

Table 1
Dielectric properties, constants and scaling factors used in the calculations

Larmor frequency	$\omega/2\pi$	123.22	MHz
Equilibrium magnetization	M_0	9.03×10^{-3}	$A \cdot m^{-1}$
Boltzmann constant	k_B	1.381×10^{-23}	$J \cdot K^{-1}$
Sample temperature	T	298	K
Conductivity	σ	0.97 Phantom 1 0.08 Phantom 2	$\Omega^{-1} \cdot m^{-1}$
Relative permittivity	ε_r	81.3 Phantom 1 80 Phantom 2	-
Vacuum permittivity	ε_o	8.85×10^{-12}	$C^2 \cdot N^{-1} \cdot m^{-2}$
Permeability	μ	1.2566×10^{-6}	$Wb \cdot A^{-1} \cdot m^{-1}$
Volume of the voxel	V_{voxel}	1.2×10^{-8}	m^3
Receiver bandwidth	Δf	51.2	kHz
Flip angle	θ	0.3421	rad
Noise factor	F	1.22	-
Signal averages	NEX	1	-
Acquired data points	N_{acq}	$(256 \times 128)/R_{accel}$	-

Results

Coil performance maps for the 32-element head array are shown in Figure 2-3, for both phantoms and various degrees of acceleration. In all cases the performance, relative to the ultimate intrinsic SNR, was highest near the center of the object and approached zero near the surface, where the ultimate SNR assumes its largest values.

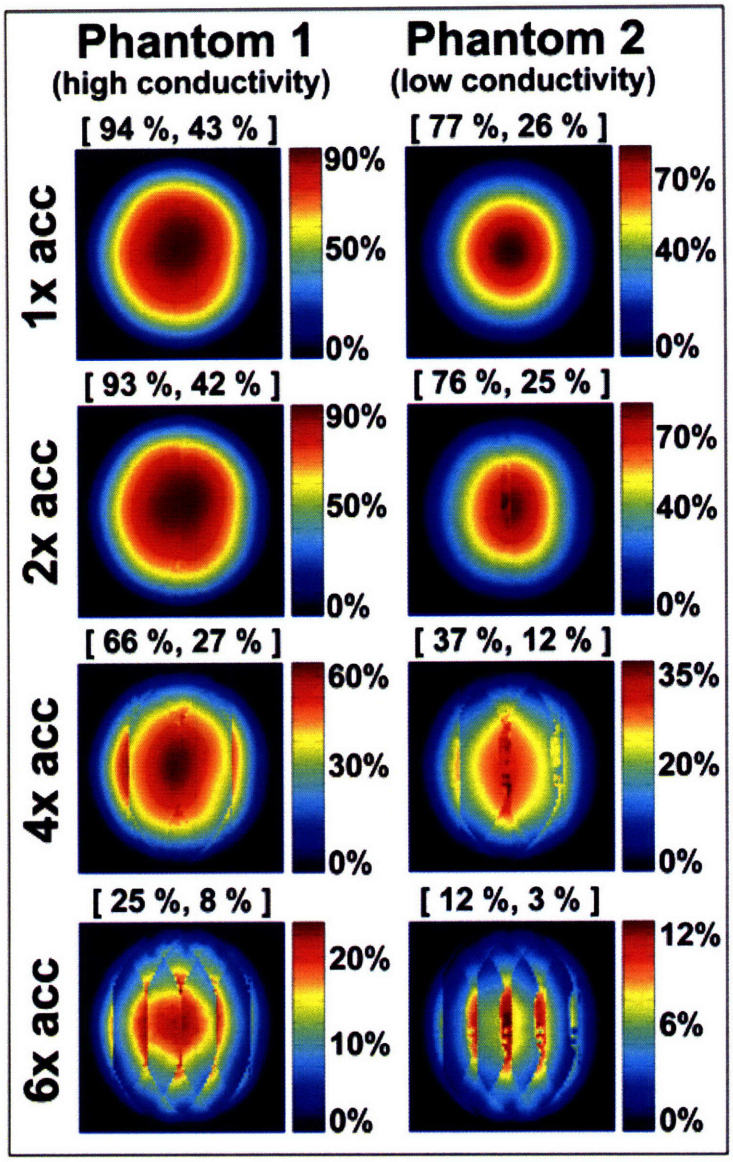

Figure 2-3. Coil performance maps for an axial slice at 2.89 T in the center of a uniform spherical phantom. The performance of the 32-element head array with respect to the ultimate SNR is shown for two different phantoms and various acceleration factors. Each pixel represents the experimental SNR divided by its corresponding ultimate SNR value. Above each map, the maximum and the mean performance are indicated in brackets and reported as a percentage of the optimum. The mean is computed including only the pixels inside the circular section of the object.

The peak performance was in the unaccelerated case and was 94% and 77% for Phantom 1 and Phantom 2, respectively. The maximum and mean performance (reported in square brackets above each map) both decreased as the acceleration factor was increased. For 2-fold acceleration the performance was almost equal to that in the fully-sampled reconstruction, whereas for 6-fold undersampling, noise amplifications substantially degraded image SNR and the maximum performance with Phantom 1 and 2 decreased to 25% and 12% of the ultimate SNR, respectively.

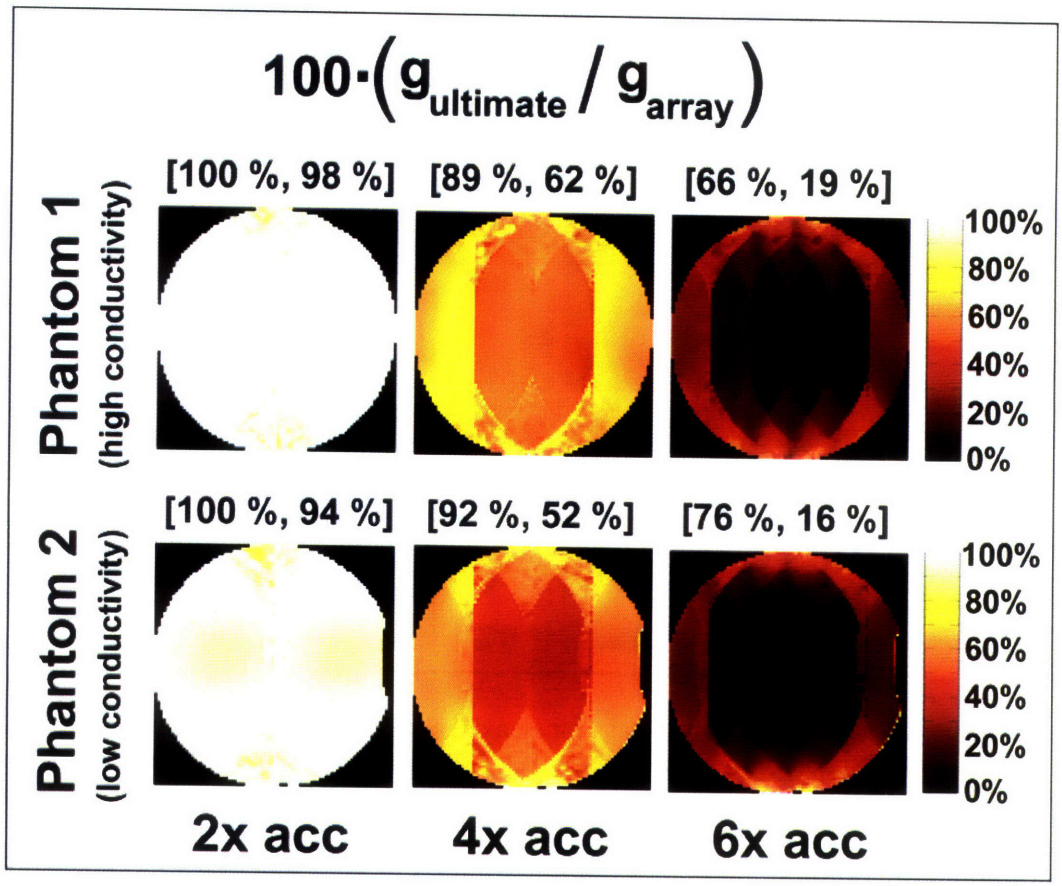

Figure 2-4. Geometry factor performance for different parallel imaging accelerations at 2.89 T for an axial slice in the center of a uniform spherical phantom. The geometry factor of a 32-element head array with respect to the corresponding value in the ultimate intrinsic case is shown for two different phantoms and various acceleration factors.

Figure 2-4 shows the performance of the coil in terms of the geometry factor. Although these maps do not provide an absolute measure of the coil performance, they are useful in investigating the potentiality of the coil for parallel imaging tasks and they can be more easily calculated without worrying about the scaling factors in Eq. (2.12). We notice that the 32-element array is almost equivalent to a hypothetical infinite array for 2-fold acceleration, whereas its efficiency in accelerating by a factor of 6 is less than 20% compared to the ultimate case.

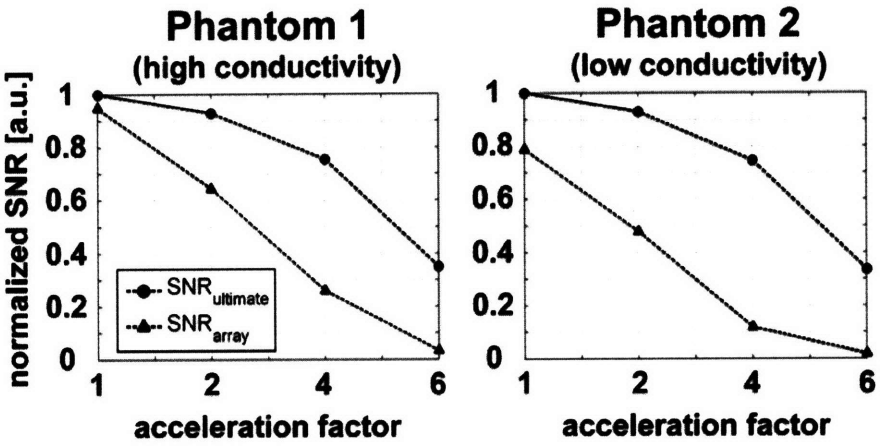

Figure 2-5. SNR as a function of acceleration factor for a voxel in the center of a spherical phantom. The SNR obtained with a 32-element head array is compared with the corresponding ultimate intrinsic SNR for two homogeneous phantoms, with equal dimensions and different electrical properties.

Comparisons with the ultimate intrinsic SNR and g in the center of the sample are shown as a function of acceleration factor in Figures 2-5 and 2-6, respectively. In Figure 2-5 we see that the performance of the coil is worse in the case of Phantom 2 and we also notice that, as we move to higher degrees of acceleration, the difference between the SNR of the coil and the ultimate intrinsic SNR increases more rapidly for Phantom 2. This is confirmed by the graphs in Figure 2-6, which show that for 2-fold acceleration ultimate intrinsic g and g of the array overlap for both phantoms, whereas for 6-fold acceleration g of the array becomes 12 for Phantom 1 and 18 for Phantom 2, though ultimate intrinsic g remains almost equal in both plots.

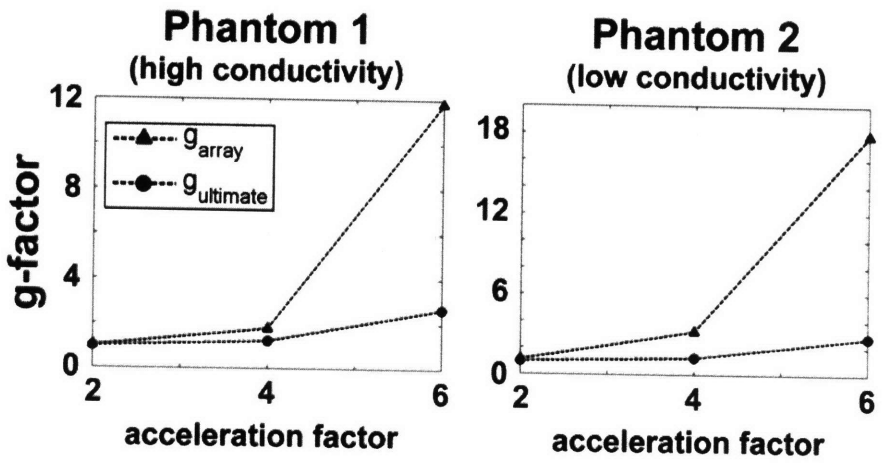

Figure 2-6. Geometry factor as a function of acceleration factor for a voxel in the center of a spherical phantom. The geometry factor of a 32-element head array is compared with the corresponding optimal values for two homogeneous phantoms, with equal dimensions and different electrical properties.

Discussion

As the number of available receiver channels on modern MR systems increases, greater attention will be paid to the design and performance of many-element RF coil arrays. Questions regarding the balance of coil-noise and sample-noise, or the suitability of any particular array design for parallel imaging, promise to take on new significance as the number of elements increases. In the present work a method has been described to evaluate the absolute performance of any particular coil array. Although originally conceived to improve the design of receiver coils for parallel MRI applications, the procedure can be applied to sequential imaging as well.

The performance of any coil array is strictly constrained by the behavior of electromagnetic fields within the sample (41,42,67). For a chosen imaging task, the best possible SNR achievable for any coil configuration can be computed using a complete set of coil sensitivity basis functions.

In this study, we used a recently proposed algorithm to compute ultimate SNR for spherical geometries (74). Ultimate intrinsic SNR values were calculated for each pixel position on specific image planes and used as a reference to assess the efficiency

of a 32-channel receiver head coil in imaging two homogeneous phantoms, having equal dimensions but different electrical properties. The results were presented in the form of performance maps, which display the percentage of the optimum SNR that is achieved at each pixel.

It should be noted that, although our experiments were performed only at 2.89 T, the basis functions used in this work take full account of the frequency-dependence associated with operation at different field strengths, and that coil performance maps are possible at arbitrary field strength. That said, simple phantom geometries with uniform electrical properties are expected to become an increasingly poor approximation of *in vivo* SNR behavior with increasing field strength. The characterization of coil performance for arbitrary electrically inhomogeneous objects remains possible with appropriate choices of surface-based field or current basis functions, but would also require extensive computational effort.

In simulating the ultimate SNR we are effectively using an infinite number of coils surrounding the object, and we expect a very high signal close to the surface. As a consequence, the ultimate SNR rises rapidly at the edges, and relative coil performance is higher near the center of the object. A similar spatial variation was reported in a previous paper, which showed coil performance maps in the case of non-parallel MRI (67). The performance values presented in that study are slightly lower than those found in this investigation for the unaccelerated case, but the results are not directly comparable as the phantom, the image section, and the imaging system were different. Small typographical differences in scaling of SNR, as noted in Ref. 7, may also have had an effect. Coil performance maps for parallel MRI were presented for the first time in 2006 (68) for the case of a cylindrical phantom. In that preliminary work, the authors reported performance values of less than 50% in the center of the sample. The low performance was in part due to the particular coil-phantom configuration. In fact, the surface arrays used in that study were originally tuned and matched for a rectangular phantom rather than a cylindrical phantom.

In the current work, the overall maximum performance, corresponding to the unaccelerated case with Phantom 1, was more than 90% in the central portion of the

phantom, implying that there is little room for improvement. A similar behavior in the center was predicted by a simulation study which modeled receive arrays of circular coils, optimally arranged around a sphere (60). In that work the electrical properties of the sphere were chosen to approximate values in the human brain and they were consistent with those measured for Phantom 1. The fact that coil performance was lower with Phantom 2 does not imply that the head array design is suboptimal for its target clinical applications, as Phantom 2 is filled with a solution whose electrical properties are not meant to approximate human tissue, but rather to minimize susceptibility artifacts. Furthermore, as the array was tuned and matched for the human head, better loading with Phantom 1 might have positively affected the performance results.

The average performance of the coil array (see Figures 2-3 and 2-4) was almost constant for 2-fold acceleration, but rapidly decreased for larger acceleration factors. This suggests that 32 elements are not enough for highly accelerated parallel imaging and that larger arrays are needed in order to approach the acceleration efficiency of the ultimate intrinsic case.

The examples shown in this work prove that the method proposed here can serve as a tool for the evaluation of coil designs. Ultimate intrinsic SNR defines an absolute performance target for coil designers, and coil performance maps provide useful and immediate feedback on how far a particular array configuration is from such expectations. Ultimate SNR needs to be computed only once for each particular geometry, and that will eventually facilitate its employment as an additional instrument for coil engineers.

Given the comparatively large set of basis functions required for convergence of the ultimate intrinsic SNR at multiple positions, it is unlikely that all the modes used to simulate the optimum can be practically realized with an actual coil array. However, if further investigation shows that a smaller subset of the larger basis can capture the dominant SNR behavior, then it may be possible to build an array targeted to that subset in order to approach the simulated optimal sensitivity patterns (see Ref. (60)). These ideal EM fields can be directly computed using the weighting factors generated

by the ultimate SNR optimization, but they would be different for every point in the sample. Thus, only a trade-off solution might exist for the conductor patterns which will be needed to produce fields as close as possible to the optimum for the largest number of positions. Genetic algorithms have been already applied to a similar optimization problem (83) and, with an accurate and robust parameterization, they might be employed also for the design of ideal coil arrays for different parallel MRI applications.

Since such arrays should in principle perform very close to the optimum, any discordance could be linked to noise other than that coming from the sample. The development in recent years of arrays with very many elements (61,84) has raised to practical priority the question of what is the smallest size for array elements before the final SNR begins to be dominated by the noise coming from the electronic components.

In conclusion, the capability of parallel MRI to accelerate image acquisitions is fundamentally limited by electrodynamic constraints, but the knowledge of such limitations can be exploited to improve current coil design and to eventually develop innovative receivers that may operate close to the optimum.

Acknowledgements

The authors thank Michael Ohliger for his help and advice in understanding the theory behind ultimate SNR. The authors are also grateful to Florian Wiesinger for helpful discussions about ultimate SNR in a spherical geometry. This work was supported in part by NIH grants R01-EB000447 and R01-EB002468.

Chapter 3

Electrodynamic Constraints on Homogeneity and RF Power Deposition in Multiple Coil Excitations[1]

Abstract

The promise of increased SNR and spatial/spectral resolution continues to drive MR technology toward higher magnetic field strengths. SAR management and B_1 inhomogeneity correction become critical issues at the high frequencies associated with high field MR. In recent years, multiple coil excitation techniques have been recognized as potentially powerful tools for controlling SAR while simultaneously compensating for B_1 inhomogeneities. This work explores electrodynamic constraints on transmit homogeneity and SAR, for both fully parallel transmission and its time-independent special case known as RF shimming. Ultimate intrinsic SAR – the lowest possible SAR consistent with electrodynamics for a particular excitation profile but independent of transmit coil design – is studied for different field strengths, object sizes and pulse acceleration factors. The approach to the ultimate intrinsic limit with increasing numbers of finite transmit coils is also studied, and the tradeoff between homogeneity and SAR is explored for various excitation strategies. In the case of fully parallel transmission, ultimate intrinsic SAR shows flattening or slight reduction with increasing field strength, in contradiction to the traditionally cited quadratic dependency, but consistent with established electrodynamic principles.

[1] The work in this chapter has been adapted for publication as "Lattanzi R, Sodickson DK, Grant AK and Zhu Y: *Electrodynamic Constraints on Homogeneity and RF Power Deposition in Multiple Coil Excitations*. Magn Reson Med. (in press)"

Introduction

The advantages of using high magnetic field strengths for MR imaging and spectroscopy are well known: they include the promise of improved signal-to-noise ratio (SNR) and spatial or spectral resolution, as well as the potential for improvements in certain useful forms of contrast. The challenges of high field strength are also well known, including a variety of difficulties associated with reduced homogeneity in both static and radiofrequency (RF) fields. For RF fields in particular, the operating wavelength decreases as field strength and Larmor frequency increase, becoming ever smaller as compared to the dimensions of the human body, and resulting in ever larger interactions between electromagnetic fields and dielectric tissues. These interactions lead to local focusing of the RF magnetic field B_1, both in excitation and in reception. The focusing of B_1 field results in interference patterns (77), which compromise the underlying SNR increases associated with high field strength and which would in many cases markedly impede clinical diagnosis. B_1 focusing also results in subject-specific spatial variations of flip angle, which can diminish the reliability of image contrast. Meanwhile, the focusing of RF electric fields in dielectric tissues at high frequency results in increasingly inhomogeneous and subject-dependent specific absorption rate (SAR). Furthermore, the magnitude of electric fields produced for a given strength of the transmit magnetic field (i.e. per unit flip angle of RF excitation) is generally expected to grow with frequency. These electric fields induce eddy currents and dissipate heat in the body, causing an overall SAR increase which has (in admittedly casual approximations based on low- to moderate-frequency behavior) been taken to increase approximately with the square of the frequency.

Compensation of B_1 inhomogeneities and management of SAR are indeed among the most difficult challenges faced by *in-vivo* ultra high field MR applications. RF-induced heating is a potentially elevated safety concern at high field strength, both requiring careful design and evaluation of RF coils and necessitating worst-case safety limits on flip angles in MR pulse sequences, which can further erode achievable high-field SNR and contrast. Various approaches to homogeneity correction and SAR

management have been proposed, involving either coil design or pulse sequence design.

At low magnetic field strength, birdcage coils are commonly used to produce homogeneous excitations over a large fields of view, but traditional birdcage designs can exhibit significant B_1 inhomogeneities and SAR increases when operating at high frequency (85). Various novel volume coil designs with improved homogeneity and efficiency at high field strength have been developed in recent years (57,86). Recent work using numerical methods has also shown that further variations in RF coil design can serve to redistribute RF energy absorption over the imaged object, in order to remove hot spots caused by RF field concentrations (87).

One noteworthy feature which has begun to distinguish high-field coil design is the use of multiple transmit elements or drive points. This provides additional degrees of freedom which may be used to control the distribution of electromagnetic fields. In particular, independent control of the driving amplitude and phase of individual current elements can be effective in correcting B_1 inhomogeneities – an approach generally referred to as RF shimming (50,55-57,88). RF shimming has been shown to be effective in improving B_1 homogeneity at high magnetic fields when an adequate number of coils is available (89). A recent study showed that SAR reduction may be achieved together with improved B_1 uniformity by optimizing the amplitudes and phases of the elements of a transmit array (90).

RF power deposition and B_1 homogeneity can also be controlled to some extent by pulse or pulse sequence design, for example using SAR-optimized flip angles (91), or variable-rate selective excitations (VERSE) (92). Hennig et al. have reported substantial SAR reductions in spin echo sequences using hyperecho techniques (93). Composite pulses have been used successfully with single coils (94) and coil arrays (95) to improve excitation homogeneity, and array-optimized composite pulse design can be also pursued for reducing local SAR levels (95). Parallel MRI techniques (15-17) may be used to decrease the number and frequency of RF excitations, thereby reducing total RF power deposition, albeit at the expense of signal to noise ratio (SNR).

Recently, parallel transmit MR techniques (58,59) – which combine multi-coil excitation and pulse design – have been explored with increasing interest. These techniques, which are generalizations of RF shimming with the additional capability to perform B_1 optimization in the time domain, were originally designed to accelerate complex excitation pulses, by analogy with the principles underlying parallel MRI. By driving each element of an array of transmit coils with a distinct tailored RF waveform, parallel excitation techniques enable the suppression of aliasing lobes resulting from reduction of the sampling density in excitation *k*-space. In these approaches, the composite B_1 field is modulated in space and time by adjusting the independent RF waveforms transmitted by each coil, and is combined with a suitable synchronous gradient waveform in order to generate a target excitation profile.

Early in the development of parallel transmit MR, it was also recognized that parallel transmission can be exploited to improve the homogeneity of RF excitations and to reduce SAR (59). These capabilities account in part for the great recent interest in parallel transmission as an enabling technology for high-field MRI. It should be noted, however, that the demands of pulse acceleration and the demands of SAR reduction may often be opposed, since calculation of the weights required to produce an accelerated excitation relies on the inversion of ill-conditioned sensitivity matrices, which may cause spatial amplification of SAR somewhat analogous to the spatial amplification of noise in parallel imaging (64). Also by analogy with the case of parallel reception, it is possible to derive a set of transmit coil waveforms which yield the minimum SAR for a given level of pulse acceleration (59).

Parallel transmission methods require prior knowledge of B_1 field distributions, as well as hardware capable of generating and amplifying multiple independent RF waveforms. In order to justify these additional investments in calibration and technology, it will be important to assess how well fully parallel transmission can perform. Katscher et al. have shown that suboptimal coil arrays may have a negligible effect on the quality of the excitation pattern in fully parallel transmission, whereas they dramatically affect SAR, even for slight variations in the spatial arrangement of individual elements (63). This result also suggests that it will be important to assess

the tradeoff between excitation fidelity or homogeneity and SAR. In this paper, we present a framework in which the homogeneity and SAR associated with various transmission approaches may be compared independent of any particular coil configuration. We also present a lower bound on SAR as a guide for future transmit coil array designs.

In the case of parallel imaging it has been shown that there is an inherent electrodynamic limitation to the achievable SNR of any physically realizable coil array, and the behavior of ultimate intrinsic SNR has been extensively studied (41,42,67). In those prior studies, receive coil sensitivities were expanded in a complete basis of valid solutions to Maxwell's equations and the optimal SNR was calculated by finding a linear combination that minimized the total noise power for unit signal strength. In this paper we use a similar approach to explore electrodynamic constraints on transmit homogeneity and SAR, by expanding putative transmit coil fields in a suitable basis to compute the ultimate intrinsic SAR for various excitation approaches. We explore the dependency of ultimate intrinsic SAR upon field strength and investigate the effects of varying the shape of the target excitation as well as the size of the imaged body (since wavelength effects can be strongly influenced by object size). In addition, we model the same excitation approaches using finite coil arrays of well-defined geometry, and compare their performance against the ultimate intrinsic case. In the case of fully parallel excitation, we investigate the relation between ultimate SAR and acceleration factor, and we determine the time-varying spatial distribution of RF power deposition within the subject during optimized excitation pulses.

Theory

In this section we begin by reviewing the general formalism of excitation with an array of transmit coils and then we describe a procedure for combining the individual coils' current waveforms in order to minimize RF power deposition in the subject while preserving a target net excitation profile. We then show a method to derive a

theoretical lower bound on this deposited power, by employing a complete basis set of transmit coil fields.

Multi-coil RF excitation formalism

It is often convenient to express the RF field generated by a transmit coil in a reference frame rotating at angular frequency equal to the Larmor frequency, as in this way the carrier term exp($i\omega t$) disappears from the equations. The principle of reciprocity, commonly used to calculate the strength of the MR signal, must be adapted accordingly. A rigorous formulation was provided by Hoult (70), who derived the following expressions for the magnetic field in the positively and negatively rotating frame, as a function of the components of the magnetic field in the static laboratory frame:

$$\begin{aligned} \tilde{\mathcal{B}}_1^+ &= \frac{\mathcal{B}_{1,x} + i\mathcal{B}_{1,y}}{2} \\ \tilde{\mathcal{B}}_1^- &= \frac{\left(\mathcal{B}_{1,x} - i\mathcal{B}_{1,y}\right)^*}{2} \end{aligned}, \tag{3.1}$$

where * indicates complex conjugation and $\mathcal{B}_{1,x}$ and $\mathcal{B}_{1,y}$ are the Cartesian components of the complex RF field amplitude generated by a coil in the laboratory frame (with the carrier terms removed). The RF excitation may be expressed in terms of $\tilde{\mathcal{B}}_1^+$, whereas, in accordance with the principle of reciprocity, the strength of the received MR signal is proportional to $\tilde{\mathcal{B}}_1^-$. Neglecting short-lived field transients and assuming a driven steady state which changes slowly as compared with the RF oscillation period, $\tilde{\mathcal{B}}_1^+$ can be separated into a spatially varying term and a temporal envelope:

$$\tilde{\mathcal{B}}_1^+(\mathbf{r},t) = b(\mathbf{r})\mathrm{I}(t) \tag{3.2}$$

It is important to remember that both factors on the right hand side of Eq. (3.2) are complex quantities: $b(\mathbf{r})$ because of its orientation in the positively rotating frame and $\mathrm{I}(t)$ because it is an oscillatory current which has a magnitude and a phase in time.

Let us now consider an array of transmit coils. Within the limits of the small tip-angle approximation, the transverse magnetization resulting from simultaneous excitation with L transmit coils can be derived using k-space Fourier analysis (59):

$$M(\mathbf{r}) = i\gamma M_0(\mathbf{r}) \sum_{l'=1}^{L} b_{l'}(\mathbf{r}) \int_k \sum_{l=1}^{L} c_{l',l} W_l(\mathbf{k}) S(\mathbf{k}) e^{i2\pi \mathbf{k}\cdot\mathbf{r}} d\mathbf{k}. \quad (3.3)$$

γ is the gyromagnetic ratio, i is the imaginary unit, M_0 is the equilibrium value of the nuclear magnetization, $b_l(\mathbf{r})$ is the complex spatial weighting induced by the $\tilde{\mathcal{B}}_1^+$ field pattern of the l^{th} component coil in the array, and $c_{l',l}$ are the coefficients that characterize the mutual coupling between the coils. In practice, rather than $b_{l'}(\mathbf{r})$, it is convenient to measure, by means of so-called B_1 maps, the effective spatial weighting $\hat{b}_l(\mathbf{r}) = \sum_{l'=1}^{L} c_{l',l} b_{l'}(\mathbf{r})$, which incorporates the mutual coupling. The product of the spatial-frequency weighting introduced by the l^{th} coil, $W_l(\mathbf{k})$, and the excitation k-space sampling trajectory controlled by the switching gradients, $S(\mathbf{k})$, represents the explicit weighting of k-space by the RF excitation and is defined as (96):

$$W_l(\mathbf{k})S(\mathbf{k}) = \int_0^T W_l(\mathbf{k}(t)) \left\{ {}^3\delta(\mathbf{k}(t) - \mathbf{k}) \left| \dot{\mathbf{k}}(t) \right| \right\} dt = \int_0^T \frac{\mathrm{I}_l(t)}{\left| \gamma \mathbf{G}(t) \right|} \left\{ {}^3\delta(\mathbf{k}(t) - \mathbf{k}) \left| \dot{\mathbf{k}}(t) \right| \right\} dt, \quad (3.4)$$

where $|\mathbf{G}(t)|$ is the amplitude of the linear gradients and ${}^3\delta$ the three-dimensional delta function. $\mathrm{I}_l(t)$ is the current circulating in the l^{th} coil and it is a measure of the amplitude of the RF field applied by the l^{th} coil to produce an ideal small tip-angle excitation at the voxel of interest in the current RF cycle.

The portion of Eq. (3.3) that defines the complex-valued excitation profile $\mu(\mathbf{r})$ can thus be re-written as:

$$\mu(\mathbf{r}) = \sum_{l=1}^{L} \hat{b}_l(\mathbf{r}) \int_k W_l(\mathbf{k}) S(\mathbf{k}) e^{i2\pi \mathbf{k}\cdot\mathbf{r}} d\mathbf{k} \quad (3.5)$$

Let us now consider the case of a 2D echo-planar excitation trajectory. Indicating positions on the trajectory with (k_x, k_y), we can define the periodic excitation pattern $f_l(x,y)$ associated with the RF pulse of the l^{th} transmit element as:

$$f_l(x,y) = \iint_{k_x,k_y} W_l(k_x,k_y) e^{i2\pi(k_x x + k_y y)} dk_x dk_y \tag{3.6}$$

(Note that, as compared with the original exposition in Ref. (59), we have changed notation for the excitation pattern from g to f so as to avoid confusion with the g-factor in parallel imaging). The periodic patterns are then combined to excite simultaneously the target profile. This translates into the following constraint for the $f_l(x,y)$'s in Eq. (3.6):

$$\sum_{l=1}^{L} f_l(x,y)\hat{b}_l(x,y) = \mu(x,y) \tag{3.7}$$

From Eq. (3.6) is clear that discrete sampling in the spatial-frequency domain (k_x, k_y) results in aliasing lobes in the x and y directions. If the sampling interval is sufficiently small, all the aliasing lobes occur outside the FOV and we need not include the periodicity of the $f_l(x,y)$ explicitly in the equation. This is the case for unaccelerated parallel transmission, which requires solving Eq. (3.7) for each voxel in the image separately.

RF power deposition with multiple transmit coils

The total electric field associated with the pth time-period in the RF excitation can be expressed as a linear combination of the electric fields generated by the L elements of the transmit array:

$$\mathbf{E}(\mathbf{r}, p\Delta t) = \sum_{l=1}^{L} \mathrm{I}_l(p\Delta t)\mathbf{e}_l(\mathbf{r}), \tag{3.8}$$

where $\mathrm{I}_l(p\Delta t)$ is the p-th complex-valued time-sample of the current applied for an interval Δt to the l^{th} transmit element or driving port, and $\mathbf{e}_l(\mathbf{r})$ denotes the complex-valued electric field which would be produced by the l^{th} coil if $\mathrm{I}_l(p\Delta t)$ were equal to 1.

The temporal window Δt is assumed small enough that the field amplitudes can be considered constant within it. The RF power dissipated in the subject over one excitation time period can be expressed as a quadratic function in the samples of the current waveforms:

$$\xi_p = \frac{1}{2}\iint_{V\,\Delta t} \sigma(\mathbf{r})\left|\mathcal{E}(\mathbf{r}, p\Delta t)\right|^2 dtdv$$

$$= \left(\mathrm{I}_1(p\Delta t)..\mathrm{I}_l(p\Delta t)..\mathrm{I}_L(p\Delta t)\right)^H \left(\frac{\Delta t}{2}\int_V \sigma(\mathbf{r}) \begin{pmatrix} \mathbf{e}_1(\mathbf{r}) \\ ... \\ \mathbf{e}_l(\mathbf{r}) \\ ... \\ \mathbf{e}_L(\mathbf{r}) \end{pmatrix}^* \left(\mathbf{e}_1(\mathbf{r})..\mathbf{e}_l(\mathbf{r})..\mathbf{e}_L(\mathbf{r})\right) dv \right) \begin{pmatrix} \mathrm{I}_1(p\Delta t) \\ ... \\ \mathrm{I}_l(p\Delta t) \\ ... \\ \mathrm{I}_L(p\Delta t) \end{pmatrix}$$

$$= \mathbf{I}_p^H \boldsymbol{\Phi}\, \mathbf{I}_p$$

(3.9)

$\sigma(\mathbf{r})$ is the conductivity of the sample, and the superscripts * and ^{H} denote, respectively, complex conjugate and conjugate (Hermitian) transpose. $\boldsymbol{\Phi}$ is a matrix which contains the overlap integrals of the electric fields from the individual coils and its elements are calculated as:

$$\Phi_{l,l'} = \int_V \sigma(\mathbf{r})\mathbf{e}_l(\mathbf{r})\cdot\mathbf{e}_{l'}^*(\mathbf{r})dv \tag{3.10}$$

(Note that Eq. (3.10) is equivalent, by reciprocity, to the expression for the noise correlation matrix between transmit elements if they were used in receive mode.) The samples of the current waveforms ($\mathrm{I}_l(p\Delta t)$) are related by Fourier transformation to the periodic patterns that define the excitation profile (see Eq. (3.4) and (3.6)):

$$W_{lp} \equiv W_l(k_x,k_y) = W_l(\mathbf{k}(p\Delta t)) = \frac{\mathrm{I}_l(p\Delta t)}{\left|\gamma\mathbf{G}(p\Delta t)\right|} \Rightarrow f_{ln} \equiv f_l(x,y) = \mathcal{F}\left[W_{lp}\right] \propto \mathcal{F}\left[\mathrm{I}_l(p\Delta t)\right]$$

(3.11)

where $\mathcal{F}$ indicates the Fourier transform, and n is an index of discrete voxel positions (x,y) considered in defining the excitation profile. The factor $\left|\gamma\mathbf{G}(p\Delta t)\right|$ has been absorbed into the proportionality on the right hand side of Eq. (3.11), as it remains constant for the EPI trajectory in question. Eq. (3.11) explicitly shows how time

dependence disappears from the remainder of the theory and becomes incorporated in the index p. The notation used here in fact indicates that, for each time period p, time-variant quantities are sampled only at time points corresponding to positions (k_x, k_y) lying on the excitation k-space trajectory. The mapping of k-space positions to spatial voxel locations by Fourier transformation applies also to the corresponding indices (p and n), as follows:

$$\begin{array}{ccc} (k_x,k_y) & \rightarrow & p \\ \Updownarrow_{\mathcal{F}} & & \Updownarrow_{\mathcal{F}} \\ (x,y) & \rightarrow & n \end{array} \tag{3.12}$$

Because of the property detailed in Eq.(3.11), we can apply Parseval's theorem to write RF power deposition using the f_{ln}'s:

$$\sum_{p=1}^{P} \mathbf{I}_p^H \, \mathbf{\Phi} \, \mathbf{I}_p = \sum_{p=1}^{P} \sum_{l=1}^{L} \sum_{l'=1}^{L} \mathrm{I}_{l'}^*(p\Delta t)\Phi_{l',l}\,\mathrm{I}_l(p\Delta t) = \sum_{l=1}^{L} \sum_{l'=1}^{L} \Phi_{l',l} \left(\sum_{p=1}^{P} \mathrm{I}_{l'}^*(p\Delta t)\mathrm{I}_l(p\Delta t) \right) \propto$$
$$\sum_{l=1}^{L} \sum_{l'=1}^{L} \Phi_{l',l} \left(\sum_{n=1}^{N} f_{l'n}^* f_{ln} \right) = \sum_{n=1}^{N} \sum_{l=1}^{L} \sum_{l'=1}^{L} f_{l'n}^* \Phi_{l',l}\, f_{ln} = \sum_{n=1}^{N} \mathbf{f}_n^H \, \mathbf{\Phi} \, \mathbf{f}_n \tag{3.13}$$

where P is the total number of time periods in the excitation and N is the total number of voxels. Using the result of Eq. (3.13) in Eq. (3.9), we can define the average RF power deposited in the sample during the excitation with two equivalent expressions:

$$\xi = \frac{1}{P} \sum_{p=1}^{P} \mathbf{I}_p^H \, \mathbf{\Phi} \, \mathbf{I}_p = \frac{1}{N} \sum_{n=1}^{N} \mathbf{f}_n^H \, \mathbf{\Phi} \, \mathbf{f}_n \,. \tag{3.14}$$

Optimal RF power deposition with fully parallel transmission

In fully parallel transmission tailored excitations are transmitted independently with the individual array elements. This means that each coil's base excitation pattern may vary independently voxel-by-voxel, since that coil's driving current pattern is free to vary independently over time. The expression in Eq. (3.7), which relates individual coil excitations to the target excitation profile, can be re-written as:

$$\sum_{l=1}^{L} f_{ln} \hat{b}_{ln} = \mu_n \,, \tag{3.15}$$

which represents N separate relations, each applicable at a particular voxel position. If we concatenate these relations into a single matrix equation, we obtain the following expression:

$$\begin{pmatrix} \hat{b}_{11} \dots \hat{b}_{l1} \dots \hat{b}_{L1} \dots 0 \dots 0 \dots 0 \dots 0 \dots 0 \dots 0 \\ \dots \dots \dots \dots \dots \dots \dots \dots \dots \dots \dots \dots \dots \dots \\ 0 \dots 0 \dots 0 \dots \hat{b}_{1n} \dots \hat{b}_{ln} \dots \hat{b}_{Ln} \dots 0 \dots 0 \dots 0 \\ \dots \dots \dots \dots \dots \dots \dots \dots \dots \dots \dots \dots \dots \dots \\ 0 \dots 0 \dots 0 \dots 0 \dots 0 \dots 0 \dots \hat{b}_{1N} \dots \hat{b}_{lN} \dots \hat{b}_{LN} \end{pmatrix} \begin{pmatrix} f_{11} \\ \dots \\ f_{l1} \\ \dots \\ f_{L1} \\ \dots \\ f_{1n} \\ \dots \\ f_{ln} \\ \dots \\ f_{Ln} \\ \dots \\ f_{1N} \\ \dots \\ f_{lN} \\ \dots \\ f_{LN} \end{pmatrix} = \begin{pmatrix} \mu_1 \\ \dots \\ \mu_n \\ \dots \\ \mu_N \end{pmatrix} \tag{3.16}$$

Here $\hat{b}_{ln} = \hat{b}_l(x_n, y_n)$, $f_{ln} = f_l(x_n, y_n)$, and $\mu_n = \mu(x_n, y_n)$. In more compact notation, we may write:

$$\mathbf{C}_{FOV}\mathbf{f}_{FOV} = \boldsymbol{\mu}_{FOV}, \tag{3.17}$$

with $\boldsymbol{\mu}_{FOV}$ representing a [N x 1] vector that contains the target profile, $\mathbf{f}_{FOV}$ being a [LN x 1] vector concatenating values of f as shown in Eq. (3.16), and the block-structured [N x LN] matrix $\mathbf{C}_{FOV}$ being a spatial-weighting map made up of transmit field values $\hat{b}_{ln}$.

Using Eq. (3.14) and the concatenated quantity $\mathbf{f}_{FOV}$, we can write an expression for the average RF power dissipated over the entire duration of the parallel excitation:

$$\xi = \frac{1}{N}\mathbf{f}_{FOV}^{H}\,\bar{\boldsymbol{\Phi}}\,\mathbf{f}_{FOV}, \tag{3.18}$$

where $\bar{\boldsymbol{\Phi}}$ is a block-diagonal matrix, with N copies of $\boldsymbol{\Phi}$ along the diagonal and zero elsewhere. The design of parallel excitation pulse sequences that yield minimization of RF power deposition consists in finding a set of coefficients for each time period, or, equivalently, a set of tailored excitation patterns at each voxel position, that leads to SAR minimization over the entire duration of the excitation. Combining Eq.'s (3.18) and (3.17), we see that the constrained minimization problem for fully parallel transmission can be summarized as (59):

$$\begin{aligned} &\text{minimize} \quad \xi = \frac{1}{N}(\mathbf{f}_{FOV}^{H}\, \bar{\boldsymbol{\Phi}}\, \mathbf{f}_{FOV}) \\ &\text{subject to} \quad \mathbf{C}_{FOV}\mathbf{f}_{FOV} = \boldsymbol{\mu}_{FOV} \end{aligned}, \tag{3.19}$$

Given the block structure of $\mathbf{C}_{FOV}$, the constraint in Eq. (3.19) can be seen as the concatenation of N constraints, each of which must be satisfied simultaneously in order to achieve the desired excitation pattern at all voxel positions. However, as the contribution to ξ from each voxel position in the sum shown in Eq. (3.14) is positive definite, we can subdivide Eq (3.19) and separately optimize the current patterns for each target position, (since the sum of separately obtained minimum SAR contributions $\mathbf{f}_n^H\, \boldsymbol{\Phi}\, \mathbf{f}_n$ will remain the minimum achievable total SAR). Application of Lagrange multipliers to solve each sub-problem in Eq (3.19) yields the following solution, previously shown in Ref. (64):

$$\tilde{\mathbf{f}}_n = \boldsymbol{\Phi}^{-1}\mathbf{C}_n^H(\mathbf{C}_n\boldsymbol{\Phi}^{-1}\mathbf{C}_n^H)^{-1}\boldsymbol{\mu}_n. \tag{3.20}$$

The tilde in $\tilde{\mathbf{f}}_n$ indicates that this choice of the individual excitation patterns is optimal in the least-squares sense. Substituting in Eq. (3.18), we obtain the minimum average SAR:

$$\tilde{\xi} = \frac{1}{N}\sum_{n=1}^{N}\left[\boldsymbol{\mu}_n^H(\mathbf{C}_n\boldsymbol{\Phi}^{-1}\mathbf{C}_n^H)^{-1}\boldsymbol{\mu}_n\right] \tag{3.21}$$

In Eq. (3.21), SAR is optimized for each voxel position (or, equivalently by application of Parseval's theorem, for each excitation time period) and then averaged.

Algorithmically, this involves a loop over voxel positions to accumulate global SAR contributions.

One further subtlety to note is that each contribution $\boldsymbol{\mu}_n^H (\mathbf{C}_n \boldsymbol{\Phi}^{-1} \mathbf{C}_n^H)^{-1} \boldsymbol{\mu}_n$ to the sum in Eq. (3.21) represents **not** the local SAR at the n^{th} voxel position, but rather the contribution to global SAR associated with the achieving of the target excitation at that position within the FOV. With the results of our optimization in hand, however, it is straightforward to compute local SAR at any position. If we weight the electric fields produced when the individual coils are driven by a unit current (see Eq. (3.8)) with the inverse Fourier transform of the corresponding elements of $\tilde{\mathbf{f}}_n$, which is proportional to the coils' actual driving current (see Eq. (3.11)), we can compute the spatially dependent net electric field generated during each time period of the SAR-optimized excitation. Knowledge of the net electric field during each excitation sampling interval enables calculation of power deposition at any particular location as a function of time and thus provides us with a spatial distribution of SAR as the excitation proceeds through excitation *k*-space. For each time period in the SAR-optimized excitation, the resulting local SAR at any position in the sample is:

$$\xi^{\text{local}}(\mathbf{r}, p\Delta t) \propto \sigma(\mathbf{r}) \left| \sum_{l=1}^{L} \mathcal{F}^{-1}\left[\tilde{f}_{ln} \right] \mathbf{e}_l(\mathbf{r}) \right|^2 \tag{3.22}$$

Pulse design for accelerated parallel excitations

If the sampling interval in excitation *k*-space is not sufficiently small, aliasing lobes will occur inside the excited FOV. In the case of under-sampling along k_x with sampling interval Δk_x, we can re-write Eq. (3.7), suppressing the z-dependence for simplicity, as:

$$\mu(x,y) = \sum_{l=1}^{L} \hat{b}_l(x,y) \sum_{m=0}^{M-1} f_l(x - m\Delta_x, y), \tag{3.23}$$

where M-1 is the number of aliasing lobes inside the FOV and $\Delta_x = 1/\Delta k_x$. Once again, the aliasing lobes outside the FOV are omitted (otherwise m would range from $-\infty$ to $+\infty$). In the case of $M = 1$, which corresponds to unaccelerated excitations, and

discretizing to discrete voxel positions, we recover the voxel-by-voxel subproblems of Eq. (3.16), i.e.

$$\left(\hat{b}_1(x_n,y_n)\ \ldots\ \hat{b}_l(x_n,y_n)\ \ldots\ \hat{b}_L(x_n,y_n)\right)\begin{pmatrix} f_1(x_n,y_n) \\ \ldots \\ f_l(x_n,y_n) \\ \ldots \\ f_L(x_n,y_n) \end{pmatrix} = \mu(x_n,y_n). \qquad (3.24)$$

In parallel excitation techniques, the number of time periods necessary to excite a target profile is reduced by lengthening the sampling interval, and by weighting the aliased excitation patterns of the independent transmission elements to eliminate aliasing in the combined excitation. Thus, in the general case of $M > 1$ Eq. (3.23) translates into a set of M linear equations:

$$\begin{pmatrix} \hat{b}_1(x_n,y_n) & \ldots & \hat{b}_l(x_n,y_n) & \ldots & \hat{b}_L(x_n,y_n) \\ \ldots & \ldots & \ldots & \ldots & \ldots \\ \hat{b}_1(x_n+m\Delta_x,y_n) & \ldots & \hat{b}_l(x_n+m\Delta_x,y_n) & \ldots & \hat{b}_L(x_n+m\Delta_x,y_n) \\ \ldots & \ldots & \ldots & \ldots & \ldots \\ \hat{b}_1(x_n+M\Delta_x,y_n) & \ldots & \hat{b}_l(x_n+M\Delta_x,y_n) & \ldots & \hat{b}_L(x_n+M\Delta_x,y_n) \end{pmatrix}\begin{pmatrix} f_1(x_n,y_n) \\ \ldots \\ \ldots \\ f_l(x_n,y_n) \\ \ldots \\ f_L(x_n,y_n) \end{pmatrix} = \begin{pmatrix} \mu(x_n,y_n) \\ \ldots \\ \mu(x_n+m\Delta_x,y_n) \\ \ldots \\ \mu(x_n+M\Delta_x,y_n) \end{pmatrix}$$

(3.25)

The SAR optimization problem for accelerated parallel transmission may be formulated precisely as in Eq. (3.19), with the difference that all sums over n run from one to N/M and the optimization is performed over sets of M aliased voxels rather than for each voxel independently.

This formulation, of course, has a strong counterpart in formulation of the weak Cartesian SENSE parallel image reconstruction (16). In fact, when we assume a fully homogeneous target excitation profile (i.e. $\mu(x_n,y_n)=1$ and $\mu(x_n+m\Delta_x,y_n)=0$ for all m), and exchange the transmit field $\tilde{\mathcal{B}}_1^+$ for the receive field $\tilde{\mathcal{B}}_1^-$, then the expression for each voxel's SAR contribution in our optimization is equivalent to the inverse square of the expression for voxelwise SNR in weak Cartesian SENSE.

Optimal RF power deposition with time-independent RF optimization

The same optimization can be applied to a special case of parallel transmission, which has fewer degrees of freedom and does not allow for accelerated excitations. In RF shimming, or B_1 shimming, all coils share a common current waveform with only a single time-independent phase and amplitude distinguishing each channel. In order to optimize the performance of RF shimming, we can search, among all possible modulations, for the one set of phases and amplitudes that minimizes RF power deposition while removing, to the greatest extent possible, B_1 inhomogeneities.

Traditionally, RF shimming has been performed using single slice-selective pulses, in which case the excitation k-space trajectory reduces to a single non-zero amplitude at $(k_x, k_y) = 0$ played out in the presence of a slice-select gradient. In order to derive RF shimming as a special case of the general formalism, we begin by assuming the more general excitation k-space trajectory used for fully parallel transmission, but in this case shared among all coils. We discuss other possible excitation strategies at the end of the section and in "Materials and Methods".

If we indicate with A_l and φ_l the amplitude and phase used to modulate the current at the l^{th} coil or driving port for RF shimming, we can express this current as:

$$I_l(p\Delta t) = A_l e^{i\varphi_l} I(p\Delta t) = \alpha_l I_p \tag{3.26}$$

where α_l is a complex coefficient and I_p is the current generated by the RF source at time-period p. Knowing that the spatial frequency weights W_{lp} are proportional to the currents $I_l(p\Delta t)$ and that the currents are sampled only along the k-space trajectory (see Eq. (3.11)), we can make the integral in Eq. (3.6) discrete and re-write the equation for the case of RF shimming:

$$f_l(x,y) = f_{ln} \propto \sum_{p=1}^{P} I_l(p\Delta t) e^{i2\pi(k_{p,x}x + k_{p,y}y)} = h_n \alpha_l \tag{3.27}$$

where we define the common excitation pattern shared by all transmit array elements as:

$$h_n = \sum_{p=1}^{P} \mathrm{I}_p e^{i2\pi(k_{p,x}x + k_{p,y}y)} . \tag{3.28}$$

This common excitation pattern results from the shared RF waveform combined with the common applied field gradients. For each transmit element, of course, this shared pattern will be modulated by that element's transmit field pattern. Substituting in Eq. (3.7) and using the index n to indicate voxel locations, we obtain:

$$\sum_{l=1}^{L} f_{ln}\hat{b}_{ln} = h_n \sum_{l=1}^{L} \alpha_l \hat{b}_{ln} = \mu_n .. \tag{3.29}$$

Substituting Eq. (3.27) into Eq. (3.13), we can express the RF power deposited in the sample during the excitation of the target profile as a quadratic function in the RF shimming coefficients α_l:

$$\xi = \frac{1}{N}\left(\sum_{n=1}^{N}|h_n|^2\right)\sum_{l=1}^{L}\sum_{l'=1}^{L}\alpha_{l'}^{*}\Phi_{l',l}\alpha_l = \frac{1}{N}\left(\sum_{n=1}^{N}|h_n|^2\right)\left(\boldsymbol{\alpha}^H\boldsymbol{\Phi}\,\boldsymbol{\alpha}\right) \tag{3.30}$$

Optimization of RF shimming performance, then, involves adjusting the α_l's, for any given choice of common profile h_n, to minimize the expression for SAR in Eq. (3.30) while preserving to the greatest extent possible the desired net excitation profile μ_n as specified by Eq. (3.29). This reduces to the following constrained minimization problem:

$$\begin{aligned} &\text{minimize } \left(\boldsymbol{\alpha}^H\boldsymbol{\Phi}\,\boldsymbol{\alpha}\right) \\ &\text{subject to } \mathbf{S}_{FOV}\boldsymbol{\alpha} = \frac{\boldsymbol{\mu}_{FOV}}{\mathbf{h}_{FOV}} \end{aligned} \tag{3.31}$$

$\mathbf{S}_{FOV}$ is a [N x L] spatial-weighting map made up of transmit field values $\hat{b}_{ln}$, $\boldsymbol{\alpha}$ is a [L x 1] vector containing the unknown complex modulation coefficient for each transmit coil, $\boldsymbol{\mu}_{FOV}$ represents the same [N x 1] vector that appears in Eq. (3.19) and $\mathbf{h}_{FOV}$ is a [N x 1] vector that contains the common excitation pattern at each voxel position of the FOV. The quotient on the right hand side of Eq. (3.31) represents an element-by-element division, derived from Eq. (3.29) and reflecting the fact that it is only the

relative differences between the starting common profile and the target profile which must be adjusted by RF shimming. The optimization in Eq. (3.31) is performed simultaneously for all voxels and the accuracy with which the homogeneity constraint is satisfied is strongly affected by the number of transmit elements, i.e. the number of columns in $\mathbf{S}_{FOV}$, as we can see better by expanding the matrix elements:

$$\begin{pmatrix} \hat{b}_1(x_1,y_1) & \dots & \hat{b}_l(x_1,y_1) & \dots & \hat{b}_L(x_1,y_1) \\ \dots & \dots & \dots & \dots & \dots \\ \hat{b}_1(x_n,y_n) & \dots & \hat{b}_l(x_n,y_n) & \dots & \hat{b}_L(x_n,y_n) \\ \dots & \dots & \dots & \dots & \dots \\ \hat{b}_1(x_N,y_N) & \dots & \hat{b}_l(x_N,y_N) & \dots & \hat{b}_L(x_N,y_N) \end{pmatrix} \begin{pmatrix} \alpha_1 \\ \dots \\ \dots \\ \alpha_l \\ \dots \\ \dots \\ \alpha_L \end{pmatrix} = \begin{pmatrix} \dfrac{\mu(x_1,y_1)}{h(x_1,y_1)} \\ \dots \\ \dfrac{\mu(x_n,y_n)}{h(x_n,y_n)} \\ \dots \\ \dfrac{\mu(x_N,y_N)}{h(x_N,y_N)} \end{pmatrix} \tag{3.32}$$

The solution of this matrix equation, detailed in Appendix A, yields the optimal modulation coefficients:

$$\tilde{\boldsymbol{\alpha}} = \boldsymbol{\Phi}^{-1}\mathbf{S}_{FOV}^{H}(\mathbf{S}_{FOV}\boldsymbol{\Phi}^{-1}\mathbf{S}_{FOV}^{H})^{-1}\frac{\boldsymbol{\mu}_{FOV}}{\mathbf{h}_{FOV}} \tag{3.33}$$

The resulting minimum SAR value is obtained by substituting $\tilde{\boldsymbol{\alpha}}$ into Eq. (3.30):

$$\tilde{\xi} = \frac{1}{N}\left(\sum_{n=1}^{N}|h_n|^2\right)\left[\left(\frac{\boldsymbol{\mu}_{FOV}}{\mathbf{h}_{FOV}}\right)^{H}(\mathbf{S}_{FOV}\boldsymbol{\Phi}^{-1}\mathbf{S}_{FOV}^{H})^{-1}\frac{\boldsymbol{\mu}_{FOV}}{\mathbf{h}_{FOV}}\right] \tag{3.34}$$

This value represents, in effect, the SAR achieved with the best possible fixed combination of transmit coils otherwise sharing the same RF waveform. The actual excited profile, achieved when the optimal coefficients are applied to the coils, can be calculated by substituting $\tilde{\boldsymbol{\alpha}}$ into Eq. (3.31). If the number of transmit elements L were greater than or equal to the number of target excitation voxels N and the transmit fields of the various elements were sufficiently distinct, than any two-dimensional profile could be matched within the voxel resolutio n in a target image plane. (The fidelity of excitations in three dimensions is limited by the constraints of Maxwell's equations (55).) Subvoxel variations between the target voxel centers are always present, as in the analogous case of weak SENSE reconstruction for parallel reception (16).

Numerical errors in or regularization of the inverse in Eq. (3.33) will result in additional deviations from the target profile. Furthermore, just as inversion of ill-conditioned coil sensitivity matrices in the SENSE formulation of parallel image reconstruction results in noise amplification, ill-conditioning in the transmit sensitivity matrix $\mathbf{S}_{FOV}$ here can result in amplification of SAR in Eq. (3.34). Thus, SAR would appear to be the principal price paid for maximum adherence to a target excitation profile.

A few comments about the choice of common excitation profile $\mathbf{h}_{FOV}$ are in order. $\mathbf{h}_{FOV}$ represents the spatial excitation profile produced by the shared RF current waveform together with the applied gradient waveform, prior to modulation by individual transmit coil field patterns. The particular form of $\mathbf{h}_{FOV}$ may be chosen according to the problem of interest: for example, if we choose to set $\mathbf{h}_{FOV} = \boldsymbol{\mu}_{FOV}$, the task of RF shimming is simply to correct for the additional modulations produced by the transmit element field patterns. If instead we choose to set $\mathbf{h}_{FOV} \neq \boldsymbol{\mu}_{FOV}$, then we would be also relying upon the RF shimming procedure to compensate for any deficiencies in the combined RF and gradient waveforms. In this work we explore both situations.

If we set $\mathbf{h}_{FOV} = 1$ everywhere, our general formalism reduces to the familiar case of single slice-selective pulses at (k_x, k_y) = 0. More recently, other RF optimization techniques have been proposed using multi-spoke excitation trajectories (97,98), which apply non-zero RF amplitudes at a small number of carefully chosen (k_x, k_y) values, each in the presence of a slice-select gradient. Multi-spoke trajectories can be seen as an intermediate case between RF shimming and fully parallel transmission. Indeed, both the slice-selective pulses at (k_x, k_y) = 0 typical of RF shimming and the slice-selective pulses with multi-spoke k-space traversal employ relatively simple k-space sampling patterns and RF pulse temporal relationships, and both can be viewed as special cases of parallel transmission. Multi-spoke excitation expands, compared to RF shimming, excitation profile control in the (x,y) plane. Meanwhile, it implements a

practical tradeoff scheme among in-plane profile, slice profile and RF pulse length. Further tradeoffs are possible in the general framework of parallel transmission. Multi-spoke approaches may be accommodated in a straightforward manner in our formalism, with the common excitation $\mathbf{h}_{FOV}$ being defined by any chosen set of spoke amplitudes. In fact, homogeneity- and SAR-optimized choices of spoke amplitudes may also be determined as part of the design, through small modifications of the minimization problem of Eq. (3.31). In this case, the set of weights $\boldsymbol{\alpha}$ would be expanded to include a complex weight not only for each coil but also for each spoke amplitude. Meanwhile, the column space of the $\mathbf{S}_{FOV}$ matrix would also be expanded by a factor equal to the number of spokes, with columns now containing the values $\hat{b}_l(x_n, y_n)\exp(ik_x x_n + ik_y y_n)$ for each chosen spoke location (k_x, k_y). Such an expansion of the number of degrees of freedom represents a step in the direction of fully parallel transmission.

Theoretical lower bound on the RF power deposition: ultimate intrinsic SAR

The tailored excitation patterns in Eq. (3.20) and the modulation coefficients in Eq. (3.33) result in the minimization of power deposition in RF shimming and fully parallel transmission, respectively. Increasing the number of elements in the transmit array would increase the number of degrees of freedom available for the optimizations in Eq. (3.19), and (3.31), allowing improved management of the energy employed in the excitation and therefore leading to further reduction of the average RF power deposited in the subject. Indeed, for any given array, if any element were added whose net effect was to increase global SAR (and its contribution were not essential to achieving the target excitation), the optimization would automatically assign it a weight of zero. In order to find the theoretical minimum value of SAR for a given excitation trajectory, then, one can in principle add new RF sources into the pulse optimization until no further reduction in power deposition is observed. Though adding arbitrary new RF sources without perturbing existing sources would be difficult in practice, the computational procedure of performing the optimization with a suitable basis of transmitters (or, alternatively, of RF electromagnetic fields) results in a lower limit on

the attainable SAR, which we shall refer to as the ultimate intrinsic SAR. Such a procedure is closely related to methods which have recently been used to compute ultimate intrinsic SNR for parallel imaging (41,42).

For the remainder of the theory to follow we suppose that all transmit elements, as well as all receive coils, are positioned outside the body, which is assumed to be homogeneous. Such a condition enables us to express the fields arising in the sample at each time period in the excitation as solutions of the source-free Maxwell's equations. In accordance with previous studies of ultimate intrinsic SNR (41,42), the net field $\mathcal{E}^{net}$ and $\mathcal{B}^{net}$, generated by a hypothetical net transmit coil, can be expressed as the time-dependent linear combination of the contributions of a complete set of basis fields $\mathbf{e}_l$ and $\mathbf{b}_l$:

$$\begin{aligned} \mathcal{E}^{net}(\mathbf{r}, p\Delta t) &= \sum_l \beta_l(p\Delta t)\mathbf{e}_l(\mathbf{r}) \\ \mathcal{B}^{net}(\mathbf{r}, p\Delta t) &= \sum_l \beta_l(p\Delta t)\mathbf{b}_l(\mathbf{r}) \end{aligned} \tag{3.35}$$

In order to find the theoretical lower bound on the RF power deposited in a given subject during a particular RF excitation, we must find the weights $\beta_l(p\Delta t)$ that produce the desired excitation profile with the smallest possible RF energy deposition.

In contrast to the case of ultimate intrinsic SNR (41,42), which uses $\tilde{\mathcal{B}}_1^-$, for this calculation we use $\tilde{\mathcal{B}}_1^+$, and thus $(b_{l,x} + i\, b_{l,y})$, the spatially varying component of the right-hand circularly polarized magnetic fields in the basis set, accounts for the transmit sensitivity patterns of the individual hypothetical transmit elements. (The harmonic time dependence of the basis fields has been removed by transformation to the rotating frame, and all other time dependence has been incorporated into the weights β_l.) These field values constitute the matrix elements of $\mathbf{C}_n$ in Eq. (3.21) and $\mathbf{S}_{FOV}$ in Eq. (3.34). Substituting the $\mathbf{e}_l(\mathbf{r})$'s of the basis set to calculate the entries of $\mathbf{\Phi}$ in Eq. (3.9), we can compute $\tilde{\xi}_{\text{ultimate}}$ - a quantity that, up to scaling factors, is a measure of the ultimate intrinsic SAR.

The optimal weights β_l can be then calculated by inverse Fourier transformation (see Eq. (3.11)) of the tailored excitation patterns f_{ln} which are found by using the selected basis set in Eq. (3.20) and Eq. (3.33). The resulting $\beta_l(p\Delta t)$ in our case are equal to the spatial-frequency weighting functions $W_l(\mathbf{k}(p\Delta t))$ in Eq. (3.11), which in turn are equal to the optimal complex current waveforms that must be applied to the individual driving ports at each time period, multiplied by a constant factor accounting for the regular application of the gradients in the EPI trajectory. If we then substitute these weights into the expression for the net electric field we can compute the time-varying local SAR as:

$$\xi^{\text{local}}_{\text{basis set}}(\mathbf{r}, p\Delta t) \propto \sigma(\mathbf{r}) \left| \sum_{l}^{\text{basis set}} \beta_l(p\Delta t)\mathbf{e}_l(\mathbf{r}) \right|^2 \tag{3.36}$$

Eq. (3.36) yields a relative measure of local RF power deposition during the excitation that results in the theoretical smallest global SAR. $\xi^{\text{local}}_{\text{basis set}}$ does not necessarily represent the lowest possible SAR at every position $\mathbf{r}$ for any time-period p, but, rather, it represents the local consequences of the choice of weights that lead to the global SAR value $\tilde{\xi}_{\text{ultimate}}$ over the total duration of the excitation and the entire volume of the sample. Direct minimizations of local SAR at any particular spatial position could in fact be performed using our current formalism with the spatial integration inherent in the matrix $\mathbf{\Phi}$ removed, but such minimizations would necessarily occur at the expense of SAR elsewhere in the volume, and we have chosen to retain global SAR as our principal optimization parameter. (One could conceive of attempting simultaneous optimization of multiple local SAR values as a consensus among competing optima, but such an approach would represent a more complicated goal-attainment problem for which the simple linear algebraic formulation used here would not apply). Henceforward, we shall refer to $\xi^{\text{local}}_{\text{basis set}}$ as ultimate intrinsic local SAR.

For an appropriately constructed field basis set, the value of $\tilde{\xi}_{\text{ultimate}}$ will eventually converge at some finite value of the index l. Convergence may be tested by performing

the optimization for increasing values of l. Converged values for ultimate intrinsic SAR may then be compared with SAR values obtained by using finite transmit coil arrays with defined conductor geometries, to assess how closely the ultimate value may be approached with physically realizable arrays. The choice of basis for ultimate SAR computations and the methodology for comparison with finite transmit arrays are outlined in "Materials and Methods" to follow.

Materials and Methods

Choice of basis functions for ultimate intrinsic SAR calculations

The numerical complexity of solving the optimization problems in Eq. (3.19) and Eq. (3.31) using a complete basis of EM fields is affected by the choice of the basis functions and by the geometry of the object modeled in the simulations. For this reason, in the present work the sample was modeled as a homogeneous sphere and a multipole expansion of electromagnetic fields was used (42,71,99). Multipole electric and magnetic fields have the advantage of orthogonality over the sphere, which simplifies various expressions in the calculation and provides some confidence regarding convergence. Wiesinger et al. (42) showed that the multipole basis set enables convenient calculation of ultimate intrinsic SNR for the sphere. We employed a similar computational framework to calculate ultimate SAR, with attention to unique constraints of transmission as opposed to reception. Furthermore, this approach allows for direct comparison of the ultimate intrinsic SAR with the best attainable SAR values for a finite number of circular coils arranged on the sphere surface, as a semi-analytical solution for the EM fields of these coils can be derived as a special case of the multipole expansion (60,99,100).

Following Eq. [B3] of Ref. (42), the multipole electromagnetic fields are given by

$$\mathcal{E}^{\text{basis set}}(r,\vartheta,\phi)=\frac{\omega\mu}{k^{\text{in}}}\sum_{l=0}^{\infty}\sum_{m=-l}^{l}\left\{\beta_{l,m}^{\text{E}}\left[\frac{i}{k^{\text{in}}r}\frac{\partial(r\,\mathrm{j}_l(k^{\text{in}}r))}{\partial r}\left(\hat{\mathbf{r}}\times\mathbf{X}_{lm}(\vartheta,\phi)\right)\right.\right.$$
$$\left.\left.-\frac{\sqrt{l(l+1)}}{k^{\text{in}}r}\mathrm{j}_l(k^{\text{in}}r)\mathrm{Y}_l^m(\vartheta,\phi)\hat{\mathbf{r}}\right]+\beta_{l,m}^{\text{M}}\mathrm{j}_l(k^{\text{in}}r)\mathbf{X}_{lm}(\vartheta,\phi)\right\}$$
$$\mathcal{B}^{\text{basis set}}(r,\vartheta,\phi)=\mu\sum_{l=0}^{\infty}\sum_{m=-l}^{l}\left\{\beta_{l,m}^{\text{E}}\mathrm{j}_l(k^{\text{in}}r)\mathbf{X}_{lm}(\vartheta,\phi)\right.$$
$$\left.-\beta_{l,m}^{\text{M}}\left[\frac{i}{k^{\text{in}}r}\frac{\partial(r\,\mathrm{j}_l(k^{\text{in}}r))}{\partial r}\left(\hat{\mathbf{r}}\times\mathbf{X}_{lm}(\vartheta,\phi)\right)-\frac{\sqrt{l(l+1)}}{k^{\text{in}}r}\mathrm{j}_l(k^{\text{in}}r)\mathrm{Y}_l^m(\vartheta,\phi)\hat{\mathbf{r}}\right]\right\}$$

(3.37)

Here k^{in} is the wave number inside the sphere, defined as $\left(k^{in}\right)^2=\omega\mu\left(\omega\varepsilon+i\sigma\right)$ where σ and ε are the electrical conductivity and electric permittivity, respectively, of the sphere contents. $\mathrm{j}_l(k^{\text{in}}r)$ is the spherical Bessel function of the first kind, Y_l^m are scalar spherical harmonics and $\mathbf{X}_{lm}$ the corresponding vector spherical harmonics defined as $\mathbf{X}_{lm}(\vartheta,\phi)=\left(-i/\sqrt{l(l+1)}\right)(\mathbf{r}\times\nabla)\mathrm{Y}_l^m(\vartheta,\phi)$ (with the full position vector $\mathbf{r}$ replacing the unit vector $\hat{\mathbf{r}}$ in Eq. B2 of Ref. (42)). $\beta_{l,m}^{\text{E}}$ and $\beta_{l,m}^{\text{M}}$ denote expansion coefficients of electric-source and magnetic-source multipole basis functions, respectively. Letting the transmit-element/mode index range over both l and m, the set of weights $\boldsymbol{\beta}(p\Delta t)\equiv\left\{\beta_{l,m}^{\text{E}}(p\Delta t),\beta_{l,m}^{\text{M}}(p\Delta t)\right\}$ were optimized following the procedures outlined in previous sections.

In order to calculate the noise covariance matrix $\boldsymbol{\Phi}$ and the coil sensitivities we followed with minor changes the method outlined in Appendix B of Ref. (42). More precisely, Eq. [B7] of Ref. (42) was multiplied by the conductivity of the sample, to correct for a minor typographical error, and, to model RF transmission, coil sensitivities were computed using the right-hand rather than the left-hand circularly polarized component of the magnetic field.

Table 1.
Dielectric properties of average brain tissue obtained from Reference 26

Bo [T]	1	3	5	7	9	11
Larmor Frequency [MHz]	42.6	127.7	212.9	298.1	383.2	468.4
Dielectric Constant ε_r	102.5	63.1	55.3	52	50	48.8
Conductivity σ [1/Ωm]	0.36	0.46	0.51	0.55	0.59	0.62

The electromagnetic properties of the material in the homogeneous sphere at various magnetic field strengths were chosen to approximate values in the head, as given in Table 1. The FOV is a transverse square section through the center of the sphere, with the side length equal to the sphere's diameter (Figure 3-1). We assumed image matrix size to be 32-by-32 voxels. (This choice was made for practical reasons of computation time, but larger matrix sizes are certainly possible.) SAR was calculated for concentric excitation profiles with three different radii, equal to 100%, 50%, or 25% of the radius of the sphere (Figure 3-1). Homogeneity of the target excitations was also varied as described further in Results to follow. All calculations were implemented using MATLAB (Mathworks, Natick, USA) on a standard PC.

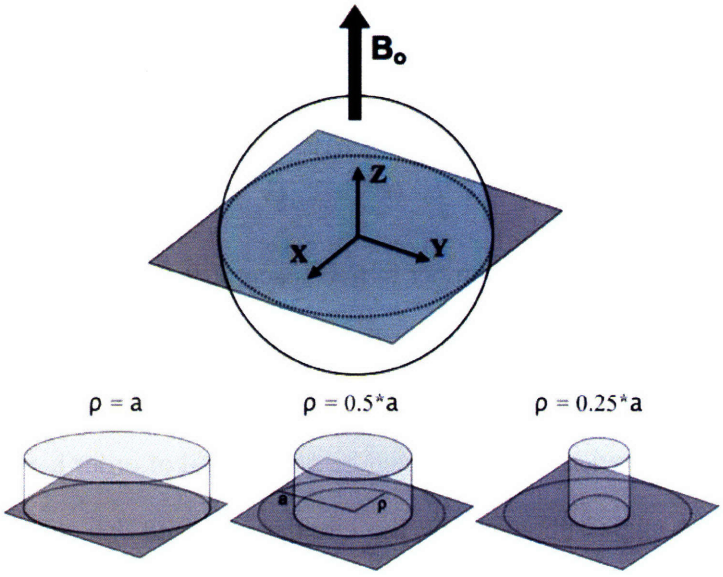

Figure 3-1. Schematic representation of the sample geometry, the FOV and the shape of the target excitation profiles. Fully homogeneous concentric excitation profiles were modeled with radius equal to 100%, 50%, and 25% of the radius of the sphere. Smoothly varying excitation profiles with the same set of radii were also tested, and are shown in subsequent figures.

Circular surface coils

The full-wave solution of the electromagnetic field produced by a circular surface coil adjacent to a homogeneous sphere (Figure 3-2) can be expressed in the form of a semi-analytical multipole expansion (99):

$$\begin{aligned}\mathcal{E}^{\text{coil}}(r,\vartheta,\phi) &= \frac{\omega}{k^{\text{in}}}\sum_{l=1}^{\infty}\beta_{l,0}^{\text{M}}\,\mathrm{j}_l(k^{\text{in}}r)\mathbf{X}_{l0}(\vartheta,\phi)\\ \mathcal{B}^{\text{coil}}(r,\vartheta,\phi) &= \sum_{l=1}^{\infty}\left[\frac{1}{k^{\text{in}}r}\beta_{l,0}^{\text{M}}\sqrt{l(l+1)}\,\mathrm{j}_l(k^{\text{in}}r)\mathrm{Y}_l^0(\vartheta,\phi)\hat{\mathbf{r}}\right.\\ &\qquad\left.-\frac{i}{k^{\text{in}}r}\beta_{l,0}^{\text{M}}\frac{\partial(r\,\mathrm{j}_l(k^{\text{in}}r))}{\partial r}\left(\hat{\mathbf{r}}\times\mathbf{X}_{l0}(\vartheta,\phi)\right)\right]\end{aligned}, \qquad (3.38)$$

$w_{l,0}^{\text{M}}$ is the expansion coefficient of magnetic-source multipole basis functions (99), derived by applying appropriate boundary conditions at the surface of a homogeneous dielectric sphere to the unconstrained fields in Eq. (3.37):

$$\beta_{l,0}^{\mathrm{M}} = \mu I 2\pi \sqrt{\frac{(2l+1)}{4\pi l(l+1)}} \frac{(k^{\mathrm{out}})^2 R^2 h_l^{(1)}(k^{\mathrm{out}}\sqrt{d^2+R^2})}{\sqrt{d^2+R^2}} \frac{dP_l(\eta)}{d\eta} \times \frac{k^{\mathrm{in}}(\mathrm{j}_l(k^{\mathrm{out}}a)y_{l+1}(k^{\mathrm{out}}a) - y_l(k^{\mathrm{out}}a)\mathrm{j}_{l+1}(k^{\mathrm{out}}a))}{k^{\mathrm{in}}h_l^{(1)}(k^{\mathrm{out}}a)\mathrm{j}_{l+1}(k^{\mathrm{in}}a) - k^{\mathrm{out}}\mathrm{j}_l(k^{\mathrm{in}}a)h_{l+1}^{(1)}(k^{\mathrm{out}}a)} \quad (3.39)$$

$k^{\mathrm{out}} = \omega\sqrt{\mu_0\varepsilon_0}$ is the wave number in free space, R is the radius of the circular coil, a is the radius of the sphere, d is the distance between the center of the coil and the center of the sphere, I is the current circulating in the coil (assumed to be normalized to unity throughout this work), P_l is the Legendre polynomial of order l, $\eta = d/\sqrt{d^2+R^2}$ is the cosine of the angle subtended by the circular coil, and $h_l^{(1)}$ and y_l are the spherical Bessel functions of the second and third kinds, respectively.

The EM fields in Eq. (3.38) can be appropriately rotated in order to express the EM fields of an identical circular coil at a different position near the surface of the sphere, with respect to the same reference frame of the sample (see Appendix B and Figure 3-2). In order to model finite arrays of surface coils, we followed a procedure outlined by Wiesinger et al in Ref. (60,100) to distribute circular coils as evenly as possible around a spherical surface concentric with the imaged sphere. The radius $\sqrt{d^2+R^2}$ of the spherical surface on which the coils are placed was 10% larger than the radius a of the imaged sphere. Transmit arrays with element numbers ranging from 1 to 64 were simulated in this way, and the resulting sets of coil fields were subjected to the identical optimization algorithms as the multipole fields used for ultimate intrinsic SAR computations. SAR and homogeneity results were then compared with ultimate intrinsic results. It is clear from the formulation of the coil electromagnetic fields in Eq. (3.38) that any finite array will perform worse than our ultimate intrinsic limit, even if the mode expansion is carried out to a finite mode order l_{max}, since the complete multipole basis of Eq. (3.37) may be regenerated by removing boundary condition constraints to allow $m \neq 0$ terms, and by including electric-source terms, both of which will necessarily increase the number of degrees of freedom for homogeneity correction and SAR control.

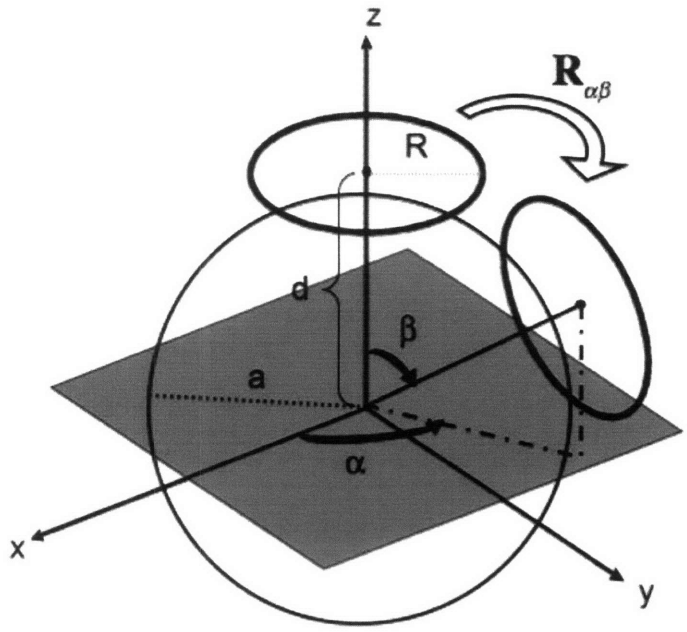

Figure 3-2. Schematic arrangement of two circular surface coils near the surface of a homogeneous sphere. The sphere is centered at the origin of the laboratory reference frame.

For completeness, we also computed SAR and homogeneity for transmission in single surface coils or simple fixed sums of coils, in order to assess the degree of benefit afforded by coil-by-coil and/or time-period-by-time-period control. The case of simple sums of transmit coils may be treated as a special case of time-independent RF optimization, in which all the coil weights α_l are forced to unity, placing any desired homogeneity adjustment entirely in the domain of the gradient-based common excitation h_n. Modifying Eq. (3.30), the resulting SAR may be expressed in terms of h_n and the precomputed matrix elements $\Phi_{l',l}$:

$$\xi^{\text{sum}} = \frac{1}{N}\left(\sum_{n=1}^{N}|h_n|^2\right)\sum_{l,l'=1}^{L}\Phi_{l',l} \tag{3.40}$$

We used two distinct choices of h_n in our comparisons:

the "forced homogeneity" choice in which h_n is designed to compensate for any inhomogeneities in the net transmit field to yield the exact target excitation μ_n. In this case, setting $\hat{b}_{ln} = \mathcal{B}_x^{\text{coil}}(x_n, y_n) + i\mathcal{B}_y^{\text{coil}}(x_n, y_n)$ for each coil in turn, we have from Eq. (3.32):

$$h_n = \frac{\mu_n}{\sum_{l=1}^{L} \hat{b}_{ln}} \tag{3.41}$$

the simple "sum of coils" choice in which no shaping of the target excitation is performed, and the target profile is allowed to match the simple sum of coil transmit fields: $\mu_n \propto \sum_{l=1}^{L} \hat{b}_{ln}$. In this case, which may be accomplished using a single slice-selective 1D pulse, we need only specify a single proportionality constant which defines the overall "magnitude" of the excitation. For our comparisons, we chose to define a "unit" excitation to occur when the net excitation field equals the mean of its absolute value across the FOV, i.e.

$$h_n = h = \frac{1}{N} \sum_{n=1}^{N} \left| \sum_{l=1}^{L} \hat{b}_{ln} \right| \tag{3.42}$$

Results

Figure 3-3 shows how rapidly the ultimate global SAR approaches a limiting value as the order of the multipole expansion l_{max}, and therefore the number $2*(l_{max} + 1)^2$ of spherical harmonics in the basis set, is increased.

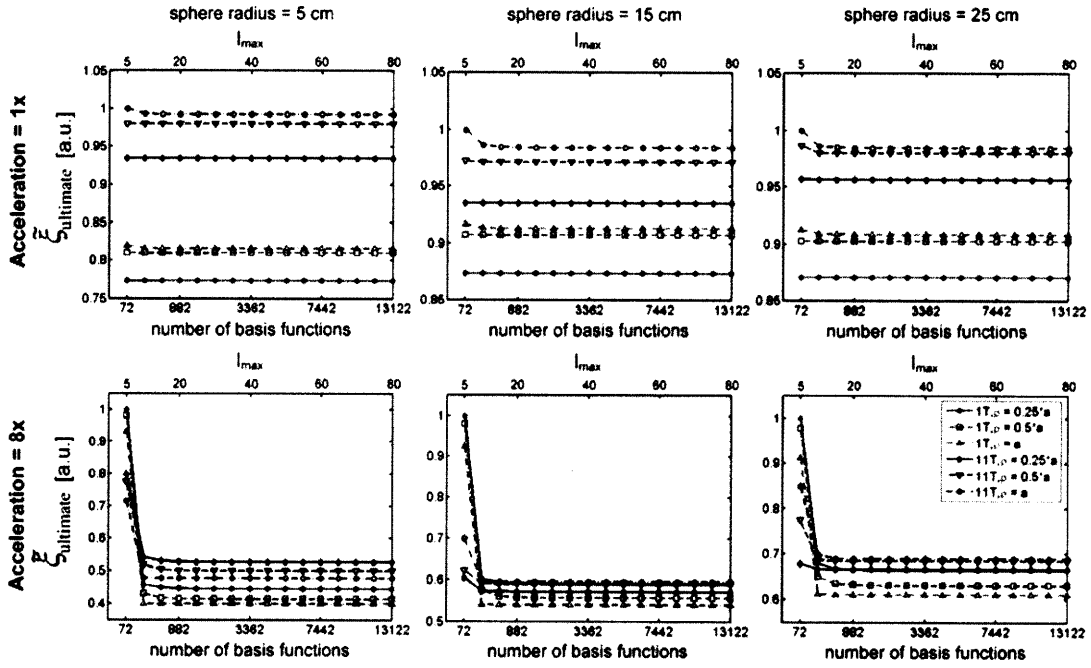

Figure 3-3. Convergence of the ultimate SAR optimization as a function of the number of basis functions used in the calculations. The number of basis functions is equal to $2*(l_{max} + 1)^2$, where l_{max} is the order of the multipole expansion, whose range is reported at the top of each plot. Data are reported for three different sphere radii (a = 5 cm, a = 15 cm, a = 25 cm) and two extreme field strengths (B_o = 1T, B_o = 11T). In each of these cases convergence was tested for the three shapes of the target excitation profile shown in Figure 3-1.

Data are plotted for the cases of the two extreme main magnetic field strengths (1T and 11T), for unaccelerated and 8-fold accelerated parallel excitation. For each of these cases sphere radii of 5 cm, 15 cm, and 25 cm were used, and convergence was tested for the different shapes of the target excitation profile shown in Figure 3-1. The FOV was always a transverse slice through the center of the sphere, as shown in Figure 3-1, with 32-by-32 matrix size. The calculations converged quickly in all cases (Figure 3-3), and for all simulations in this work it was decided to set the expansion order to l_{max} = 80, to match the conditions of a previous investigation using the same multipole expansion (42). Calculations of ultimate SAR in the case of RF shimming have a similar convergence behavior, which is not shown here. The same expansion order used to generate the basis set was employed to calculate the EM field associated with a circular surface coil with the semi-analytical multipole expansion (see Eq. (3.38)).

With our choice of l_{max}, the duration of ultimate global SAR calculations was about 2 minutes for RF shimming and about 5 minutes for unaccelerated fully parallel transmission. Calculation of ultimate intrinsic local SAR is nearly independent of the chosen expansion order and in each case lasted about 90 minutes, as it required performing 2D Fourier transformation on a 32-by-32 matrix of complex elements for every time period of the excitation.

Figure 3-4 compares B_1 homogeneity for different excitation techniques and various coil configurations at 7T main magnetic field strength. A target excitation profile fully homogeneous over the entire FOV was used (i.e. $\mu_n = h_n = 1$ everywhere within the sphere). The leftmost column of Figure 3-4 shows schematic representations of the different transmit coil arrangements around the surface of the sphere. The ultimate intrinsic case at the bottom of the figure is represented as a spherical surface without particular coils in place. The columns to the right of the leftmost column show actual excited profile for the following cases: sum of coils (second column from left, case (b) and Eq. (3.42) in Materials & Methods), forced homogeneity (third column from left, case (a) and Eq (3.41) in Materials & Methods), RF shimming (fourth column from left), and fully parallel transmission (rightmost column).

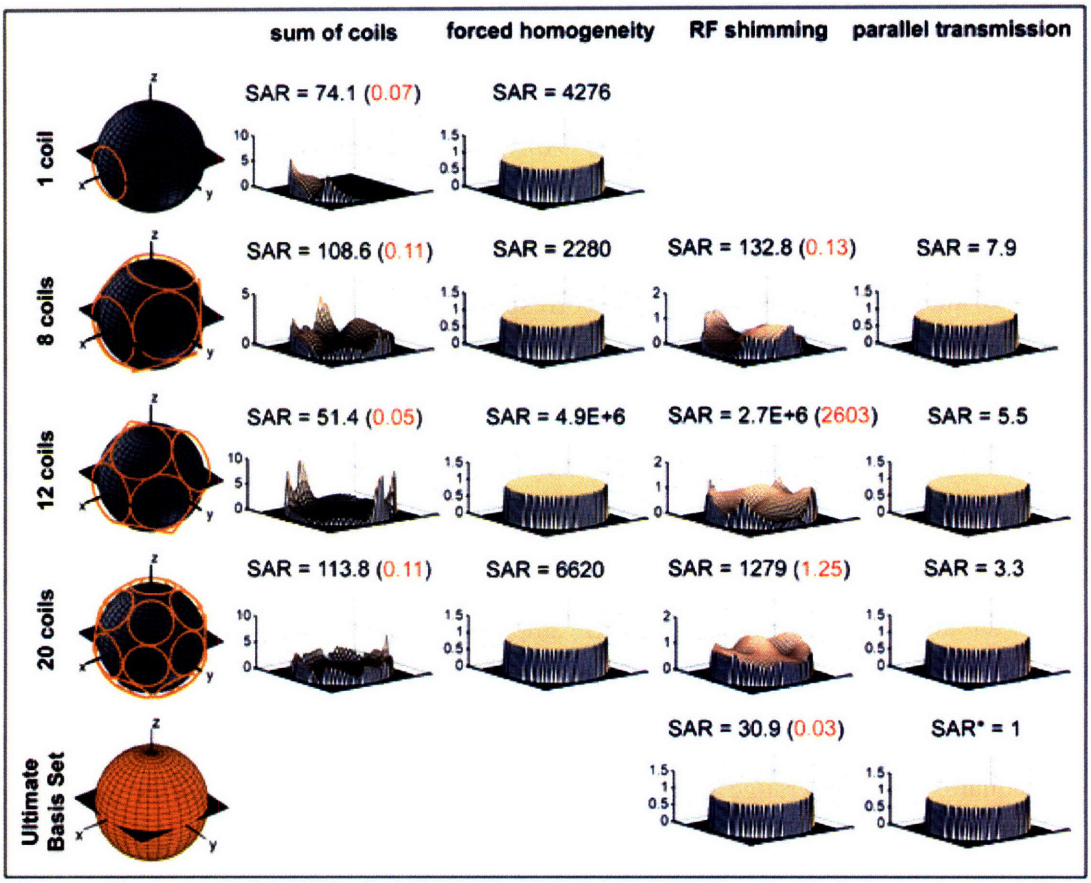

Figure 3-4. Actual excited profile for various transmit coil configurations and different excitation strategies at 7T magnetic field strength. Leftmost column: coil configuration (with ultimate intrinsic case at bottom). Second column from left ("sum of coils"): excitation profile for simple fixed sums of transmit coil fields. The contributions of the individual coils are summed and scaled by the average of the absolute value of each coil's transmit sensitivity (see Eq. 42). Third column from left ("forced homogeneity"): excitation profile for the case in which a common tailored gradient and RF excitation are used to correct for sensitivity variations resulting from the simple sum (see Eq. 41). Fourth column from left and rightmost column: these last two columns refer to RF shimming and parallel transmission respectively, showing that the latter enables homogeneous excitations even with a small number of coils. The radius of the modeled homogeneous sphere is 15 cm. The quantities reported are relative measures of SAR and are normalized to the ultimate intrinsic value for parallel transmission (indicated with an asterisk). The SAR values in parentheses for the second and fourth columns represent the case in which excitation is achieved by repeatedly sampling the center of excitation *k*-space 1024 times with small RF amplitudes, rather than by applying a single high-amplitude spoke in the center during the 32-by-32 EPI trajectory.

We see that fully parallel excitations result in good homogeneity even with small numbers of elements, whereas using RF shimming it is more difficult to correct inhomogeneities in the excitation profile with limited numbers of coils. Even 20 coils are not sufficient for full homogeneity under the conditions studied in Figure 3-4. The value of SAR (normalized to the ultimate intrinsic value for unaccelerated parallel transmission) is plotted above the corresponding actual excited profile.. Two values of SAR are reported in the case of sum of coils and RF shimming. The value on the left corresponds directly to our theoretical formulation, where, for these two excitation strategies, the 32-by-32 EPI trajectory reduces to a single period (or spoke) at the center of k-space, occupying a fraction of the duration of a full 2D tailored excitation. The same result, however, could be also achieved by repeatedly sampling the center of excitation k-space with smaller RF amplitudes. Prolonging the pulse in this way is known to reduce global SAR by the ratio of pulse durations (since the electric field amplitude decreases linearly with the RF current amplitude, and the SAR scales as its square, while the range of temporal integration increases in inverse proportion to the current amplitude in order to preserve flip angle). On the right (red values in parentheses) we report the SAR which would result if the single spoke were repeated/extended 1024 times at correspondingly lower amplitude. Although stretching single-spoke pulses out to durations typical of full 2D selective excitations may not be fully realistic, due to off-resonance effects and other practical considerations, we include this number as a lower bound, with the actual value for particular implementations expected to fall somewhere between the two extremes. The 'forced homogeneity' case clearly shows that a high price in SAR must be paid in exchange for homogeneity of the excitation using fixed multicoil excitation and relying solely upon a common tailored RF and gradient waveform for homogeneity correction. By comparison, SAR values are markedly reduced for fully parallel excitations, and SAR decreases monotonically as the number of transmit elements increases.

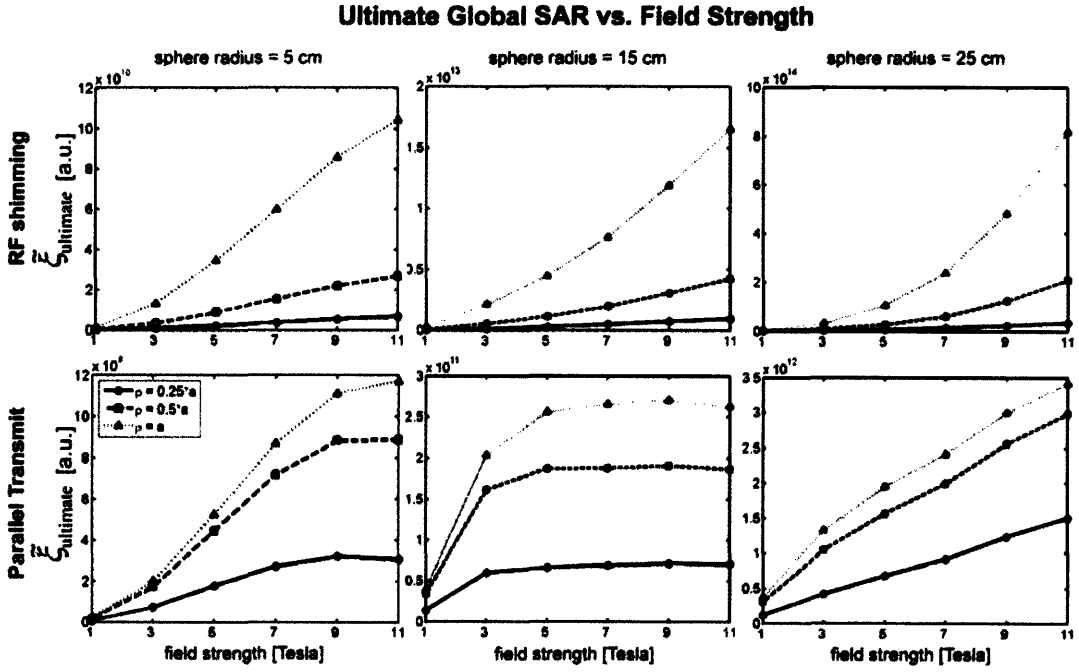

Figure 3-5. Ultimate intrinsic average global SAR for excitation of a transverse FOV through the center of a homogeneous sphere as a function of main magnetic field strength, for SAR-optimized RF shimming (top row) and fully parallel transmission (bottom row). Frequency-dependent average *in vivo* values of sphere electrical properties were used (see Table 1). The size of the modeled sphere increases from the leftmost to the rightmost column. Results are shown for three different concentric homogeneous target excitation profiles, whose radius is indicated in the legend as a fraction of the sphere radius *a*.

The theoretical lower bound on RF power deposition was calculated for different sizes of the sample and for different shapes (see Figure 3-1) of the target excitation profile. The resulting values are plotted in Figure 3-5 as a function of the main magnetic field strength, for the cases of RF shimming and parallel transmission. As expected, both techniques result in higher RF power deposition when the sample dimensions are increased, because more energy is needed to excite positions close to the center of the sphere. Ultimate SAR increases with increasing size of the region in which we wish to excite a fully homogenous profile (assuming that the unexcited regions are controlled in the case of RF shimming by the common excitation profile rather than by the RF shimming process per se, i.e. $\mu_n = h_n = 1$ within excited regions and 0 within unexcited regions). In general, the growth of ultimate SAR with field strength is slower for fully

parallel transmission than for RF shimming. In the case of parallel transmission with a sphere radius of 15 cm, there is an evident flattening in the growth of SAR with field strength. In fact, for a 15cm sphere, ultimate SAR for parallel transmission decreases slightly when field strength is increased from 9T to 11T.

The simple concentric target excitation profiles used to calculate RF power deposition (see Figure 3-1) have sharp edges, and they might seem an unfair and/or unrealistic choice in the case of finite coil arrays. Figure 3-6a shows global SAR and actual excited profile for RF shimming comparing different target excitation profiles: the uniform profile with sharp edges shown in Figure 3-1, a bi-dimensional Gaussian curve of amplitude one in the center of the FOV and a bi-dimensional quadratic function with amplitude decreasing from one at the edges to zero in the center. In all cases $h_n = 1$ over the entire FOV, so that the coils' sensitivities alone were used to shape the excitation profile, without aid from the gradients. For easiest comparison, SAR values are normalized to the lowest value, which corresponds to the ultimate intrinsic case using the smooth profile with low intensity in the center. We notice that there is an evident baseline SAR advantage to using smooth profiles. The actual excited profile matches the target profile only in the case of the ultimate basis set.

In order to improve SAR performance, one might also conceive of relaxing the strict constraint of least-squares adherence to the target excitation profile, since in many applications one might well be willing to settle for an approximate match to the target in exchange for improved SAR. This may be accomplished by introducing some degree of regularization into the pseudoinverse of Eq. (3.34). Figure 3-6b shows that when the tolerance of SVD-based inversion (i.e. the smallest singular value considered non-zero) is increased, the resulting global SAR for RF shimming (normalized to the same case as in Figure 3-6a) becomes smaller, while the shape of the actual excited profile deviates more and more from the desired profile.

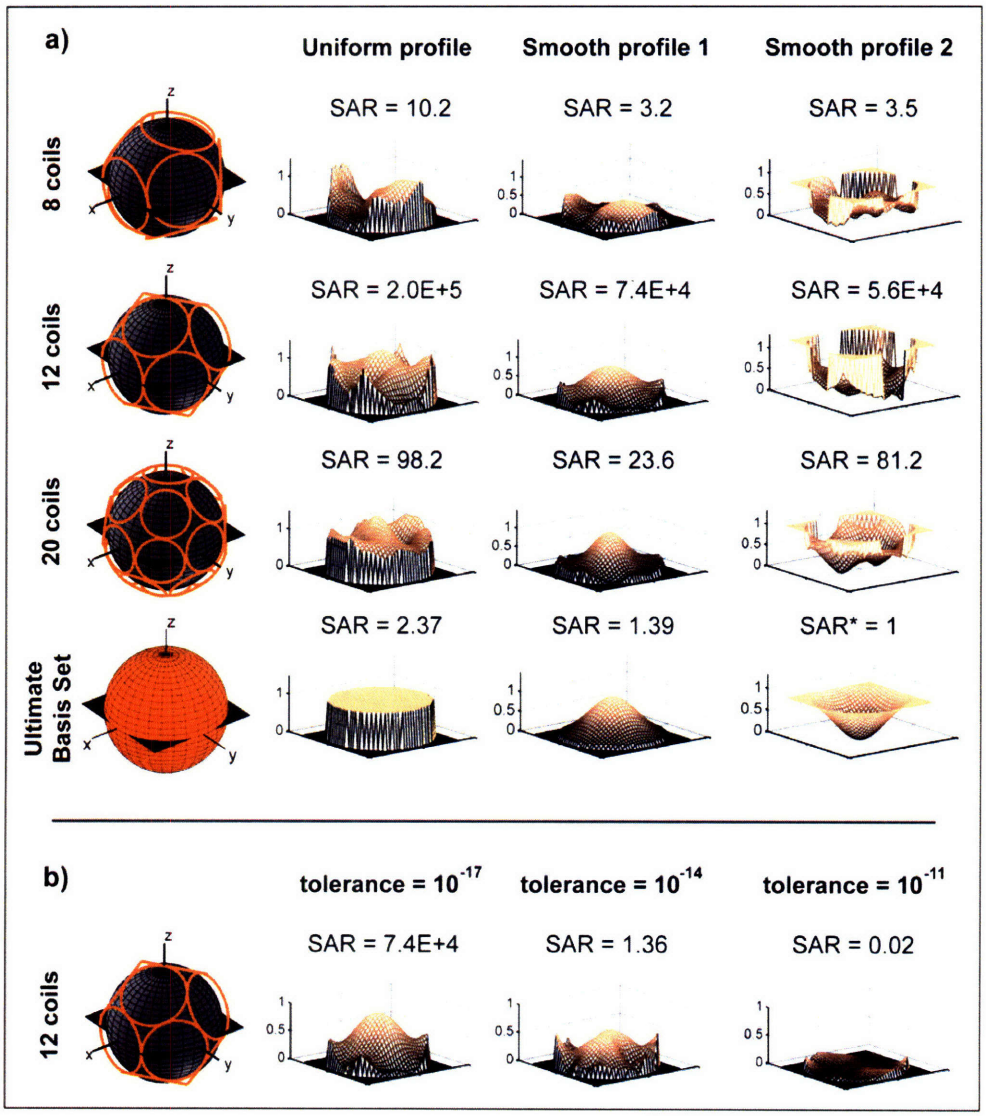

Figure 3-6. SAR benefits of relaxing homogeneity constraints. a) Average global SAR and actual excited profile using RF shimming for various transmit coils configurations at 7T magnetic field strength. The case of uniform concentric profiles considered elsewhere in this work is compared against two smoother target excitation profiles: a bi-dimensional Gaussian curve of amplitude one in the center of the FOV and a bi-dimensional quadratic function with amplitude decreasing from one at the edges to zero in the center. b) Average global SAR and actual excited profile using RF shimming for varying degrees of regularization with a 12-element transmit array at 7T. By increasing the tolerance of the SVD-based inversion in Eq. 23, we can loosen the constraint on profile fidelity in order to improve SAR. SVD tolerance (i.e. the threshold for the smallest singular value considered nonzero and included in the inversion) increases from 10^{-17} to 10^{-14} to 10^{-11} from left to right, and the resulting SAR values for RF shimming are shown above the resulting excited profiles. The radius of the modeled homogeneous sphere is 15 cm for both (a) and (b). The quantities reported are relative measures of SAR and are normalized to the case with the lowest SAR value in (a), which is indicated with an asterisk in the figure.

Dependency of $\tilde{\xi}_{\text{ultimate}}$ upon acceleration factor is plotted in Figure 3-7 for parallel excitations at various magnetic field strengths and for different sample sizes, in the case of a homogenous target excitation profile uniform throughout the FOV (leftmost diagram in Figure 3-1). Ultimate SAR is generally higher for larger accelerations, although the pattern of growth depends on the size of the sample. The smaller the sphere, the more the SAR growth flattens with increasing acceleration.

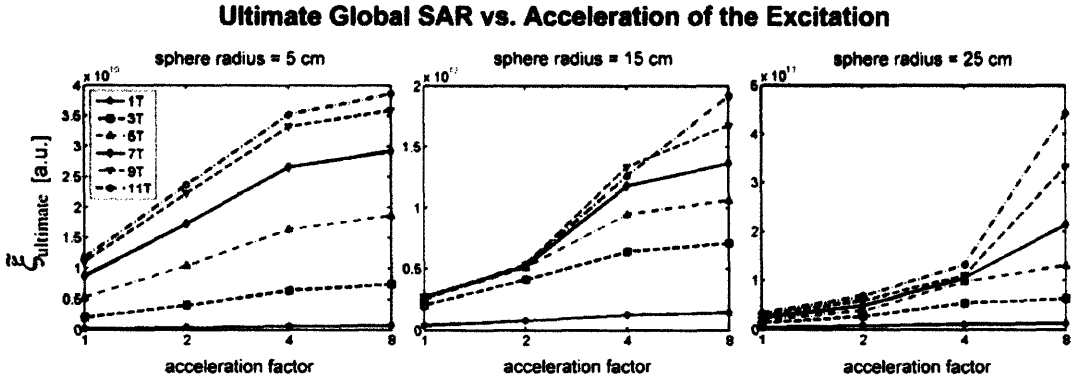

Figure 3-7. Ultimate intrinsic average global SAR for parallel excitations along a transverse FOV through the center of a homogeneous sphere, as a function of the acceleration factor. Each plot refers to a different size of the modeled sphere and shows the behavior for different values of the main magnetic field strength. A uniform, fully homogeneous concentric excitation profile with radius equal to the radius of the sphere was used in all cases.

In addition to global SAR measures, ultimate intrinsic local SAR resulting from unaccelerated parallel excitation with coefficients optimized for global SAR was also calculated using Eq. (3.36) as a function of time, for a uniform concentric target excitation profile with radius equal to the radius of the sphere (leftmost diagram in Figure 3-1). Figure 3-8 shows the computed local SAR distribution within the FOV during excitation of the center of *k*-space (i.e. half way through the duration of the pulse) for different values of the main magnetic field and different sizes of the sample. SAR values are normalized to the lowest local SAR in the plot at the top left of the figure (i.e. B_0 = 1T, sphere radius = 5cm) and are plotted on a logarithmic scale in order to highlight the behavior in the center of the FOV, where SAR is in general much

lower than near the edges. The lower and upper bounds of the colormap were allowed to vary from row to row so that the spatial variation of local SAR could best be appreciated while preserving information about the overall scaling of SAR with field strength. As expected, the spatial distribution of the RF power deposition is affected by the dimension of the sample. In Figure 3-8 it is possible to appreciate how similar ratios between the wavelength of the incident RF field and the radius of the sphere result in similar distribution patterns, as for example in the case of B_0 = 11T and sphere radius equal to 15 cm, as compared with B_0 = 7T and sphere radius equal to 25 cm.

Ultimate intrinsic local SAR as a function of acceleration is shown in Figure 3-9, for a 15 cm sphere at different values of the main magnetic field strength. In order to compare the results, in each case we considered a time period in the middle of the excitation, whose duration differed depending upon the degree of acceleration. The same normalization as in Figure 3-8 was used. For increasing acceleration, an increasing proportion of RF energy is deposited near the center of the FOV, especially at lower field strengths.

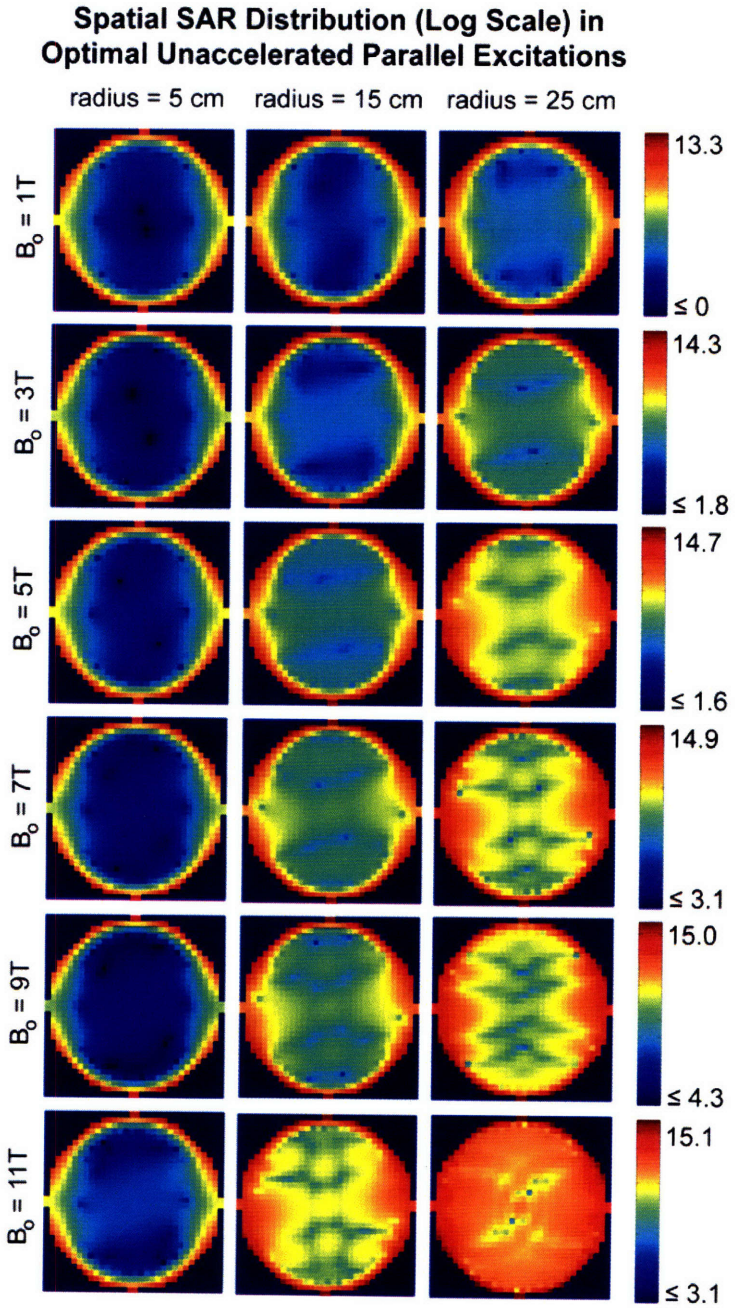

Figure 3-8. Normalized distribution (base-10 Log scale) of local SAR within the FOV during unaccelerated parallel excitations with current patterns optimized for global SAR. For each value of the main magnetic field strength, spatial distribution of ultimate intrinsic local SAR is compared for different sizes of the modeled sphere during excitation of the center of *k*-space.

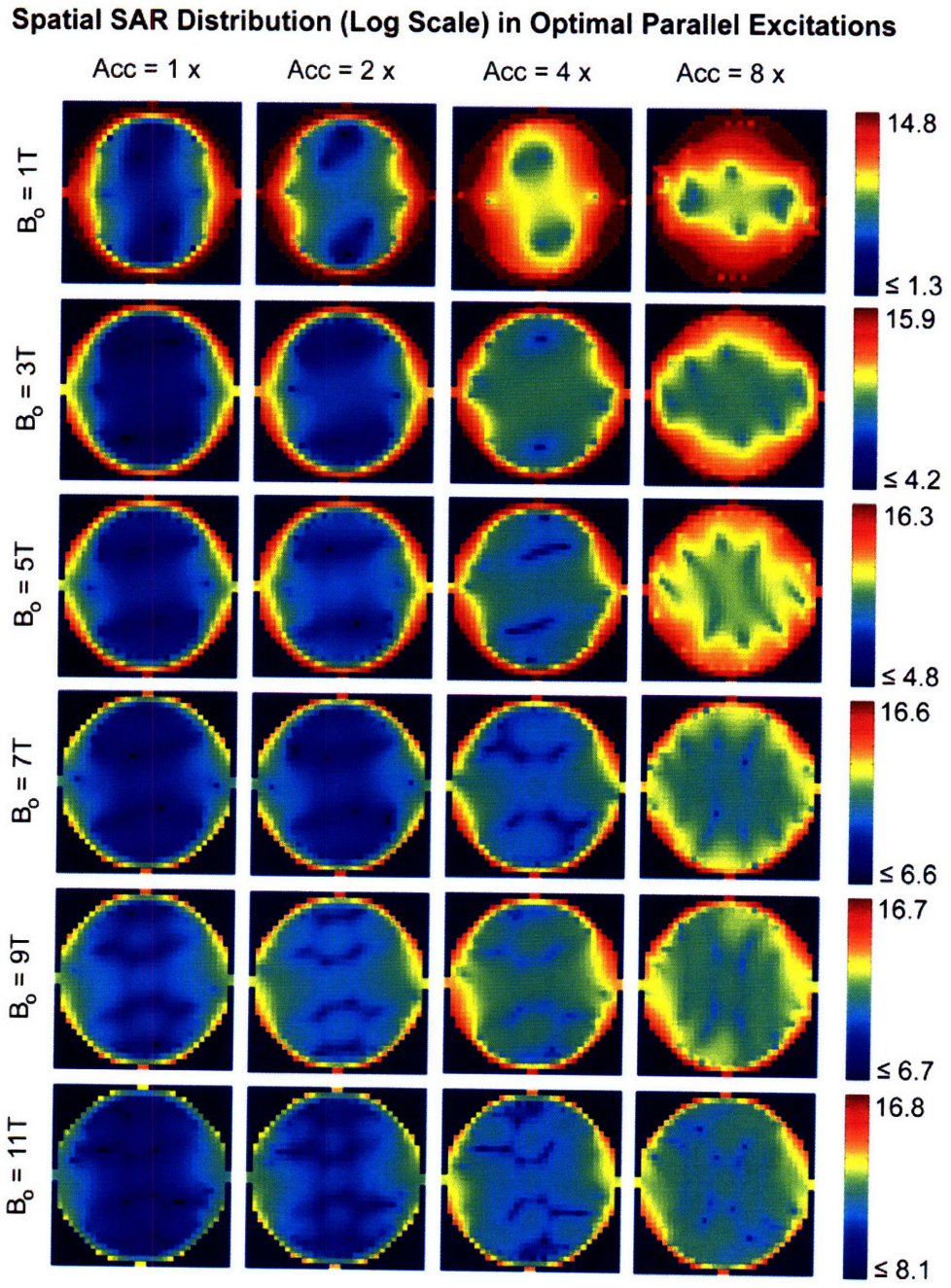

Figure 3-9. Normalized distribution (base-10 Log scale) of local SAR within the FOV during accelerated parallel excitations with current patterns optimized for global SAR in a 15 cm sphere. For each value of the main magnetic field strength, spatial distribution of ultimate intrinsic local SAR during excitation of the center of *k*-space is compared for various acceleration factors.

Figure 3-3 showed that in some cases optimal SAR calculations converge with a relatively small number of basis functions. In Figure 3-10, the ratio of global SAR for finite transmit arrays to ultimate intrinsic SAR is plotted (on a logarithmic scale) in the case of unaccelerated parallel transmission to see how rapidly it is possible to approach ultimate behavior by increasing the number of coils packed around the surface of the sphere. For all magnetic field strengths global SAR can be maintained within one order of magnitude of the theoretical lower bound using transmit arrays with at least 12 coils. Actual SAR approaches the ultimate intrinsic limit faster for smaller values of B_0. At 3T the SAR resulting from parallel excitation with a 8-element array is already only about three times larger than the corresponding ultimate intrinsic SAR.

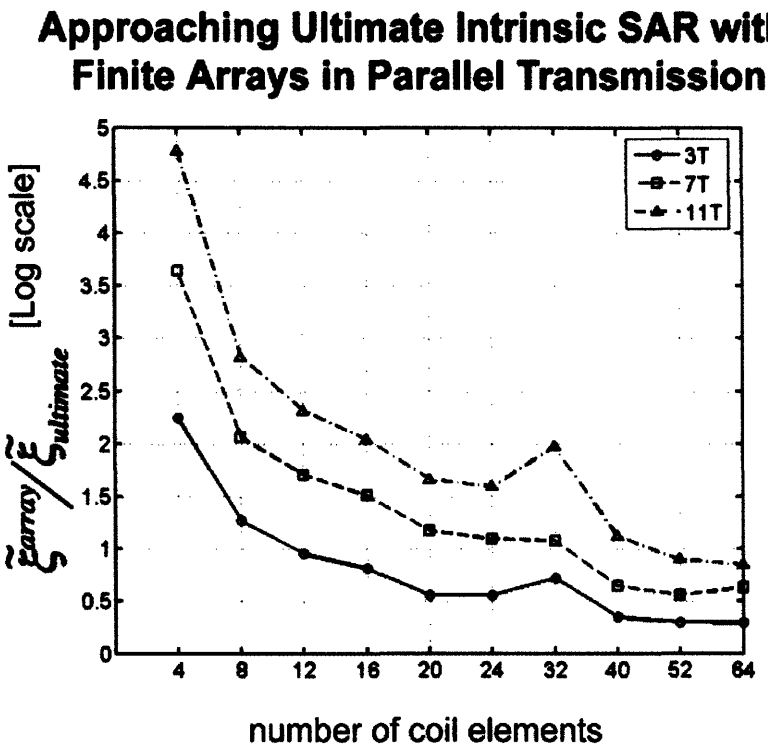

Figure 3-10. SAR efficiency of parallel transmission as a function of the number of coil elements in the transmit array. The ratio of SAR resulting from unaccelerated parallel excitations with finite arrays to ultimate intrinsic SAR is plotted for different magnetic field strengths in the case of a 15 cm sphere, using a logarithmic scale.

Discussion

The aim of this work is to explore electrodynamic constraints on transmit homogeneity and SAR, two of the key obstacles to clinical applications of ultra high field MR imaging. An algorithm is described here to calculate the theoretical lowest possible RF power deposition for a spherical sample, based on multipole expansion of the electromagnetic fields inside the object. Ultimate intrinsic SAR for multi-coil excitations using fully parallel transmission and time-independent RF shimming was assessed at different magnetic field strengths for various object sizes and target excitation profiles.

In RF shimming, optimization of the magnitudes and phases of the driving currents is performed over the entire FOV once for the whole pulse, whereas fully parallel transmission allows engineering of destructive and constructive interferences both in space and in time to achieve uniform profiles and reduce SAR. Ultimate SAR for RF shimming was found to grow almost quadratically with increasing B_0, in large part due to the increasingly stringent demands of homogeneity correction at high field strength. By contrast, for fully parallel transmission the growth of ultimate SAR with field strength flattened out and even slightly decreased for selected object sizes (Figure 3-5). This somewhat surprising behavior, although in contradiction to the commonly assumed quadratic dependency of SAR on frequency, is nevertheless consistent with electrodynamic principles. Previously published computational results for single-port (99,101) and multi-port (102) excitations in particular coil models already have shown a less-than-quadratic SAR increase at high frequencies and empirical evidence can be found in a paper comparing head images at 4T and 7T (103). Ibrahim and Tang (102) used a rigorous FDTD model to investigate dependence of RF power deposition on frequency in the case of a particular 4-, 8- and 16-port TEM resonator and found results similar to those plotted for ultimate intrinsic SAR in our Figure 3-5, in which SAR peaks in the vicinity of 7 Tesla and then decreases at higher field strength. Two general physical arguments may be adduced to explain the observed behavior of ultimate intrinsic SAR. First, SAR behavior is governed by the relative scaling between the electric field and the magnetic field, since the electric field is directly

responsible for energy deposition via the sample conductivity, while the magnetic field controls the degree of spin excitation. In other words, the quantity of interest is the SAR per unit flip angle, or $\iint_{V\,\Delta t} \sigma(\mathbf{r})\left|\mathcal{E}(\mathbf{r}, p\Delta t)\right|^2 dtdv \Big/ \left|\tilde{\mathcal{B}}_1^+\right|$. Ignoring for the moment the subtleties involved in the spatiotemporal integration and the implicit sum over modes, we see that the relevant quantity for each multipole mode in the expansion of Eq.'s (3.37) and (3.38) is $\sigma|\mathbf{e}_l|^2/|\mathbf{b}_l| \sim \sigma|\mu\omega/k|^2$. This overall scaling factor is plotted in Figure 3-11, and it shows a flattening with increasing frequency which clearly contributes to the observed ultimate intrinsic SAR behavior. At high frequencies, the possibility of increased destructive interference of electric fields (101) could also contribute to the sub-quadratic increase of SAR with frequency.

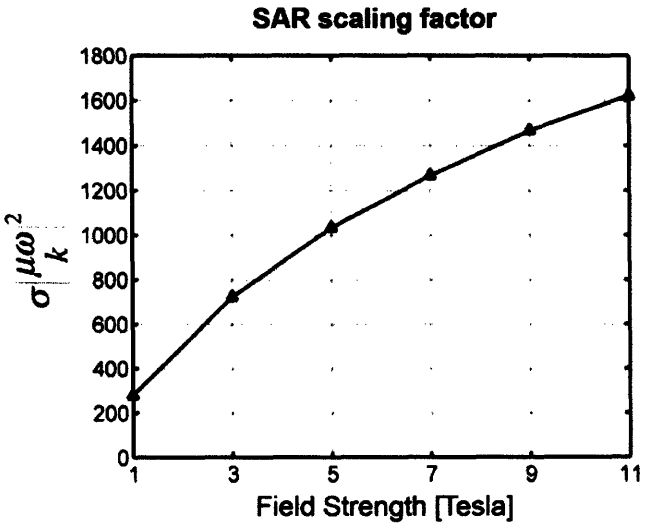

Figure 3-11. Behavior, as a function of main magnetic field strength, of the scaling factor that pre-multiplies the SAR per unit flip angle for both the case of circular surface coils and the limit case of a full basis set of spherical harmonics. Permeability of free space was used, whereas conductivity and permittivity were set to frequency-dependent *in vivo* values as in Ref. (42).

In fully parallel transmission for moderately-sized spheres, the flattening is even more accentuated because at high frequencies the wavelength is sufficiently reduced (Figure

3-12) to become compatible with spatial focusing, allowing for further reduction of RF power deposition via engineered field cancellations. For large spheres, the modest skin depth at high frequency (Figure 3-12) prevents effective field penetration into central regions, thereby spoiling some of the effectiveness of engineered cancellation.

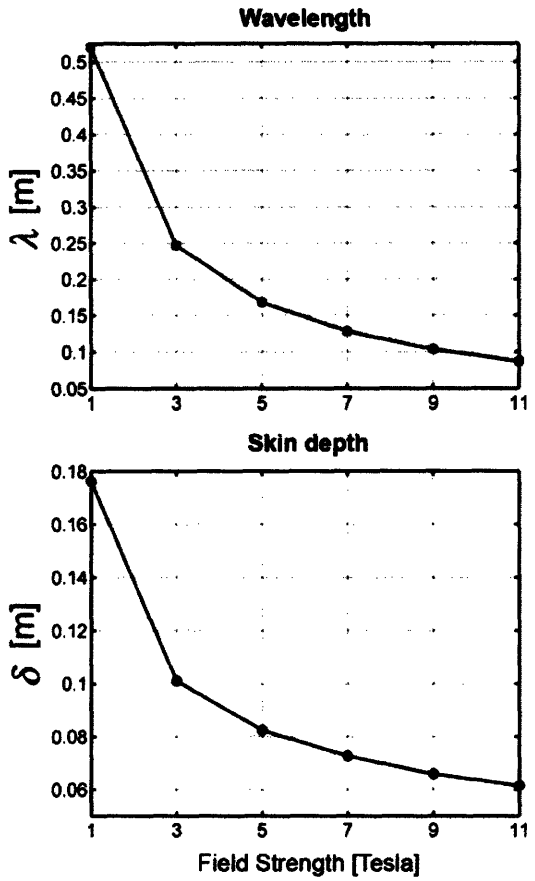

Figure 3-12. Wavelength and skin depth as a function of main magnetic field strength. The electrical properties were set to frequency-dependent *in vivo* values as for Figure 3-11.

When the length of a pulse is shortened, SAR is expected to grow, as transmit currents must be increased to achieve any target level of excitation, and these currents enter quadratically into the expression for SAR. However, in the case of accelerated parallel excitations, ultimate SAR increased only moderately for small acceleration factors, and

overall was found to grow more slowly than expected (Figure 3-7). Relaxation of the constraint on homogeneity of each component coil's excitation profile in the framework of an accelerated excitation may be in part responsible for this behavior, which nevertheless bears further investigation.

Ultimate intrinsic average global SAR is a global measure of the lowest achievable SAR over the entire pulse duration and the entire volume of the object. Spatial distribution of SAR is, however, very important for *in-vivo* applications, as "hotspots" may occur in vulnerable anatomic locations (e.g. the orbits for brain imaging studies). Once the current patterns that result in SAR-optimal parallel excitations are calculated, they can be used to compute the associated local RF power deposition at each spatial position and each time period in the excitation. Our results show that, as might be expected, the spatial distribution of SAR within the object depends on its size, since the pattern of interaction of RF fields with dielectric material is dictated by the relation between the incident wavelength and the object dimensions (Figure 3-8). As acceleration factor increases for parallel excitation, optimum local SAR values near the center of the object become more comparable to the values at its edges (Figure 3-9), showing that undersampling leads to more RF energy deposition in the middle of the sample. This behavior is less dominant at higher field strengths, suggesting that parallel transmission becomes more effective in resolving aliased positions at higher frequencies. These trends aside, however, peak local SAR is always larger at positions near the surface of the sphere, where the electric field is larger. A quantitative interpretation of peak SAR results for practical safety purposes is delicate and is left to future work.

Both RF shimming and parallel transmission enable complete compensation of B_1 inhomogeneities over a 2D FOV in the ultimate intrinsic case. Even with few coils in fixed combinations, transmit field homogeneity can always be corrected by relying upon a shared gradient- and RF-based excitation pattern to undo the spatial variation of coil sensitivities, although the associated SAR price can be very high (Figure 3-4). When a transmit array is available, RF shimming can be used to improve homogeneity, while controlling RF power deposition. However, many transmit coils may be needed

in order to excite the desired profile. On the other hand, parallel transmission yields good compensation of B_1 inhomogeneities even with small arrays, suggesting once again the potential benefits of this technique at ultra high field strengths. Relative RF shimming performance is improved by choosing appropriately smooth target excitation profiles.

In addition to the shape of the target profile itself, the requirements for profile fidelity have a strong effect on the tradeoff between SAR and homogeneity in multicoil excitation pulse design. The algebraic optimization algorithm employed in this work treats adherence to the target profile as the primary constraint, and minimizes global SAR subject to this constraint. This explains the substantially lower global SAR for RF shimming with an 8-element transmit array (see Figure 3-4 and 3-6) as compared with a 12- or 20-element array. In fact, with only 8 coils, close adherence to the target profile is impossible, and remaining degrees of freedom are used for SAR reduction. With more coils, combinations representing a closer match to the target are possible, but these combinations are costly in SAR. Of course, in practice homogeneity need not be prioritized universally over SAR in this manner. A flexible tradeoff between the two pulse design goals is possible using appropriate regularization strategies. The results shown in Figure 3-6a indicate that the SAR performance of RF shimming approaches may be improved dramatically with regularization. SAR for fully parallel excitations is correspondingly reduced if a similar flexibility in excitation profile is allowed.

SAR results will of course depend as well upon the underlying excitation trajectory, but the general trends demonstrated in this work are expected to be consistent among trajectories. EPI trajectories were used here since they permit a particularly simple formulation of the transmit acceleration process (59), but other excitation trajectories and pulse design approaches are possible (58,104), with some increase in numerical complexity.

One limitation of this study is that in our choice of a uniform target excitation profile ($\mu = 1$) we are constraining both the magnitude and the phase of the optimized B_1 field within the FOV. Although this approach allows us to maintain the linearity of the

algorithm and to apply the same SAR optimization to different multi-coil excitation techniques, it is important to remember that, for RF shimming to be effective in certain applications, only the magnitude of B_1 (and of the resulting transverse magnetization) may need to be constrained. Specifying the phase as well in these cases might be unnecessarily restrictive. Indeed, it has been shown that the performance of parallel transmission and multi-spoke pulses can be improved with excitation designs that compensate for B_1 magnitude inhomogeneities, allowing for a small amount of spatial phase variation (105).

Another limitation is the use of a single geometry, but the general theoretical framework outlined in the Theory section applies to any geometry and, for example, it can be extended in a straightforward manner to a cylindrical object by using a different set of basis functions. Furthermore, in this investigation we assumed the spherical sample to be homogeneous, but the general principles should hold for more complex models, incorporating multiple *in-vivo* tissue types.

It will be important in future work to investigate how sensitive the optimal combination of the individual coils' excitation patterns may be with respect to calibration errors or small loading perturbations. A better understanding of these questions will help in assessing the practical feasibility of approaching ultimate intrinsic SAR with a relatively small number of transmit elements. In any case, ultimate intrinsic SAR is a theoretical lower bound independent from any specific coil geometry and it can be used as a reference performance target for future designs.

One other practical detail we chose not to include in our circular coil model is the potential effect of inductive or other coupling between transmit coils. This matter has been discussed extensively in the context of early implementations of parallel transmission. However, it is possible that appropriate incorporation of the measured correlation matrix $\mathbf{\Phi}$ into the SAR optimization will substantially blunt the worst effects of coupling, just as incorporation of the noise correlation matrix in parallel image reconstructions has been shown to blunt the effects of coupling upon SNR (106).

Finally, we chose to assess homogeneity (or adherence to a particular target excitation) in a single 2D FOV. Correcting homogeneity over an entire volume is a more ambitious proposition, and it may even be impossible for RF shimming alone (55). Full volumetric homogeneity correction remains possible with fully parallel transmission, but relatively long pulse durations may be required to add a sufficient number of degrees of freedom to the optimization problem.

Conclusions

In the present work, fundamental constraints on the lowest possible SAR obtainable with multi-coil excitations were studied with respect to the underlying electrodynamics. In parallel transmission, the capability to transmit tailored excitations with the individual elements of a transmit array enables a high degree of control over B_1 homogeneity in combination with an effective means of SAR management. In RF shimming, relatively low SAR values can be achieved with comparatively simple pulses, but the tradeoff between homogeneity and SAR is less robust. In the case of parallel transmission, ultimate intrinsic SAR varies quite slowly with frequency at the highest field strengths studied, suggesting dramatic potential benefits of this technique for high field imaging and spectroscopy.

Acknowledgements

The authors are grateful to Florian Wiesinger for helpful discussions about the semi-analytical multipole expansion of circular coil fields, and for providing code to distribute closely packed coils around a sphere. Funding support from NIH grant R01 EB005307, R01 EB000447 and R01 EB002468 are also gratefully acknowledged.

Appendix A

Minimization of average SAR in RF shimming and parallel transmission

In the Theory section we showed that the problem of finding the set of complex modulation coefficients that minimize ξ while exciting the target profile (see Eq. (3.31)) reduces to the minimization of the function

$$\xi = \frac{1}{N}\left(\sum_{\rho=1}^{N}\left|h_\rho\right|^2\right)\left(\boldsymbol{\alpha}^H \boldsymbol{\Phi}\, \boldsymbol{\alpha}\right), \tag{3.A1}$$

by varying the quantity $\boldsymbol{\alpha}$, under the constraint:

$$\mathbf{S}_{FOV}\boldsymbol{\alpha} = \frac{\boldsymbol{\mu}_{FOV}}{\mathbf{h}_{FOV}}, \tag{3.A2}$$

where $\boldsymbol{\alpha}$ is a [L x 1] vector, $\mathbf{S}_{FOV}$ a [N x L] matrix, $\boldsymbol{\Phi}$ a [L x L] matrix and $\frac{\boldsymbol{\mu}_{FOV}}{\mathbf{h}_{FOV}}$ a [N x 1] vector. The minimization problem can be expressed as a Lagrange function:

$$\mathcal{L} = \sum_{l=1}^{L}\sum_{l'=1}^{L}(\alpha_{l'}^{*}\,\Phi_{l',l}\,\alpha_l) + \sum_{n=1}^{N}\sum_{l=1}^{L}\lambda_n(S_{n,l}\alpha_l - \frac{\mu_n}{h_n}) + \sum_{n=1}^{N}\sum_{l'=1}^{L}(\alpha_{l'}^{*}S_{n,l'}^{*} - \frac{\mu_n^{*}}{h_n^{*}})\lambda_n^{*}, \tag{3.A3}$$

where λ_n's are Lagrange multipliers and the scaling factor in Eq. (3.A1) has been removed for simplicity. Using a matrix formulation, Eq. (3.A3) becomes:

$$\mathcal{L} = \left(\boldsymbol{\alpha}^H \boldsymbol{\Phi}\, \boldsymbol{\alpha}\right) + \boldsymbol{\lambda}\left(\mathbf{S}_{FOV}\boldsymbol{\alpha} - \frac{\boldsymbol{\mu}_{FOV}}{\mathbf{h}_{FOV}}\right) + \left(\mathbf{S}_{FOV}^{H}\boldsymbol{\alpha}^H - \frac{\boldsymbol{\mu}_{FOV}^{H}}{\mathbf{h}_{FOV}^{H}}\right)\boldsymbol{\lambda}^H. \tag{3.A4}$$

If we set to zero the partial derivatives of $\mathcal{L}$ with respect to $\boldsymbol{\lambda}$, $\boldsymbol{\alpha}$, $\boldsymbol{\alpha}^H$ and $\boldsymbol{\lambda}^H$, we obtain four equations which result in the solution $\tilde{\boldsymbol{\alpha}}$ of Eq. (3.33).

In the Theory section we showed that in the case of parallel transmission we can separately optimize the current patterns for each target position, as the RF power ξ in Eq. (3.19) is positive definite. The minimization problem in Eq (3.19) can thus be divided in N sub-problems, each of which can be solved with the same method outlined in this section for the case of RF shimming.

Appendix B

Calculations of the fields for a coil at an arbitrary position near the surface of the sphere

Eq. (3.38) provides an expression for the EM field produced by a circular coil whose axis coincides with the z-axis of the laboratory frame (Figure 3-2). The same expression can be used to calculate the field for an identical circular coil at a different position near the surface of the sphere, by applying an appropriate rotation. The orientation of the reference frame of the rotated coil with respect to the laboratory frame is defined by the angles α and β in Figure 3-2. So the two reference frames can be superimposed by the consecutive application of two rotations:

$$\mathbf{R}_{\alpha\beta} = \mathbf{R}_z(\alpha)\mathbf{R}_y(\beta) = \begin{pmatrix} \cos(\alpha) & \sin(\alpha) & 0 \\ -\sin(\alpha) & \cos(\alpha) & 0 \\ 0 & 0 & 1 \end{pmatrix} \begin{pmatrix} \cos(\beta) & 0 & -\sin(\beta) \\ 0 & 1 & 0 \\ \sin(\beta) & 0 & \cos(\beta) \end{pmatrix}. \quad (3.B1)$$

Pre-multiplying the EM fields of the rotated coil by the rotation matrix $\mathbf{R}_{\alpha\beta}$, we express them with respect to the laboratory frame. Then, in order to evaluate the EM fields at the same positions for both coils, we need to rotate the plane of the FOV backward to its original position, using the inverse of $\mathbf{R}_{\alpha\beta}$.

The transmit RF field produced by the rotated circular coil can thus be calculated as:

$$\begin{aligned} \mathcal{E}_{\alpha\beta}^{\text{coil}}(\mathbf{r}) &= \mathbf{R}_{\alpha\beta}\mathcal{E}^{\text{coil}}(\mathbf{R}_{\alpha\beta}^{-1}\mathbf{r}) \\ \mathcal{B}_{\alpha\beta}^{\text{coil}}(\mathbf{r}) &= \mathbf{R}_{\alpha\beta}\mathcal{B}^{\text{coil}}(\mathbf{R}_{\alpha\beta}^{-1}\mathbf{r}) \end{aligned}, \quad (3.B2)$$

where $\mathcal{E}^{\text{coil}}$ and $\mathcal{B}^{\text{coil}}$ are the fields of a coil coaxial with the z-axis, defined in Eq. (3.38). The resulting values of $\mathcal{B}_{\alpha\beta}^{\text{coil}}(\mathbf{r})$ were used to generate transmit sensitivities. For computation of the matrix $\mathbf{\Phi}$, the quantity $\int_V \sigma(\mathbf{r})\mathcal{E}_{\alpha\beta}^{\text{coil}}(\mathbf{r})\cdot\mathcal{E}_{\alpha'\beta'}^{\text{coil}*}(\mathbf{r})d^3\mathbf{r}$ for appropriately rotated versions of coil electric fields was generated by numerical integration in a common reference frame, since a compact analytic expression is not available.

Chapter 4

Dyadic Green's Functions for Electrodynamic Calculations of Ideal Current Patterns yielding Optimal SNR and SAR in Magnetic Resonance Imaging

Abstract

Numerical simulation techniques are commonly used to model interactions between human tissues and the electromagnetic fields generated by RF coils in MRI experiments. At high and ultra-high magnetic field strengths modeling of these effects becomes ever more important, as inhomogeneities in the RF reception field may compromise image quality, and as the power deposited into tissue during RF transmission tends to increase. In this work we present a theoretical framework, based on a rigorous electrodynamic formulation using dyadic Green's functions, to derive the electromagnetic field in homogeneous spherical and cylindrical samples. We show how to calculate ideal current patterns, independent on any particular coil design, resulting in ultimate intrinsic SNR, the highest possible SNR, or ultimate intrinsic SAR, the lowest possible RF power deposition for a target flip angle distribution. We simulated optimal SNR and SAR for various coil array configurations and we compared the results with the corresponding theoretical limit. Optimal performance may be approached with finite arrays if ideal current patterns are used as a reference in coil design.

Introduction

Accurate modeling of electromagnetic (EM) effects is becoming increasingly important as higher magnetic field strengths are employed in MR systems. The interactions of the EM field with biological tissues at high frequencies require appropriate coil designs to improve image quality and to avoid adverse effects in patients. Parallel imaging (15-17) and parallel excitation (58,59) techniques are promising solutions to overcome these issues. In reception, the increased signal-to-noise ratio, available at higher field strengths, allows for higher degrees of acceleration in parallel MRI, therefore reducing susceptibility artifacts. In transmission, arrays of independently driven transmit coils allows for time-varying control over the EM field which can be used to improve B_1 homogeneity and to minimize specific absorption rate (SAR). As the number of channels available in MR systems has increased to enable faster acquisitions and multiple coil excitations, building prototypes of coil arrays has become more difficult and expensive, and therefore the design of coil arrays has relied ever more upon electrodynamic simulations.

Numerical simulations with techniques such as the finite difference time domain (FDTD) technique are normally used for EM analyses with detailed heterogeneous models of the human body (88,107,108). Although these approaches are rigorous and the results have shown good agreement with experimental data, they are time-consuming and the numerical complexity grows rapidly as the number of modeled coils increases. The duration of these simulations also restricts the number of different coil-sample configurations that can be realistically explored, limiting the generality of the results. In fact, it has been shown that there is a strong dependency of SNR and SAR upon geometrical and physical factors (42,100,109), such as shape and dimensions of the object and the conductors, or electrical properties of the tissues. As the investigation of these relations is fundamental to gain physical insight into the behavior of RF coils at high magnetic field strength, different electrodynamic approaches can be employed, allowing for less detailed geometrical models and faster, but still rigorous, simulations of the EM field.

In this work we use mode expansions with dyadic Green's functions (DGF) (73) to express the full-wave EM field in a dielectric sphere and in a dielectric cylinder. A similar DGF approach for SNR calculation was described by Schnell et al. in the case of a cylindrical sample (110), but to our knowledge such an approach has not been explored for spherical geometries until now. The model in Ref. (110) was also extended to include the effects of the conductive shield of the MR system. Semi-analytical calculations of SNR and SAR for simulated MR experiments, both for specific coil geometries and for the ultimate intrinsic case, can be performed quickly with our DGF formulation. The theoretical framework also enables derivation of optimized surface current patterns corresponding to the best possible performance. Preliminary results of this work were presented at a recent conference (74,111).

Theory

Electromagnetic field expansion in a dielectric sphere with dyadic Green's functions

The DGF formalism enables calculation of the electric field resulting from any spatial current distribution $\mathbf{J}(\mathbf{r})$ as:

$$\mathbf{E}(\mathbf{r}) = i\omega\mu_0 \iiint_{V'} \bar{\mathbf{G}}(\mathbf{r},\mathbf{r}') \cdot \mathbf{J}(\mathbf{r}') dV', \tag{4.1}$$

where i is the imaginary unit, ω is the angular frequency, μ_0 is the magnetic permeability in free-space and $\bar{\mathbf{G}}(\mathbf{r},\mathbf{r}')$ is the branch of the DGF corresponding to the region indicated by $\mathbf{r}$. The DGF associated with a dielectric sphere immersed in free space was constructed, using the method of scattering superposition (Appendix A), in terms of the following vector wave functions, which are among the possible solutions of the vector wave equation in spherical coordinates:

$$\begin{aligned} \mathbf{M}_{l,m}(\mathbf{r}, k_{\text{in}}) &= -i\sqrt{l(l+1)}\, j_l(k_{\text{in}}\rho)\mathbf{X}_{l,m}(\theta,\varphi) \\ \mathbf{N}_{l,m}(\mathbf{r}, k_{\text{in}}) &= \frac{-i\sqrt{l(l+1)}}{k_{\text{in}}} \nabla \times j_l(k_{\text{in}}\rho)\mathbf{X}_{l,m}(\theta,\varphi) \end{aligned} \tag{4.2}$$

In this expression j_l is a spherical Bessel function of order l, k_{in} is the complex wave number inside the sample:

$$k_{\text{in}}^2 = \omega^2 \varepsilon_r \varepsilon_0 \mu_0 + i\omega\mu_0\sigma \tag{4.3}$$

where ε_0 is the permittivity of free space, ε_r and σ are the relative permittivity and the conductivity of the sphere, respectively. The function $\mathbf{X}_{l,m}$ is a vector spherical harmonic defined as:

$$\mathbf{X}_{l,m}(\vartheta,\phi) = \frac{-i}{\sqrt{l(l+1)}}(\rho\hat{\rho}\times\nabla)\mathrm{Y}_l^m(\vartheta,\phi), \tag{4.4}$$

where Y_l^m is a spherical harmonic.

If we define the current distribution $\mathbf{J}(\mathbf{r})$ to exist only on the sphere surface, Eq. (4.1) reduces to a surface integral. In the most general case, the surface current density may consist of both magnetic-type and electric-type components, indicated with the superscript $^{(\mathrm{M})}$ and $^{(\mathrm{E})}$ respectively, and we can express it with a mode expansion. The generic surface current mode would take the form of:

$$\mathbf{K}_{l,m}(\theta,\varphi) = -i\sqrt{l(l+1)}\left[W_{l,m}^{(M)}\mathbf{X}_{l,m}(\theta,\varphi) + W_{l,m}^{(E)}\rho\hat{\rho}\times\mathbf{X}_{l,m}(\theta,\varphi)\right], \tag{4.5}$$

where $W_{l,m}^{(M)}$ and $W_{l,m}^{(E)}$ are the series expansion coefficients representing divergence-free and curl-free surface current contributions, respectively. Substituting in Eq. (4.1), we find the following expression for the EM field inside the sphere (Appendix B):

$$\begin{aligned}
\mathcal{E}(\mathbf{r}) &= \frac{\omega\mu_0}{k_{\text{in}}}\sum_{l=0}^{+\infty}\sum_{m=-l}^{+l}\left[\tilde{\mathbf{M}}_{l,m}(k_{\text{in}},\mathbf{r})V_{l,m}^M + \tilde{\mathbf{N}}_{l,m}(k_{\text{in}},\mathbf{r})V_{l,m}^N\right] \\
\mathcal{B}(\mathbf{r}) &= i\mu_0\sum_{l=0}^{+\infty}\sum_{m=-l}^{+l}\left[\tilde{\mathbf{N}}_{l,m}(k_{\text{in}},\mathbf{r})V_{l,m}^M + \tilde{\mathbf{M}}_{l,m}(k_{\text{in}},\mathbf{r})V_{l,m}^N\right]
\end{aligned} \tag{4.6}$$

$\tilde{\mathbf{M}}$ and $\tilde{\mathbf{N}}$ are the same functions in Eq. (4.2), divided by $-i\sqrt{l(l+1)}$. The weighting coefficients $V_{l,m}^M$ and $V_{l,m}^N$ are derived multiplying the expansion coefficients of the current density with a transformation matrix $\mathbf{T}$ (see Appendix B) that accounts for boundary conditions at the surface of the sphere:

$$\begin{pmatrix} V_{l,m}^{M} \\ V_{l,m}^{N} \end{pmatrix} = \mathbf{V} = \mathbf{T}^{\mathrm{T}}\mathbf{W} = \mathbf{T}^{\mathrm{T}} \begin{pmatrix} W_{l,m}^{(M)} \\ W_{l,m}^{(E)} \end{pmatrix}, \tag{4.7}$$

where the superscript $^{\mathrm{T}}$ indicates the transpose of the matrix. Note that the vectors **V**, **T** and **W** are defined for given (l, m).

Electromagnetic field expansion in a dielectric cylinder with dyadic Green's functions

For the case of a dielectric cylinder, we have extended the EM field expansion described by Schnell et al. (110) to include the MR conductive shield in the model. A detailed derivation is provided in Appendix B. The generic current mode on the surface of the cylinder would take the form of:

$$\mathbf{K}_n(m,\varphi,z) = W_n^{(M)}(m)\nabla \times e^{in\varphi}e^{imz}\hat{\rho} + W_n^{(E)}(m)\nabla e^{in\varphi}e^{imz}, \tag{4.8}$$

and the vector wave functions used to construct the DGF are:

$$\begin{aligned} \mathbf{M}_{n,\gamma}(m,\mathbf{r}) &= \nabla \times J_n(\gamma\rho)e^{in\varphi}e^{imz}\hat{z} \\ \mathbf{N}_{n,\gamma}(m,\mathbf{r}) &= \frac{1}{k_{\mathrm{in}}}\nabla \times \nabla \times J_n(\gamma\rho)e^{in\varphi}e^{imz}\hat{z}, \end{aligned} \tag{4.9}$$

where $J_n(\gamma\rho)$ is a Bessel function of integer order n and the eigenvalue parameter γ is defined as:

$$\gamma^2 = k_{\mathrm{in}}^2 - m^2 \tag{4.10}$$

with k_{in} as in Eq. (4.3). The expression for the EM field inside the dielectric cylinder is similar to Eq. (4.6) and it was also reported in Ref. (110):

$$\begin{aligned} \mathcal{E}(\mathbf{r}) &= -\frac{\omega\mu_0}{8\pi}\sum_{n=-\infty}^{+\infty}\int_{-\infty}^{+\infty}\left[\tilde{\mathbf{M}}_{n,\gamma}(m,\mathbf{r})V_n^M(m) + \tilde{\mathbf{N}}_{n,\gamma}(m,\mathbf{r})V_n^N(m)\right]dm \\ \mathcal{B}(\mathbf{r}) &= -\frac{ik_{\mathrm{in}}\mu_0}{8\pi}\sum_{n=-\infty}^{+\infty}\int_{-\infty}^{+\infty}\left[\tilde{\mathbf{N}}_{n,\gamma}(m,\mathbf{r})V_n^M(m) + \tilde{\mathbf{M}}_{n,\gamma}(m,\mathbf{r})V_n^N(m)\right]dm \end{aligned} \tag{4.11}$$

For this work, we re-derived the transformation matrix **T** that multiplies the currents weights (see Eq. (4.7)), to account for boundary conditions due to the MR conductive

shield surrounding the cylinder (Appendix B). In order to calculate the current induced in the shield, we also derived an expression for the EM outside the cylinder:

$$\begin{aligned}\mathcal{E}_{\text{out}}(\mathbf{r}) &= -\frac{\omega\mu_0}{8\pi}\sum_{n=-\infty}^{+\infty}\int_{-\infty}^{+\infty}\left[\mathbf{A}_{n,\eta}(m,\mathbf{r})V_n^A(m)+\mathbf{B}_{n,\eta}(m,\mathbf{r})V_n^B(m)\right]dm \\ \mathcal{B}_{\text{out}}(\mathbf{r}) &= -\frac{i\mu_0}{8\pi}\sum_{n=-\infty}^{+\infty}\int_{-\infty}^{+\infty}\left[\nabla\times\mathbf{A}_{n,\eta}(m,\mathbf{r})V_n^A(m)+\nabla\times\mathbf{B}_{n,\eta}(m,\mathbf{r})V_n^B(m)\right]dm\end{aligned} \quad ,(4.12)$$

where $\mathbf{A}_{n,\eta}(m,\mathbf{r})$ and $\mathbf{B}_{n,\eta}(m,\mathbf{r})$ are combinations of vector wave functions, with the eigenvalue parameter γ replaced for the region outside the cylinder by:

$$\eta^2 = k_0{}^2 - m^2 = \omega^2\varepsilon_0\mu_0 - m^2, \tag{4.13}$$

The coefficients $V_n^A(m)$, $V_n^B(m)$ are defined as:

$$\begin{pmatrix}V_n^A(m)\\V_n^B(m)\end{pmatrix} = \mathbf{V} = \mathbf{U}^{\mathrm{T}}\mathbf{W} = \mathbf{U}^{\mathrm{T}}\begin{pmatrix}W_n^{(M)}(m)\\W_n^{(E)}(m)\end{pmatrix} \tag{4.14}$$

Here the transformation matrix **U** sets the boundary conditions at the shield surface and its expression is provided in Appendix B.

Calculation of ideal current patterns for ultimate intrinsic SNR

The complete set of EM modes can be employed to calculate the ultimate intrinsic SNR (41,42,67), independent of any coil design. A general expression for the SNR received by a coil at any particular position $\mathbf{r}_0$ can is given by:

$$\mathrm{SNR}(\mathbf{r}_0) \sim \frac{\omega_0\mathbf{M}\cdot\tilde{\mathcal{B}}^{-}(\mathbf{r}_0)^*}{\sqrt{8k_{\mathrm{B}}T_{\mathrm{S}}\cdot P_0}} = \frac{\omega_0 M_0\left(\mathcal{B}_{\mathrm{x}}(\mathbf{r}_0)-i\mathcal{B}_{\mathrm{y}}(\mathbf{r}_0)\right)}{\sqrt{8k_{\mathrm{B}}T_{\mathrm{S}}\cdot P_0}}, \tag{4.15}$$

where M_{O} is the equilibrium magnetization, ω_0 is the Larmor frequency, k_{B} is the Boltzmann's constant, T_{S} is the absolute temperature of the sample, P_0 is the total noise power at position $\mathbf{r}_0$ and, according to the principle of reciprocity (70), the net coil sensitivity is defined as the complex-conjugate of the left-hand circularly polarized component of the RF magnetic field:

$$\mathcal{B}_x(\mathbf{r}_0) - i\mathcal{B}_y(\mathbf{r}_0) = \sum_{l=0}^{+\infty} \sum_{m=-l}^{+l} \mathbf{W}^T \mathbf{T} \mathbf{S} \tag{4.16}$$

Expressions for the matrix **S** are derived in Appendix C for both spherical and cylindrical objects. In the general case P_0 includes both power loss within the load (or sample) and power loss within the antenna. The power loss due to thermal noise inside the dielectric object with uniform conductivity σ can be calculated as (see Appendix C):

$$\tilde{\mathbf{P}}_L = \frac{\sigma}{2} \iiint_V \mathbf{E}(\mathbf{r}) \cdot \mathbf{E}^*(\mathbf{r}) dV = \sum_{l=0}^{+\infty} \sum_{m=-l}^{+l} \mathbf{V}^T \mathbf{P}_L \mathbf{V}^* = \sum_{l=0}^{+\infty} \sum_{m=-l}^{+l} \mathbf{W}^T \mathbf{T} \mathbf{P}_L \left(\mathbf{T}^T \mathbf{W}\right)^*, \tag{4.17}$$

with:

$$\mathbf{P}_L = \frac{\sigma}{2} \left| \frac{\omega \mu_0}{k_{in}} \right|^2 \begin{pmatrix} \int_0^a |j_l(k_{in}\rho)|^2 \rho^2 d\rho & 0 \\ 0 & \frac{1}{|k_{in}|^2} \left\{ \int_0^a \left[\left| \frac{\partial [\rho j_l(k_{in}\rho)]}{\partial \rho} \right|^2 + l(l+1) |j_l(k_{in}\rho)|^2 \right] d\rho \right\} \end{pmatrix}, \tag{4.18}$$

for the case of a sphere with radius a. For the case of a cylinder with radius a, an expression for $\mathbf{P}_L$ is derived in Ref. (110):

$$\mathbf{P}_L = \frac{\sigma}{2} \left(\frac{\omega \mu_0}{4} \right)^2 \frac{\gamma \gamma^*}{2} \begin{bmatrix} F_{n-1} + F_{n+1} & \frac{m}{k_{in}^*} \left[F_{n-1} - F_{n+1} \right] \\ \frac{m}{k_{in}} \left[F_{n-1} - F_{n+1} \right] & \frac{m^2}{k_{in} k_{in}^*} \left[F_{n-1} + F_{n+1} + 2 \frac{\gamma \gamma^*}{m^2} F_n \right] \end{bmatrix} \tag{4.19}$$

with:

$$F_n = \int_0^a J_n(\gamma \rho) J_n\left(\gamma^* \rho\right) \rho d\rho = \frac{\gamma^* a J_{n-1}\left(\gamma^* a\right) J_n(\gamma a) - \gamma a J_{n-1}(\gamma a) J_n\left(\gamma^* a\right)}{\gamma^2 - \gamma^{*2}} \tag{4.20}$$

The power loss due to the presence of the surface current distribution, assuming the hypothetical coil material has thickness d_c and conductivity σ_c, can be calculated as (see Appendix C):

$$\tilde{\mathbf{P}}_A = \frac{1}{2\sigma_c d_c}\iint_{A'} \mathbf{K}(\mathbf{r}')\cdot\mathbf{K}^*(\mathbf{r}')dA' = \sum_{l=0}^{+\infty}\sum_{m=-l}^{+l}\mathbf{W}^{\mathrm{T}}\mathbf{P}_A\mathbf{W}^*. \tag{4.21}$$

If we define the current distribution to be on a surface with radius ρ_c, for the case of the sphere we have:

$$\mathbf{P}_A = \frac{l(l+1)\rho_c^2}{2\sigma_c d_c}\begin{pmatrix}1 & 0\\ 0 & 1\end{pmatrix}, \tag{4.22}$$

whereas for the case of the cylinder:

$$\mathbf{P}_A = \frac{2\pi^2\rho_c}{\sigma_c d_c}\left[m^2 + \left(\frac{n}{b}\right)^2\right]\begin{pmatrix}1 & 0\\ 0 & 1\end{pmatrix}. \tag{4.23}$$

We added the ρ_c in Eq. (4.23), to account for a typographical error in Ref. (110). We can now write a general expression for the total noise power:

$$\begin{aligned} P_0 = \left(\tilde{\mathbf{P}}_L + \tilde{\mathbf{P}}_A\right)_{0,0} &= \left(\sum_{l=0}^{+\infty}\sum_{m=-l}^{+l}\left(\mathbf{W}^{\mathrm{T}}\mathbf{T}\mathbf{P}_L\left(\mathbf{T}^{\mathrm{T}}\mathbf{W}\right)^* + \mathbf{W}^{\mathrm{T}}\mathbf{P}_A\mathbf{W}^*\right)\right)_{0,0} \\ &= \left(\sum_{l=0}^{+\infty}\sum_{m=-l}^{+l}\mathbf{W}^H\boldsymbol{\Psi}_{\mathrm{mode}}\,\mathbf{W}\right)_{0,0} \end{aligned} \tag{4.24}$$

Here the superscript $^{\mathrm{H}}$ denotes conjugate (Hermitian) transpose. For the case of the cylinder, where the double sum in l and m becomes a sum in n and an integration in m, if we want to include the effect of the noise due to currents circulating in the conductive shield, we need to add $\mathbf{U}\mathbf{P}_S\mathbf{U}^H$ to $\boldsymbol{\Psi}_{\mathrm{mode}}$, where $\mathbf{P}_S$ is a power loss term calculated with the integral:

$$\tilde{\mathbf{P}}_S = \frac{1}{2\sigma_S d_S}\iint_{A'}\mathbf{K}_S(\mathbf{r}')\cdot\mathbf{K}_S^*(\mathbf{r}')dA' = \sum_{n=-\infty}^{+\infty}\int_{-\infty}^{+\infty}\mathbf{U}^{\mathrm{T}}\mathbf{P}_S\mathbf{U}^*dm, \tag{4.25}$$

where d_S is the thickness of the shield material, σ_S its conductivity and the current induced in the shield is calculated as (Appendix C):

$$\mathbf{K}_S(\mathbf{r}) = \frac{1}{\mu_0}\boldsymbol{\mathcal{B}}_{\mathrm{out}}(\mathbf{r})\big|_{\rho=\rho_s}\times\hat{\rho}. \tag{4.26}$$

For Cartesian SENSE parallel imaging reconstructions (16), optimal SNR is achieved by finding the coefficients that minimize Eq. (4.24) while having Eq. (4.16) equal to unity at the reconstructed voxel position $\mathbf{r}_0$ and zero at all aliasing positions. The solution was given by Pruessmann et al. (16):

$$\mathbf{W}^{opt} = \left(\mathbf{B}^H \boldsymbol{\Psi}_{\text{mode}}^{-1} \mathbf{B}\right)^{-1} \mathbf{B}^H \boldsymbol{\Psi}_{\text{mode}}^{-1}, \tag{4.27}$$

where **B=TS** is the so-called encoding matrix. Substituting $\mathbf{W}^{opt}$ yields an expression for the ultimate intrinsic SNR:

$$\tilde{\zeta}(\mathbf{r}_0) \sim \frac{\omega_0 M_0}{\sqrt{8k_B T_S \cdot \left[\mathbf{S}^H \mathbf{T}^H \left(\mathbf{T}\mathbf{P}_L \mathbf{T}^H + \mathbf{P}_A\right)^{-1} \mathbf{T}\mathbf{S}\right]^{-1}_{0,0}}} = \frac{\omega_0 M_0}{\sqrt{8k_B T_S \cdot \left(\mathbf{B}^H \boldsymbol{\Psi}_{\text{mode}}^{-1} \mathbf{B}\right)^{-1}_{0,0}}}. \tag{4.28}$$

For the case of the cylinder, if we include the conductive shield, the noise matrix $\boldsymbol{\Psi}_{\text{mode}}$ in the denominator will have the additional term $\mathbf{U}\mathbf{P}_S\mathbf{U}^H$. Note that, if we remove $\mathbf{P}_A$ and allow a fully general set of current modes, the boundary condition matrix **T** disappears from the denominator of Eq. (4.28) and the expression for ultimate intrinsic SNR matches that derived by Wiesinger et al. using multipole EM field expansion in a sphere (42). However, the DGF approach begins by defining current distributions, so it has the advantage that we can use the optimal coefficients $\mathbf{W}^{opt}$ in Eq. (4.5) and (4.8) to perform a weighted sum of the individual current modes and find the ideal surface current patterns that results in the ultimate intrinsic SNR. For the case of the sphere the expression is:

$$\mathbf{I}_{\text{Rx}}^{ideal}(\theta,\varphi) = \sum_{l=0}^{+\infty} \sum_{m=-l}^{+l} \mathbf{K}_{l,m}^{opt}(\theta,\varphi) = \sum_{l=0}^{+\infty} \sum_{m=-l}^{+l} \left(\mathbf{W}^{opt}\right)^{\mathrm{T}} \begin{pmatrix} \mathbf{X}_{l,m}(\theta,\varphi) \\ \hat{\rho} \times \mathbf{X}_{l,m}(\theta,\varphi) \end{pmatrix} \tag{4.29}$$

and for the cylinder:

$$\mathbf{I}_{\text{Rx}}^{ideal}(\varphi,z) = \sum_{n=-\infty}^{\infty} \int_{-\infty}^{\infty} \mathbf{K}_n^{opt}(m,\varphi,z)dm = \sum_{n=-\infty}^{\infty} \int_{-\infty}^{\infty} \left(\mathbf{W}^{opt}\right)^{\mathrm{T}} \begin{pmatrix} im\hat{\varphi} - \dfrac{in}{\rho_c}\hat{z} \\ \dfrac{in}{\rho_c}\hat{\varphi} + im\hat{z} \end{pmatrix} e^{in\varphi} e^{imz} dm \tag{4.30}$$

Calculation of ideal current patterns for ultimate intrinsic SAR

The DGF formulation also extends naturally to SAR analysis in the transmit case, as the electric field resulting from an arbitrary current distribution can be applied directly to calculate the average RF power deposition in the object (59):

$$\xi = \frac{1}{P}\sum_{p=1}^{P}\frac{\sigma}{2}\iiint_{V}\mathcal{E}(\mathbf{r},p\Delta t)\cdot\mathcal{E}^{*}(\mathbf{r},p\Delta t)dV = \frac{1}{P}\sum_{p=1}^{P}\sum_{l=0}^{+\infty}\sum_{l'=0}^{+\infty}\sum_{m=-l}^{+l}\sum_{m'=-l'}^{+l'}\mathbf{W}_{p}^{\mathrm{T}}\boldsymbol{\Phi}\mathbf{W}_{p}^{*}, \qquad (4.31)$$

where P is the total number of time periods in the excitation, $\boldsymbol{\Phi}$ is an electric field correlation matrix, defined for each mode and equal by reciprocity to the sample noise covariance matrix $\mathbf{TP}_{L}\mathbf{T}^{H}$ in Eq. (4.18) and $\mathbf{W}_{p}$ are the weighting coefficients (see Eq. (4.5)) of the current distribution at time period p. Eq. (4.31) is a measure of global SAR and in the case of rectilinear EPI-type excitation trajectories can be re-written in image domain as a quadratic function in the RF excitation patterns $\mathbf{f}_{n}$ generated by the transmit coils (59,64,109):

$$\xi = \frac{1}{N}\sum_{n=1}^{N}\mathbf{f}_{n}^{H}\,\boldsymbol{\Phi}\,\mathbf{f}_{n}, \qquad (4.32)$$

where N is the total number of voxels. Time intervals p are mapped to spatial voxel locations n by Fourier transformation and $\mathbf{W}_{p} = \mathcal{F}^{-1}\{\mathbf{f}_{n}\}$, where $\mathcal{F}$ indicates the Fourier transform. In parallel transmission (58,59) it is possible to combine the excitations of the individual transmit elements in a way that minimizes global SAR (64,109):

$$\mathbf{f}_{n}^{opt} = \boldsymbol{\Phi}^{-1}\mathbf{C}_{n}^{H}(\mathbf{C}_{n}\boldsymbol{\Phi}^{-1}\mathbf{C}_{n}^{H})^{-1}\boldsymbol{\mu}_{n}, \qquad (4.33)$$

where μ_{n} is the target excitation and the matrix $\mathbf{C}_{n}$ is a spatial-weighting map made up of the transmit sensitivities. $\mathbf{C}_{n}$ is analogous to the matrix **TS** in Eq. (4.16), with the right circularly polarized component of the magnetic field, i.e. $\mathcal{B}_{x}(\mathbf{r}_{0}) + i\mathcal{B}_{y}(\mathbf{r}_{0})$, instead of the left one. Substituting Eq. (4.33) in Eq (4.32) we obtain an expression for the ultimate intrinsic SAR (109):

$$\tilde{\xi} = \frac{1}{N}\sum_{n=1}^{N}\left[\boldsymbol{\mu}_{n}^{H}(\mathbf{C}_{n}\boldsymbol{\Phi}^{-1}\mathbf{C}_{n}^{H})^{-1}\boldsymbol{\mu}_{n}\right] \qquad (4.34)$$

In the transmit case, ideal surface current patterns corresponding to the theoretically smallest global SAR are calculated as a function of time, while traversing excitation *k*-space:

$$\mathbf{I}_{\mathrm{Tx},\,p\Delta t}^{ideal}(\theta,\varphi)=\sum_{l=0}^{+\infty}\sum_{m=-l}^{+l}\mathbf{K}_{l,m}^{opt}(\theta,\varphi,p\Delta t)=\sum_{l=0}^{+\infty}\sum_{m=-l}^{+l}\left(\mathcal{F}^{-1}\left\{\mathbf{f}_{n}^{opt}\right\}\right)^{\mathrm{T}}\begin{pmatrix}\mathbf{X}_{l,m}(\theta,\varphi)\\ \hat{\rho}\times\mathbf{X}_{l,m}(\theta,\varphi)\end{pmatrix}. \tag{4.35}$$

This expression refers to the case of a spherical object, but it can be derived analogously for a cylinder from Eq. (4.8):

$$\mathbf{I}_{\mathrm{Tx},\,p\Delta t}^{ideal}(\theta,\varphi)=\sum_{n=-\infty}^{\infty}\int_{-\infty}^{\infty}\mathbf{K}_{n}^{opt}(m,\varphi,z,p\Delta t)dm=\sum_{n=-\infty}^{\infty}\int_{-\infty}^{\infty}\left(\mathcal{F}^{-1}\left\{\mathbf{f}_{n}^{opt}\right\}\right)^{\mathrm{T}}\begin{pmatrix}im\hat{\varphi}-\dfrac{in}{\rho_c}\hat{z}\\ \dfrac{in}{\rho_c}\hat{\varphi}+im\hat{z}\end{pmatrix}e^{in\varphi}e^{imz}dm \tag{4.36}$$

In RF shimming (55,57), a special time-independent case of parallel transmission, where there is a single driving RF current that is modulated in phase and amplitude at each coil element, optimal modulation coefficients can be found using a similar SAR minimization approach (112).

Optimal currents for circular surface coils

In the previous sections, we showed that we can use a complete set of basis functions to simulate the optimal SNR and SAR achievable with an infinite number of coils. The performance of any actual coil in the case of a spherical sample can be simulated with the same formulas if we apply the appropriate weighting functions to the current distribution in Eq. (4.5). Let us consider a loop coil of radius *R* positioned outside the dielectric sphere, with axis along the z-axis and at a distance *d* from the center of the sphere (Figure 4-1). The current distribution for this coil can be defined as:

$$\mathbf{K}_{z}^{loop}(\theta,\varphi)=\hat{\varphi}I\frac{\sin\theta}{\sqrt{d^2+R^2}}\delta\left(\rho-\sqrt{d^2+R^2}\right)\delta\left(\cos\theta-\frac{d}{\sqrt{d^2+R^2}}\right), \tag{4.37}$$

where I is the current circulating in the coil, assumed to be uniform within the conductive material, and $\delta\left(\rho-\sqrt{d^2+R^2}\right)=1$, as the current is defined only on the spherical surface of radius $\rho_c=\sqrt{d^2+R^2}$. The proportionality factor $\sin\theta/\sqrt{d^2+R^2}$ guarantees that the flux of $\mathbf{K}_z^{loop}$ through any half plane of constant θ (polar angle) is equal to I (the proportionality factor is the inverse of the Jacobian resulting from the integration in polar coordinates of $\mathbf{K}_z^{loop}\cdot\hat{\varphi}$ on a plane defined by a constant θ, where, due to the orientation and position of the coil, $\hat{\varphi}$ corresponds to the normal $\hat{\mathbf{n}}$ of the plane).

In the case of a loop coil, currents can only flow in closed patterns, so curl-free contributions are zero in Eq. (4.5):

$$\mathbf{K}(\theta,\varphi)=\sum_{l=0}^{+\infty}\sum_{m=-l}^{+l}W_{l,m}^{(M)}\left(-i\sqrt{l(l+1)}\mathbf{X}_{l,m}(\theta,\varphi)\right) \tag{4.38}$$

The last two equations must be equivalent and, if we compare them, we find an expression for $W_{l,m}^{(M)}$ associated to the particular loop coil (see Appendix D):

$$W_{l,0}^{loop,(M)}=\frac{-i2\pi R}{d^2+R^2}\frac{1}{(l+1)}\left(\cot\theta\,\mathrm{Y}_l^0(\theta,\varphi)-\csc\theta\sqrt{\frac{2l+1}{2l-1}}\mathrm{Y}_{l-1}^0(\theta,\varphi)\right)_{\theta=\arccos\frac{d}{\sqrt{d^2+R^2}}}. \tag{4.39}$$

We have substituted $I=1$, as, for the purposes of modeling coil sensitivities by reciprocity, we are interested in unit current. The current density for a loop coil rotated to an arbitrary position on the sphere (Figure 4-1) has the same functional form as that of the loop coil along the z-axis, but in a coordinate system rotated with respect to the reference coordinate system:

$$\mathbf{K}_{rot}^{loop}(\theta,\varphi)\equiv\mathbf{K}_{z'}^{'loop}(\theta',\varphi')=\sum_{l=0}^{+\infty}W_{l,0}^{'loop,(M)}\left[-i\sqrt{l(l+1)}\mathbf{X}'_{l,0}(\theta',\varphi')\right] \tag{4.40}$$

Rotated vector spherical harmonics can be always represented as a linear superposition of unrotated vector harmonics (see Appendix D):

$$\mathbf{X}'_{l,0}(\theta',\varphi') = \sqrt{\frac{4\pi}{2l+1}} \sum_{m=-l}^{l} Y_l^{m*}(\beta,\alpha)\mathbf{X}_{l,m}(\theta,\varphi), \tag{4.41}$$

where α and β define the angular position of the center of the rotated coil on the unit sphere. Substituting in Eq. (4.40) we obtain:

$$\begin{aligned}\mathbf{K}_{rot}^{loop}(\theta,\varphi) &= \sum_{l=0}^{+\infty}\sum_{m=-l}^{l} W_{l,0}^{'loop,(M)} \sqrt{\frac{4\pi}{2l+1}} Y_l^{m*}(\beta,\alpha)\left[-i\sqrt{l(l+1)}\mathbf{X}_{l,m}(\vartheta,\phi)\right] \\ &= \sum_{l=0}^{+\infty}\sum_{m=-l}^{l} W_{l,m}^{loop,(M)}\left[-i\sqrt{l(l+1)}\mathbf{X}_{l,m}(\vartheta,\phi)\right]\end{aligned}, \tag{4.42}$$

where the weights for the rotated coil are given by:

$$W_{l,m}^{loop,(M)} = \sqrt{\frac{4\pi}{2l+1}} Y_l^{m*}(\beta,\alpha) W_{l,0}^{(M)} \tag{4.43}$$

In order to calculate optimal SNR for an array of Υ receive loop coils, we need to derive the coil sensitivities and the noise correlation matrix among coils. That can be achieved by substituting the weights in the expressions in Eq. (4.16) and (4.24):

$$\begin{aligned}\mathcal{B}_{x,\gamma}^{loop}(\mathbf{r}_0) - i\mathcal{B}_{y,\gamma}^{loop}(\mathbf{r}_0) &= \sum_{l=0}^{+\infty}\sum_{m=-l}^{+l}\begin{pmatrix} W_{(l,m),\gamma}^{loop,(M)} \\ 0 \end{pmatrix}^{T} \mathbf{T}\,\mathbf{S} \\ P_{\gamma\gamma'}^{loop} &= \left(\sum_{l=0}^{+\infty}\sum_{m=-l}^{+l}\begin{pmatrix} W_{(l,m),\gamma}^{loop,(M)} \\ 0 \end{pmatrix}^{T} \boldsymbol{\Psi}_{\text{mode}} \begin{pmatrix} W_{(l,m),\gamma'}^{loop,(M)} \\ 0 \end{pmatrix}^{*}\right)\end{aligned} \tag{4.44}$$

The resulting matrices will then be combined as in Eq. (4.28) to find the optimal SNR. The method can be extended straightforwardly to the calculation of minimum SAR for an array of transmit loop coils.

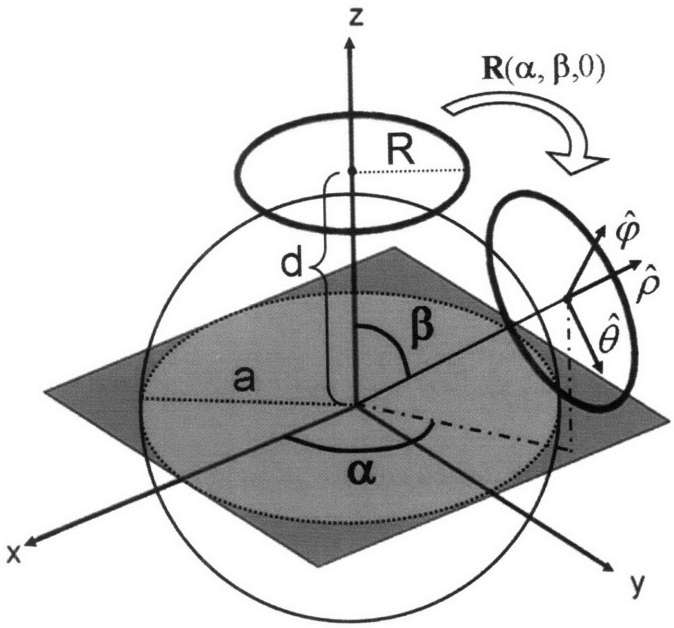

Figure 4-1. Schematic representation of the spherical sample geometry, with two loop coils arranged on a spherical surface at distance $\sqrt{d^2 + R^2}$ from the center of the sphere. SNR and SAR calculations were performed on a transverse plane through the center of the object.

Optimal currents for cylindrical window coils

The formalism can be implemented as well for the case of an array of cylindrical window coils (Figure 4-2). The weights to be applied to the divergence-free component of the current distribution in Eq. (4.8) for the γ^{th} coil are (Appendix D):

$$W_{n,\gamma}^{window,(M)}(m) = 2\frac{\sin(n\varphi_{0_\gamma})}{n}\frac{\sin(md_\gamma)}{m}e^{-jn\Delta\varphi_\gamma}e^{-jm\Delta z_\gamma} \tag{4.45}$$

where $2\varphi_{0_\gamma}$ is the angular aperture of the γ^{th} coil, $2d_\gamma$ is the coil's axial extent, and $\Delta\varphi_\gamma$ and Δz_γ are its the azimuthal and axial offsets.

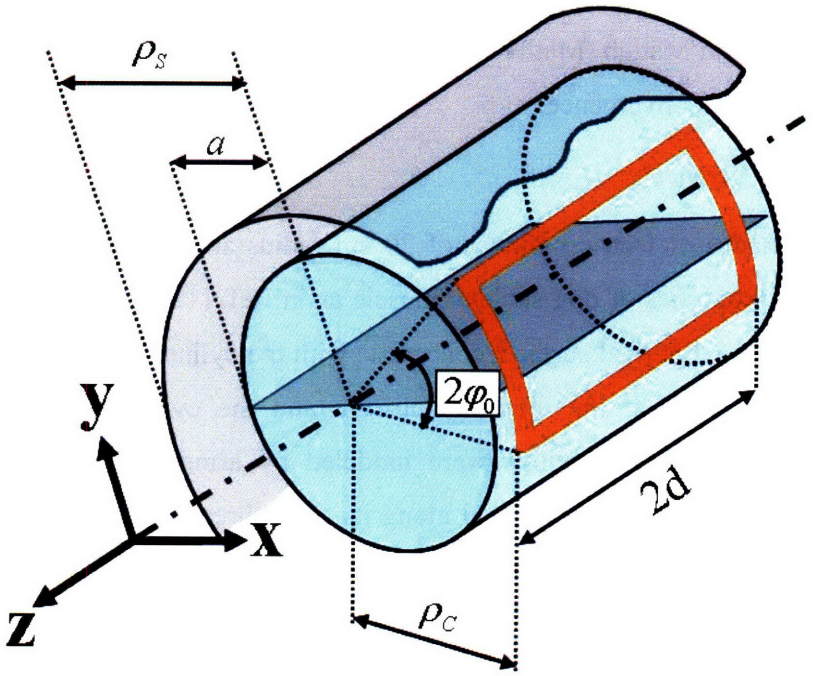

Figure 4-2. Schematic representation of the cylindrical sample geometry, with a cylindrical window coil modeled on a surface between the object and the surrounding conductive shield. The chosen FOV was a transverse plane at the level of the cylinder axis.

Methods

Spherical geometry

SNR and SAR calculations were performed on a transverse plane (Figure 4-1) through the center of a sphere with uniform electrical properties, chosen to approximate average values in the human head as in Ref. (42). SAR was calculated assuming a homogeneous excitation profile on the field of view (FOV). For the ultimate case, we used sphere radius of 10 cm and the current distribution was defined on a spherical surface at radius ρ_C = 10.5 cm from the center of the sphere. Finite arrays of identical loop coils were modeled with different number of elements and various geometrical arrangements. The radius $\sqrt{d^2 + R^2}$ of the spherical surface on which the coils are placed was 10% larger than the radius a of the dielectric sphere. Copper conductivity

and conductor thickness equal to skin depth was assumed. Calculations were implemented in Matlab (MathWorks, Natick, MA, USA) using an expansion order l_{max} = 70, to ensure convergence.

Cylindrical geometry

We modeled a dielectric cylinder of 20 cm radius and length L = 90 cm, assuming dielectric properties of dog skeletal muscle as in Ref. (110). Current distribution was defined on a cylindrical surface, concentric with the cylindrical body and with radius 5 mm larger, for both the ultimate intrinsic and the cylindrical window coil case. Different array configurations were modeled by arranging identical coil elements around the cylindrical surface and along its axial direction, with 10% overlapping on each side. The conductive shield was positioned at a radial distance of 34.25 cm from the center of the cylinder. For both coils and shield we assumed copper conductivity and conductor thickness equal to skin depth. The expansion coefficient n was varied from -40 to +40 with unit step, whereas m, which in theory should be continuous, was varied from -50 to +50 with step $\Delta m = 1/L$. For large m, both γ and η acquire a substantial imaginary component, and the square root branches which yield $\mathrm{Im}(\gamma) < 0$ and $\mathrm{Im}(\eta) < 0$ must be chosen independently for each value of m. This selection guarantees that the Bessel functions with argument $\gamma\rho$ or $\eta\rho$ – and hence the electromagnetic fields associated with each mode – remain appropriately bounded with increasing radius. (If the opposite branch were chosen, the fields would also diverge unphysically at large m, a fact noted in Ref. (113)). Calculations were implemented in Matlab and performed at voxel locations on a transverse FOV (Figure 4-2).

Results

Ultimate intrinsic SNR and optimal SNR for finite coil arrays were calculated within the same theoretical framework, allowing for direct comparison, without concern about differential scaling factors. Figure 4-3 shows SNR efficiency, with respect to the best possible performance, of arrays of loop coils symmetrically packed around the

spherical sample, at different voxel locations and for different values of the main magnetic field strength. We note that, near the center of the object, the SNR of the array converges rapidly to the ultimate value at 1.5 T as the number of coil elements increases, whereas the performance worsens at higher frequencies. For a voxel near the surface of the sphere, with 64 coils the resulting SNR is less than 15% of the optimum.

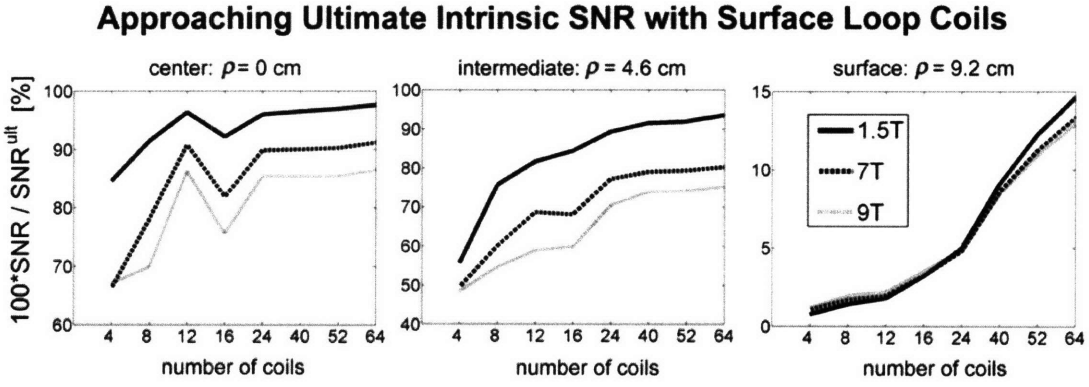

Figure 4-3. SNR of an array of loop coils, normalized to the ultimate intrinsic SNR, as a function of number of coil elements, at various positions along the radius ρ of the dielectric sphere, for different values of main magnetic field strength, in the unaccelerated case.

In the definition of the ultimate intrinsic SNR, power losses are due only to thermal noise in the sample, which is equivalent to assuming that the conductors have infinite conductivity and do not contribute with resistive losses. This additional source of noise would have a negligible effect on the SNR in the center but, as we see in Figure 4-4, it would dramatically lower ultimate intrinsic SNR, therefore improving the expected coil efficiency, at positions near the surface of the sphere, which are closer to the region where the current distribution is defined.

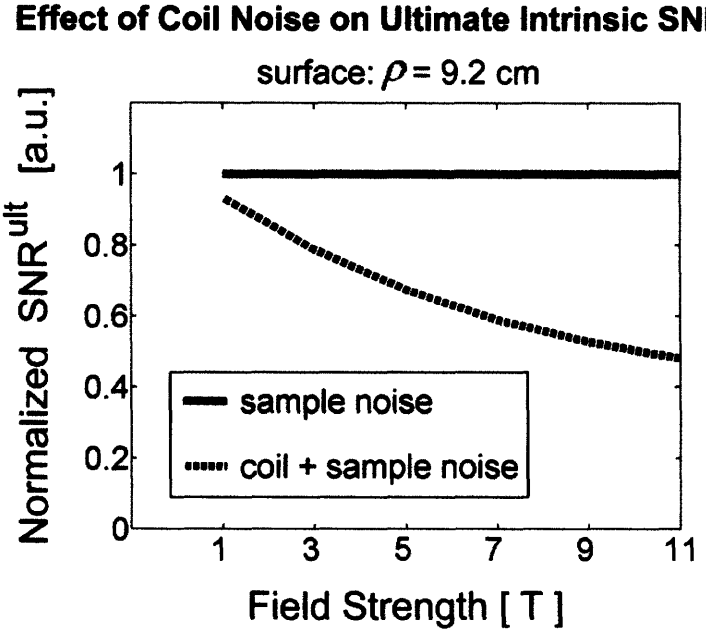

Figure 4-4. Ultimate intrinsic SNR, normalized to the case where only sample-derived noise contributions are considered, at a position near the surface of the sphere, as a function of main magnetic field strength. Adding coil-derived power loss in the model reduces SNR in regions near the conductors, especially at high field.

Ideal current patterns associated with the best possible SNR at 11 T are shown in Figure 4-5 for a voxel at the center of the sphere. The ideal currents circulate in wide loops embracing the spherical surface and we see that with 64 coils, symmetrically arranged around the object, it is possible to capture most of this behavior, as the resulting SNR is 83% of its theoretical limit. With 8 coils, the current patterns, which are constrained by the position of the conductors, only cover a limited region of the spherical surface and the resulting performance is lower.

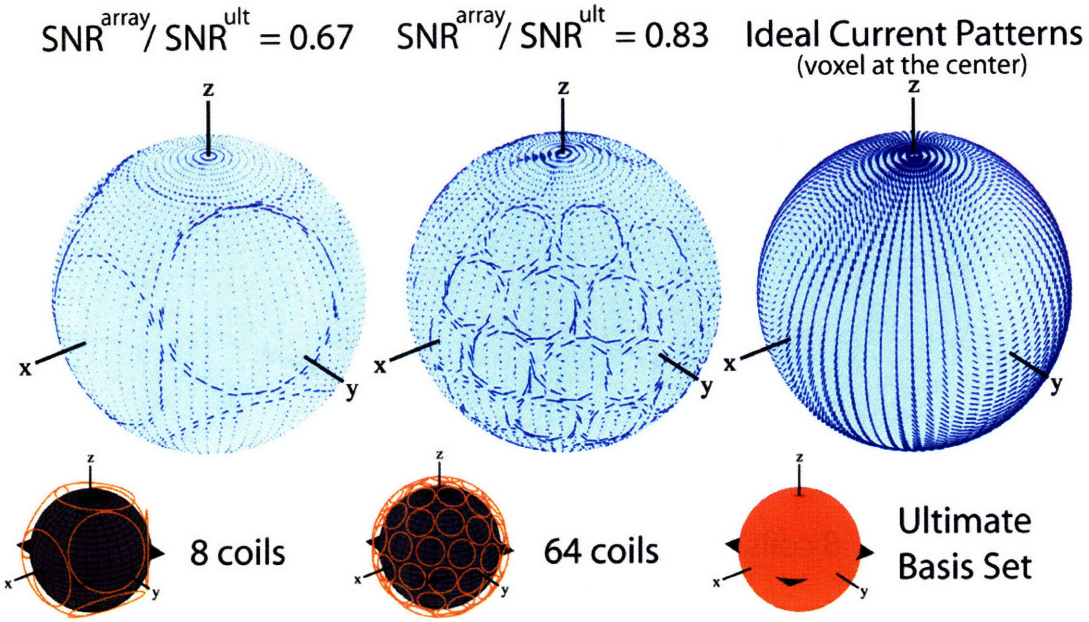

Figure 4-5. Ideal surface current patterns, associated to the best possible SNR at a voxel in the center of the sphere, are compared, at 11 T, with SNR-optimized current patterns for an 8-element and a 64-element array. The corresponding SNR, normalized to the ultimate intrinsic SNR, is reported for both coils above the current plots.

The same graphical representation is used in Figure 4-6 for the case of a voxel located about at the same distance from the center and the surface of the sphere. Here, ideal current patterns are concentrated in a small loop centered at the azimuthal coordinate corresponding to the voxel of interest. In the case of the 64-element array, we notice that only the coils localized in the same region are active, minimizing in this way the noise received from other regions. If the same encircling packing is used for the 8-element array, SNR efficiency drops from 70% to 31% of the optimum. However, the performance can be improved by arranging 8 coils around the FOV, or by using a single coil that mimic the behavior of the ideal current patterns.

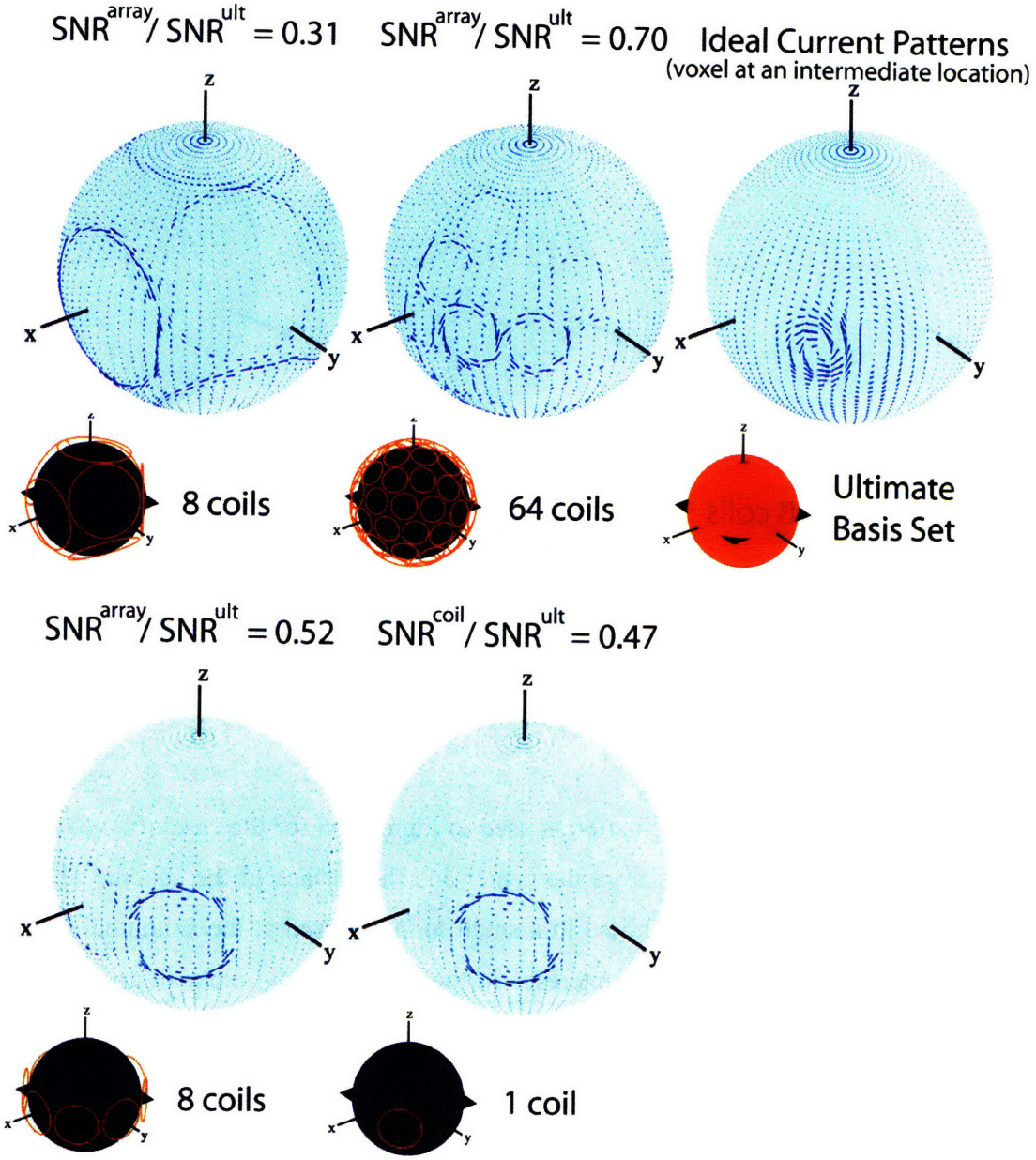

Figure 4-6. Ideal surface current patterns, associated to the best possible SNR at a voxel position intermediate between the center and the surface of the sphere, are compared, at 11 T, with SNR-optimized current patterns for different coil configurations. The corresponding SNR values, normalized to the ultimate intrinsic SNR, are reported above the current plots. Only coil elements in the region near the voxel of interest are active.

In Figure 4-7 the efficiency of various receive arrays, with an increased number of coil elements symmetrically packed around the sphere, is evaluated in the case of 4-fold acceleration, in terms of the geometry factor (g) (16). g, by definition greater than or equal to one, is a measure of the spatially varying noise amplifications associated to parallel imaging reconstructions and depends on the reciprocal orthogonality between coil sensitivity functions. We see that accelerating by a factor of 4 with a 64-element array is almost equivalent to using an infinite number coils. At 1.5 T (top row), the ratio of the lowest possible g to the g of the arrays is smaller than at 7 T, indicating that the coils are more efficient in accelerating image acquisition at higher frequencies.

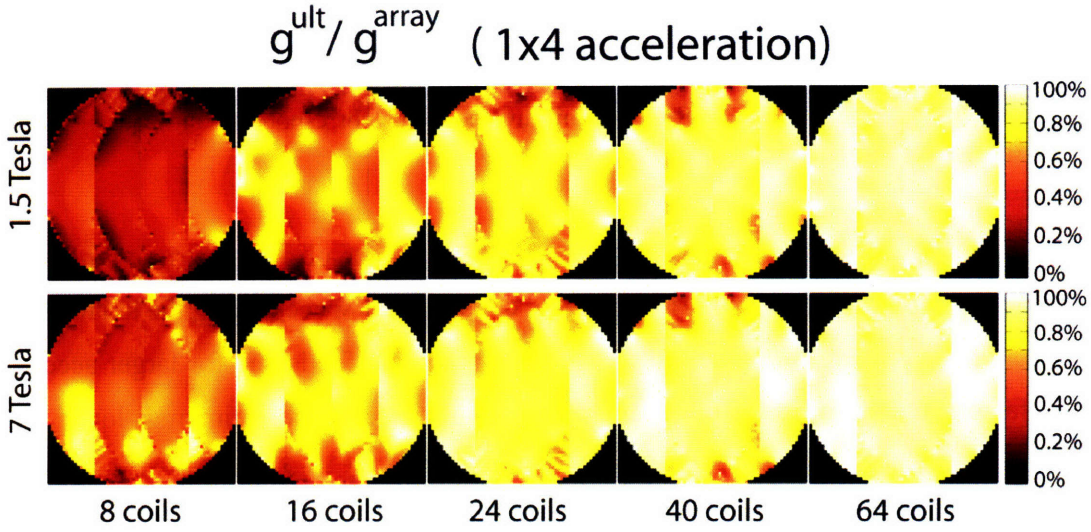

Figure 4-7. Coil efficiency as a percentage of the optimum for 4-fold linear accelerations. The geometry factor of receive arrays with an increasing number of loop coil elements is reported with respect to the ultimate intrinsic case, at 1.5 T and 7 T.

However, the overall coil performance is always higher at lower frequencies, as we see in Figure 4-8, which shows, for the same simulation, coil performance maps (68), displaying at each pixel display the SNR of the array divided by the corresponding ultimate intrinsic SNR.

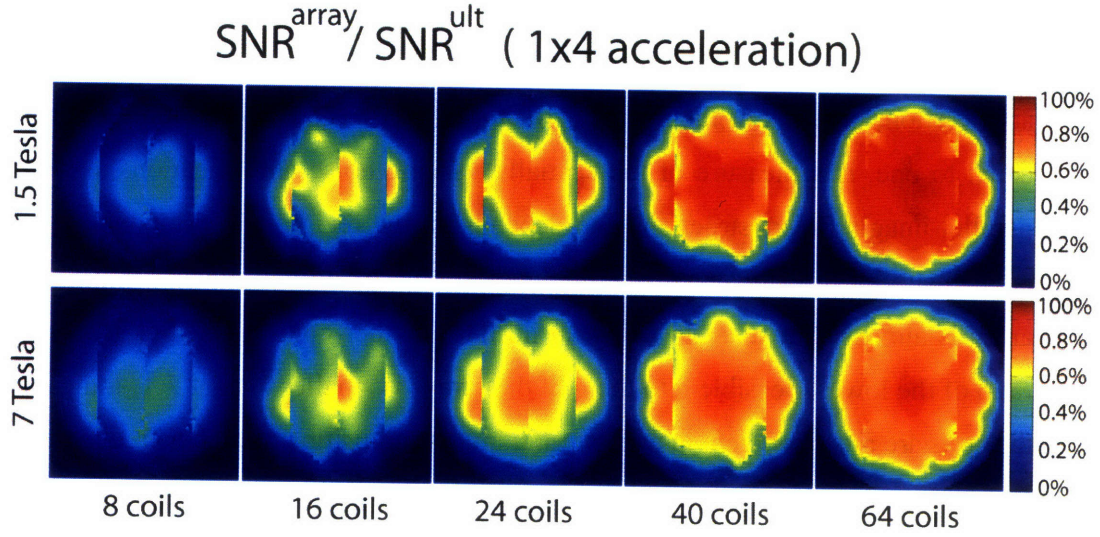

Figure 4-8. Coil performance maps in the case of 4-fold accelerated parallel imaging. The performance of receive coil arrays with respect to the ultimate intrinsic SNR is shown for two different values of the main magnetic field strength and increasing number of coil elements. Each pixel represents the SNR of the coil divided by its corresponding ultimate intrinsic SNR value.

Ultimate intrinsic SNR is approached near the center of a dielectric cylinder with a sufficient number of cylindrical window coils equally spaced along the axial and radial direction (Figure 4-9 and 4-10). At higher magnetic fields and for larger acceleration factors, the performance of the coil arrays with respect to the optimum is lower.

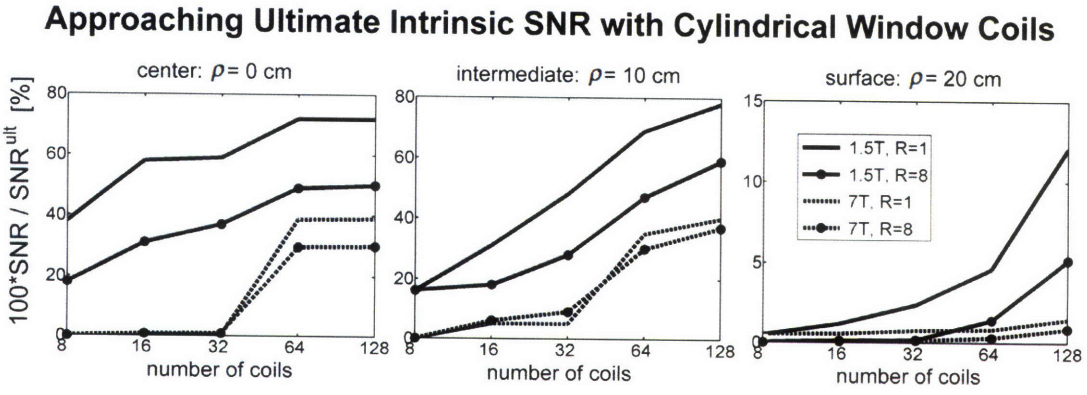

Figure 4-9. SNR, normalized to the ultimate intrinsic SNR, as a function of number of coil elements, at various positions along the radius ρ of the dielectric cylinder, for different values of main magnetic field strength and acceleration factor.

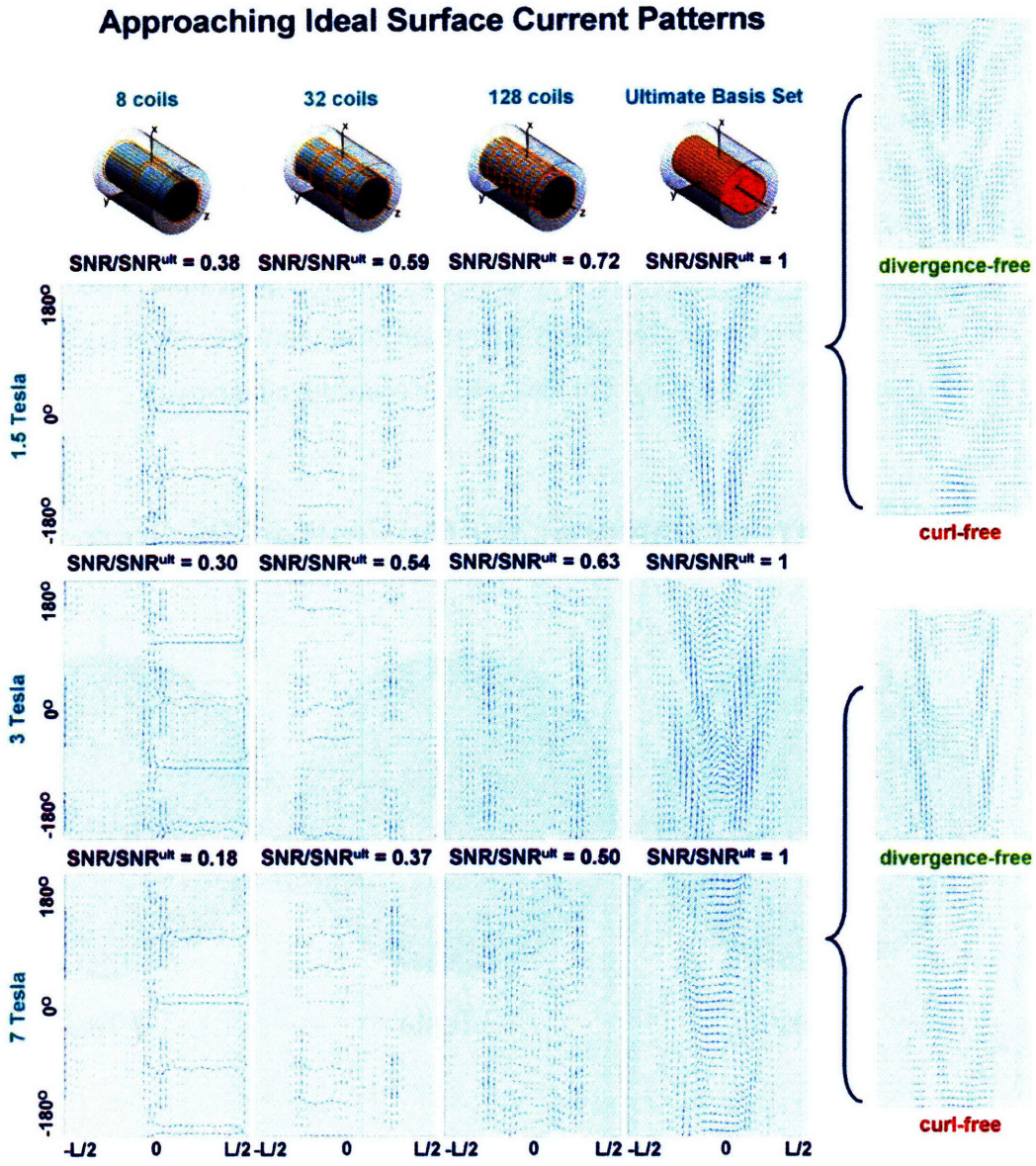

Figure 4-10. Ideal surface current patterns compared with surface current patterns from cylindrical window coil arrays, for a reconstructed voxel in the center of the object, in the unaccelerated case for different magnetic field strengths. The plots represent 2D "unwrapped" views of the 3D cylindrical surface. The axial and the azimuthal coordinates are on the horizontal and vertical axis, respectively. Divergence-free and curl-free contributions to the ideal current patterns are plotted separately in two cases to show the increasing effect of electric dipole currents at high field.

In Figure 4-10, optimal current patterns for the case of a voxel along the axis of the cylinder are compared with the corresponding ideal current patterns. Although with a 128-element array the shape of the current patterns resembles the ideal distribution, even in the best case (i.e. 1.5 T), the resulting SNR is only about 70% of the optimum. If we decompose the ideal current patterns in their divergence-free and curl-free components, we notice that at 1.5 T the dominant contribution is from closed-loop type currents, as the divergence-free plot is almost identical to the plot showing the sum of the two parts. At 7 T, the weight of the curl-free contribution increases.

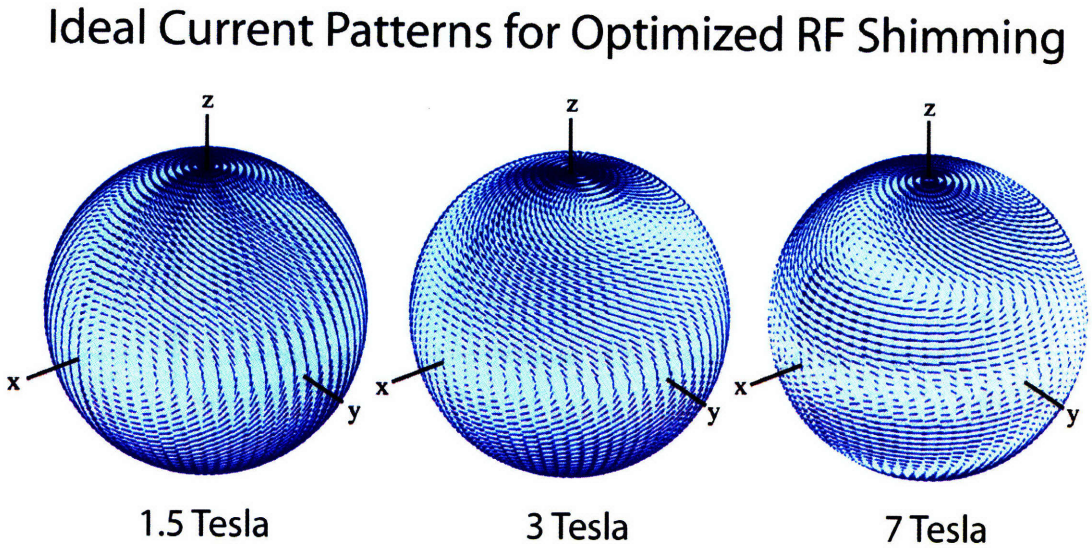

Figure 4-11. Ideal current patterns resulting in the lowest possible SAR with RF shimming, during the excitation of a homogeneous profile on the FOV. The simple loop shapes at 1.5 T are compared with the increasingly complex patterns at higher field.

In Figure 4-11 we show ideal current patterns, corresponding to the excitation of a homogeneous flip angle distribution on the transverse plane through the center of the sphere, with the theoretically smallest SAR. The optimization was done for RF shimming, as this technique enables achieving the desired excitation profile with a single hard pulse in the center of *k*-space, resulting in a single set of optimal currents. Ideal current patterns were calculated by summing the optimal contributions of each

current mode. Results are compared for three different values of the main magnetic field strength and we see that highly complex current patterns are needed to compensate for B_1 inhomogeneities and minimize SAR at 7 T.

Discussion

We have presented a formalism to calculate SNR and SAR within homogeneous spherical and cylindrical samples, for any surface coil geometry as well as in the ultimate intrinsic case. Our method allows for quick simulations of the physical behavior of the RF field in head and body imaging applications and provides ideal current patterns that can be used as a reference in coil design for parallel imaging and for parallel transmission.

In the case of the sphere, the theoretical framework includes as a special case a previously described theory of ultimate intrinsic SNR (42). In the case of the cylinder, we have extended a previously published method for calculating optimal SNR (110) by adapting it for parallel imaging reconstructions and by including the MR conductive shield in the model. We used a realistic noise model, in order to account for losses due not only to the sample, but also to the coil conductors and to parasitic currents induced in the conductive shield. Results about the efficiency of finite arrays in terms of the best possible performance are in agreement with previous observations (60,100), based on similar coil and sample models, but obtained with a different electrodynamic formulation.

Ideal current patterns, resulting in optimal performance, were presented for the first time by the authors at a recent conference (74,111) and here we have shown how they can be used for coil design. In Figure 4-5 we saw that the ultimate intrinsic SNR for a voxel at the center of the sample corresponds to current patterns uniformly distributed around the sphere and that it is indeed possible to capture most of the SNR theoretically available, using a sufficient number of coils symmetrically arranged around the object. At positions closer to the surface of the sphere, in accordance with

intuition, the ideal current distribution is a loop pattern aligned with the voxel of interest (Figure 4-6). This suggests that loop coils are likely to be the best choice for building receive head arrays. In transmission, ideal current patterns resulting in the theoretical smallest SAR, still look like distribute loops at low magnetic field strength, but become more complex as the frequency increases (Figure 4-11). An interesting feature that was also observed at high field (Figure 4-10) is that the curl-free component of the ideal current patterns gives an important contribution in achieving optimal SNR. That suggests that to approach the best possible performance, coil arrays for high-field MRI should consist of a combination of closed-loop conductors and electric dipoles. Although interesting from a conceptual perspective, it is expected that a similar design would raise serious concerns about decoupling between elements and RF energy deposition in patients.

The method we have developed can be a useful toolset for coil designers. It allows investigating the dependency of SNR and SAR on a multitude of factors by means of very fast simulations. The main limit is that it uses homogeneous samples. Although our formalism provide important physical insights and the general trends are expected to hold in many cases, there may be variations associated to particular heterogeneous examples and so it is important to remember that the same SAR and SNR optimization can be also implemented *as is* with any existing numerical simulation technique.

Conclusions

High and ultra-high field strengths represent an ongoing frontier for MRI, but issues related to signal transmission and signal generation become important limiting factors. In particular, SAR management and compensation of B1 inhomogeneities are critical issues, which require careful design and evaluation of RF coils, RF pulses and pulse sequences. Evaluation of the specific absorption rate (SAR) is fundamental to assess potential health effects and compliance with safety standards. On the other hand, modeling of the SNR has become a common phase during the design of RF detector coil arrays, as the number of elements, as well as their geometrical arrangement, is

fundamental for achieving many-fold accelerations with parallel imaging techniques. In this work we described a semi-analytical method to calculate SNR and SAR based on a mode expansion using dyadic Green's functions in a dielectric sphere and in a dielectric cylinder. Ultimate intrinsic SNR and SAR can be computed by employing a complete set of surface current modes, and the corresponding ideal surface current patterns can be derived. This formalism holds also in the case of actual coils and can be useful to investigate the physical behaviors of the RF fields during MR reception and MR excitation. Ideal current patterns can be used as a reference to improve coil design.

Acknowledgements

The authors are grateful to Aaron Grant for helpful discussions about rotational properties of vector spherical harmonics and to Florian Wiesinger for providing code to distribute closely packed coils around a sphere.

Appendix A

Dyadic Green's functions for a dielectric sphere in free space

Choosing the appropriate DGF enables calculating the EM field from any given current density using Eq. (4.1). We start with defining two spherical vector wave functions which are solutions of the vector wave equation $\nabla\times\nabla\times\mathbf{F}-k^2\mathbf{F}=0$:

$$\begin{aligned}\mathbf{M}_{l,m}(\mathbf{r}) &= \nabla\times\left(\psi_{l,m}(\mathbf{r})\,\mathbf{r}\right)\\ \mathbf{N}_{l,m}(\mathbf{r}) &= \frac{1}{k}\nabla\times\nabla\times\left(\psi_{l,m}(\mathbf{r})\,\mathbf{r}\right)\end{aligned} \tag{4.A1}$$

where k is the complex wave number and $\psi_{lm}(\mathbf{r})$ are eigenfunctions that are solutions of the scalar wave equation $\nabla^2\psi+k^2\psi=0$ in spherical coordinates:

$$\psi_{lm}(\mathbf{r}) = \sqrt{\frac{2l+1}{4\pi}\frac{(l-m)!}{(l+m)!}} j_l(k\rho) P_l^m(\cos\vartheta) e^{im\phi} = j_l(k\rho) \mathrm{Y}_l^m(\vartheta,\phi). \qquad (4.A2)$$

In this expression, $P_l^m(\cos\vartheta)$ is the associated Legendre function of order (l, m), where l and m are both integers, j_l is a spherical Bessel function of order l, and Y_l^m is a spherical harmonic. Substituting Eq. (4.A2) in Eq. (4.A1), we obtain Eq. (4.2). $\mathbf{N}_{l,m}(\mathbf{r})$ and $\mathbf{M}_{l,m}(\mathbf{r})$ satisfy the symmetrical relation:

$$\begin{aligned} \mathbf{N}_{l,m}(\mathbf{r}) &= \frac{1}{k}\nabla\times\mathbf{M}_{l,m}(\mathbf{r}) \\ \mathbf{M}_{l,m}(\mathbf{r}) &= \frac{1}{k}\nabla\times\mathbf{N}_{l,m}(\mathbf{r}) \end{aligned} \qquad (4.A3)$$

For the case of a dielectric sphere of radius a immersed in free space, with its center located at the origin of the coordinate system (Figure 4-1), we define the complex wave number inside and outside the object, indicated with subscripts $_{\mathrm{in}}$ and $_0$, respectively:

$$\begin{aligned} k_0^2 &= \omega^2\mu_0\varepsilon_0 && \rho \geq a \\ k_{\mathrm{in}}^2 &= \omega^2\varepsilon_r\varepsilon_0\mu_0 + i\omega\mu_0\sigma && \rho \leq a \end{aligned} \qquad (4.A4)$$

where ω is the angular frequency, ε_r is the relative permittivity of the dielectric material, μ_0 and ε_0 are the magnetic permeability and the electric permittivity in free-space, respectively. The DGF can be constructed using the method of scattering superposition:

$$\bar{\mathbf{G}}(\mathbf{r},\mathbf{r}') = \begin{cases} \bar{\mathbf{G}}_o(\mathbf{r},\mathbf{r}') + \bar{\mathbf{G}}_s^{(1)}(\mathbf{r},\mathbf{r}') & \rho \geq a \\ \bar{\mathbf{G}}_s^{(2)}(\mathbf{r},\mathbf{r}') & \rho \leq a \end{cases} \qquad (4.A5)$$

Here the source is at location $\mathbf{r}'$ and $\mathbf{r}$ is the position at which the field is calculated. The DGF in free space is defined as (73):

$$\bar{\mathbf{G}}_o(\mathbf{r},\mathbf{r}') = ik_0 \sum_{l=0}^{+\infty}\sum_{m=-l}^{+l} \begin{cases} \tilde{\mathbf{M}}_{l,m}^{+}(k_0,\mathbf{r})\tilde{\mathbf{M}}_{l,m}(k_0,\mathbf{r}') + \tilde{\mathbf{N}}_{l,m}^{+}(k_0,\mathbf{r})\tilde{\mathbf{N}}_{l,m}(k_0,\mathbf{r}') & \mathbf{r} \geq \mathbf{r}' \\ \tilde{\mathbf{M}}_{l,m}(k_0,\mathbf{r})\tilde{\mathbf{M}}_{l,m}^{+}(k_0,\mathbf{r}') + \tilde{\mathbf{N}}_{l,m}(k_0,\mathbf{r})\tilde{\mathbf{N}}_{l,m}^{+}(k_0,\mathbf{r}') & \mathbf{r} \leq \mathbf{r}' \end{cases} \qquad (4.A6)$$

where the ~ means that the vector wave functions in Eq. (4.2) are normalized by $-i\sqrt{l(l+1)}$ and the superscript $^+$ indicates that $h_l^{(1)}$, the spherical Hankel function of the first kind of order l, is used in place of the j_l's in Eq. (4.A2). The scattering components of the DGF are defined as (73):

$$\begin{aligned}\bar{\mathbf{G}}_s^{(1)}(\mathbf{r},\mathbf{r}') &= ik_0\sum_{l=0}^{+\infty}\sum_{m=-l}^{+l}\left[A_l\tilde{\mathbf{M}}_{l,m}^{+}(k_0,\mathbf{r})\tilde{\mathbf{M}}_{l,m}^{+}(k_0,\mathbf{r}')+B_l\tilde{\mathbf{N}}_{l,m}^{+}(k_0,\mathbf{r})\tilde{\mathbf{N}}_{l,m}^{+}(k_0,\mathbf{r}')\right]\\ \bar{\mathbf{G}}_s^{(2)}(\mathbf{r},\mathbf{r}') &= ik_0\sum_{l=0}^{+\infty}\sum_{m=-l}^{+l}\left[C_l\tilde{\mathbf{M}}_{l,m}(k_{\text{in}},\mathbf{r})\tilde{\mathbf{M}}_{l,m}^{+}(k_0,\mathbf{r}')+D_l\tilde{\mathbf{N}}_{l,m}(k_{\text{in}},\mathbf{r})\tilde{\mathbf{N}}_{l,m}^{+}(k_0,\mathbf{r}')\right]\end{aligned} \tag{4.A7}$$

where the coefficients A_l, B_l, C_l and D_l are determined applying the Dirichlet boundary conditions:

$$\begin{aligned}\hat{\rho}\times\bar{\mathbf{G}}(\rho=a+) &= \hat{\rho}\times\bar{\mathbf{G}}(\rho=a-)\\ \hat{\rho}\times\nabla\times\bar{\mathbf{G}}(\rho=a+) &= \hat{\rho}\times\nabla\times\bar{\mathbf{G}}(\rho=a-)\end{aligned} \tag{4.A8}$$

which yields:

$$\begin{pmatrix} -h_l^{(1)}(k_0a) & 0 & j_l(k_{\text{in}}a) & 0\\ 0 & -\left.\dfrac{\partial[\rho h_l^{(1)}(k_0\rho)]}{\partial\rho}\right|_{\rho=a} & 0 & \dfrac{k_0}{k_s}\left.\dfrac{\partial[\rho j_l(k_{\text{in}}\rho)]}{\partial\rho}\right|_{\rho=a}\\ -\left.\dfrac{\partial[\rho h_l^{(1)}(k_0\rho)]}{\partial\rho}\right|_{\rho=a} & 0 & \left.\dfrac{\partial[\rho j_l(k_{\text{in}}\rho)]}{\partial\rho}\right|_{\rho=a} & 0\\ 0 & -h_l^{(1)}(k_0a) & 0 & \dfrac{k_s}{k_0}j_l(k_{\text{in}}a)\end{pmatrix}\begin{pmatrix}A_l\\B_l\\C_l\\D_l\end{pmatrix} =$$

$$= \begin{pmatrix} j_l(k_0a)\\ \left.\dfrac{\partial[\rho j_l(k_0\rho)]}{\partial\rho}\right|_{\rho=a}\\ \left.\dfrac{\partial[\rho j_l(k_0\rho)]}{\partial\rho}\right|_{\rho=a}\\ j_l(k_0a)\end{pmatrix} \tag{4.A9}$$

Dyadic Green's functions for a dielectric cylinder in free space

In the case of a dielectric cylinder of radius a (Figure 4-2), the free-space DGF in Eq. (4.A5) can be defined as:

$$\bar{\mathbf{G}}_o(\mathbf{r},\mathbf{r}') = -\frac{j}{8\pi}\sum_{n=-\infty}^{+\infty}\int_{-\infty}^{+\infty}\frac{dm}{\eta^2}\begin{cases}\mathbf{A}_{n,\eta}(m,\mathbf{r})\tilde{\mathbf{M}}_{n,\eta}(m,\mathbf{r}')+\mathbf{B}_n(m,\mathbf{r})\tilde{\mathbf{N}}_{n,\eta}(m,\mathbf{r}') & \mathbf{r}\geq\mathbf{r}' \\ \tilde{\mathbf{M}}_{n,\eta}(m,\mathbf{r})\mathbf{A}_{n,\eta}(m,\mathbf{r}')+\tilde{\mathbf{N}}_{n,\eta}(m,\mathbf{r})\mathbf{B}_n(m,\mathbf{r}') & \mathbf{r}\leq\mathbf{r}'\end{cases} \quad (4.A10)$$

Here the vector wave functions $\tilde{\mathbf{M}}_{n,\eta}$ and $\tilde{\mathbf{N}}_{n,\eta}$ take the form of Eq. (4.9), with γ replaced by η (defined in Eq. (4.13)). The functions $\mathbf{A}_{n,\eta}$ and $\mathbf{B}_{n,\eta}$ are general linear combinations of wave functions and they are chosen to satisfy boundary conditions at the conductive shield ($\rho=\rho_s$), which requires the parallel components of the electric field to be zero:

$$\begin{aligned}\mathbf{A}_{n,\eta}(m,\mathbf{r}) &= \tilde{\mathbf{M}}^{+}_{n,\eta}(m,\mathbf{r})-\frac{H_n^{(2)'}(\eta,\rho_s)}{J_n'(\eta,\rho_s)}\tilde{\mathbf{M}}_{n,\eta}(m,\mathbf{r}) \\ \mathbf{B}_{n,\eta}(m,\mathbf{r}) &= \tilde{\mathbf{N}}^{+}_{n,\eta}(m,\mathbf{r})-\frac{H_n^{(2)'}(\eta,\rho_s)}{J_n'(\eta,\rho_s)}\tilde{\mathbf{N}}_{n,\eta}(m,\mathbf{r})\end{aligned} \quad (4.A11)$$

where $\tilde{\mathbf{M}}^{+}_{n,\eta}$ and $\tilde{\mathbf{N}}^{+}_{n,\eta}$ take precisely the same form as $\tilde{\mathbf{M}}_{n,\eta}$ and $\tilde{\mathbf{N}}_{n,\eta}$ with the additional substitutions $H_n^{(2)}\rightarrow J_n$ and $H_n^{(2)'}=\partial H_n^{(2)}/\partial\rho\rightarrow J_n'=\partial J_n/\partial\rho$, where $H_n^{(2)}$ is the Hankel function of the second kind of order n. Note also that, in order to ensure proper orthogonality behavior, the signs of all factors of in and im are reversed in the primed coordinate system as opposed to the unprimed coordinate system (e.g. $e^{in\varphi}e^{imz}\rightarrow e^{-in\varphi'}e^{-imz'}$). The remaining Green's functions representing "scattering" by the dielectric cylinder are defined as follows:

$$\bar{\mathbf{G}}_s^{(1)}(\mathbf{r},\mathbf{r}') = -\frac{j}{8\pi}\sum_{n=-\infty}^{+\infty}\int_{-\infty}^{+\infty}\frac{dm}{\eta^2}\begin{Bmatrix}\left[a_n(m)\mathbf{A}_{n,\eta}(m,\mathbf{r})+b_n(m)\mathbf{B}_{n,\eta}(m,\mathbf{r})\right]\mathbf{A}_{n,\eta}(m,\mathbf{r}') \\ +\left[c_n(m)\mathbf{A}_{n,\eta}(m,\mathbf{r})+d_n(m)\mathbf{B}_{n,\eta}(m,\mathbf{r})\right]\mathbf{B}_{n,\eta}(m,\mathbf{r}')\end{Bmatrix}$$

(4.A12)

$$\bar{\mathbf{G}}_s^{(2)}(\mathbf{r},\mathbf{r}') = -\frac{j}{8\pi}\sum_{n=-\infty}^{+\infty}\int_{-\infty}^{+\infty}\frac{dm}{\eta^2}\begin{Bmatrix}\left[e_n(m)\tilde{\mathbf{M}}_{\gamma,n}(m,\mathbf{r})+f_n(m)\tilde{\mathbf{N}}_{\gamma,n}(m,\mathbf{r})\right]\mathbf{A}_{n,\eta}(m,\mathbf{r}') \\ +\left[g_n(m)\tilde{\mathbf{M}}_{\gamma,n}(m,\mathbf{r})+h_n(m)\tilde{\mathbf{N}}_{\gamma,n}(m,\mathbf{r})\right]\mathbf{B}_{n,\eta}(m,\mathbf{r}')\end{Bmatrix}$$

(4.A13)

where the index γ is defined as $\gamma^2=k_{\text{in}}^2-m^2$ with k_{in}^2 as in Eq. (4.A4). The values of the coefficients *a*, *b*, *c*, *d*, *e*, *f*, *g*, and *h* were fixed by applying the boundary conditions in Eq. (4.A8) on electric and magnetic fields at the surface of the cylinder. For the left

hand side of these equations we used $\bar{\mathbf{G}}(\rho=a+)=\left(\bar{\mathbf{G}}_0(\mathbf{r},\mathbf{r}')+\bar{\mathbf{G}}_s^{(1)}(\mathbf{r},\mathbf{r}')\right)\Big|_{\rho=a}$ and chose the lower branch of $\bar{\mathbf{G}}_0$ in Eq. (4.A10) with $\mathbf{A}_{n,\eta}$ and $\mathbf{B}_{n,\eta}$ in the prime coordinate system (since the integral in Eq (4.1) is non-vanishing only at $\rho' = \rho_c > a = \rho$). For the left hand side we used $\bar{\mathbf{G}}(\rho=a-)=\bar{\mathbf{G}}_s^{(1)}(\mathbf{r},\mathbf{r}')\Big|_{\rho=a}$. Since all vector wave functions with distinct mode indices are orthogonal, we can impose the boundary conditions separately for each value of n and m, yielding the following matrix expressions for the coefficients:

$$\mathbf{Q}\cdot\begin{bmatrix} a_n(m) \\ b_n(m) \\ e_n(m) \\ f_n(m) \end{bmatrix} = \begin{bmatrix} \eta J_n'(\eta a) \\ 0 \\ \chi J_n(\eta a) \\ -\eta^2 J_n(\eta a) \end{bmatrix} \qquad \mathbf{Q}\cdot\begin{bmatrix} c_n(m) \\ d_n(m) \\ g_n(m) \\ h_n(m) \end{bmatrix} = \begin{bmatrix} \frac{\chi}{k_0} J_n(\eta a) \\ \frac{-\eta^2}{k_0} J_n(\eta a) \\ k_0 \eta J_n'(\eta a) \\ 0 \end{bmatrix} \quad (4.A14)$$

with $\chi \equiv {}^{nm}\!/_{a}$ and:

$$\mathbf{Q} = \begin{bmatrix} -\eta\Pi'(\eta a) & \frac{-\chi}{k_0}\Pi(\eta a) & \gamma J_n'(\gamma a) & \frac{\chi}{k_{in}} J_n(\gamma a) \\ 0 & \frac{\eta^2}{k_0}\Pi(\eta a) & 0 & \frac{-\gamma^2}{k_{in}} J_n(\gamma a) \\ -\chi\Xi'(\eta a) & -k_0\eta\Xi'(\eta a) & \chi J_n(\gamma a) & k\gamma J_{nn}'(\gamma a) \\ \eta^2\Xi(\eta a) & 0 & -\gamma^2 J_n(\gamma a) & 0 \end{bmatrix} \quad (4.A15)$$

where:

$$\begin{aligned} \Pi(\eta a) &\equiv H_n^{(2)}(\eta a) - \frac{H_n^{(2)}(\eta,\rho_s)}{J_n(\eta,\rho_s)} J_n(\eta a) \\ \Pi'(\eta a) &\equiv H_n^{(2)'}(\eta a) - \frac{H_n^{(2)'}(\eta,\rho_s)}{J_n'(\eta,\rho_s)} J_n'(\eta a) \\ \Xi(\eta a) &\equiv H_n^{(2)}(\eta a) - \frac{H_n^{(2)'}(\eta,\rho_s)}{J_n'(\eta,\rho_s)} J_n(\eta a) \\ \Xi'(\eta a) &\equiv H_n^{(2)'}(\eta a) - \frac{H_n^{(2)}(\eta,\rho_s)}{J_n(\eta,\rho_s)} J_n'(\eta a) \end{aligned} \quad (4.A16)$$

Appendix B

Mode expansion of the electromagnetic field inside dielectric sphere

Let us define a basis set of current patterns on the surface of the sphere, including both magnetic-type and electric-type components, indicated with the superscript $^{(M)}$ and $^{(E)}$ respectively:

$$\begin{aligned}\mathbf{J}(\theta,\varphi) &= \sum_{l=0}^{+\infty}\sum_{m=-l}^{+l}\left[\mathbf{K}_{l,m}^{(M)}(\theta,\varphi)+\mathbf{K}_{l,m}^{(E)}(\theta,\varphi)\right] \\ &= \sum_{l=0}^{+\infty}\sum_{m=-l}^{+l}-i\sqrt{l(l+1)}\left[W_{l,m}^{(M)}\mathbf{X}_{l,m}(\theta,\varphi)+W_{l,m}^{(E)}\rho\hat{\rho}\times\mathbf{X}_{l,m}(\theta,\varphi)\right]\end{aligned} \tag{4.B1}$$

In order to calculate the EM field inside the sphere, we need to choose the branch of the DGF with $\rho \le a$ and substitute in Eq. (4.1):

$$\begin{aligned}&\mathbf{E}(\mathbf{r}) = i\omega\mu_0\iiint_{V'}\bar{\mathbf{G}}(\mathbf{r},\mathbf{r}')\cdot\mathbf{J}(\mathbf{r}')dV' = i\omega\mu_0\iint_{A'}\bar{\mathbf{G}}_s^{(2)}(\mathbf{r},\mathbf{r}')\cdot\left[\mathbf{K}^{(M)}(\mathbf{r}')+\mathbf{K}^{(E)}(\mathbf{r}')\right]a^2dA' = \\ &i\omega\mu_0a^2\iint_{A'}\left\{-ik_0\sum_{l=0}^{+\infty}\sum_{m=-l}^{+l}\left[C_l\tilde{\mathbf{M}}_{l,m}(k_{\text{in}},\mathbf{r})\tilde{\mathbf{M}}_{l,m}^{+}(k_0,\mathbf{r}')+D_l\tilde{\mathbf{N}}_{l,m}(k_{\text{in}},\mathbf{r})\tilde{\mathbf{N}}_{l,m}^{+}(k_0,\mathbf{r}')\right]\right\}\cdot \\ &\left\{\sum_{l'=0}^{+\infty}\sum_{m=-l'}^{+l'}-i\sqrt{l'(l'+1)}\left[W_{l',m'}^{(M)}\mathbf{X}_{l',m'}(\theta',\varphi')+W_{l',m'}^{(E)}\rho\hat{\rho}\times\mathbf{X}_{l',m'}(\theta',\varphi')\right]\right\}dA'\end{aligned} \tag{4.B2}$$

Let us define:

$$\begin{aligned}V_{(l,m),(l'm')}^{M} &= C_l\iint_{A'}\left[\tilde{W}_{l',m'}^{(M)}\tilde{\mathbf{M}}_{l,m}^{+}(k_0,\mathbf{r}')\cdot\left(-i\sqrt{l'(l'+1)}\mathbf{X}_{l',m'}(\vartheta',\phi')\right)+\right. \\ &\left.\tilde{W}_{l',m'}^{(E)}\tilde{\mathbf{M}}_{l,m}^{+}(k_0,\mathbf{r}')\rho\hat{\rho}\times\left(-i\sqrt{l'(l'+1)}\mathbf{X}_{l',m'}(\vartheta',\phi')\right)\right]dA' \\ V_{(l,m),(l'm')}^{N} &= D_l\iint_{A'}\left[\tilde{W}_{l',m'}^{(M)}\tilde{\mathbf{N}}_{l,m}^{+}(k_0,\mathbf{r}')\cdot\left(-i\sqrt{l'(l'+1)}\mathbf{X}_{l',m'}(\vartheta',\phi')\right)+\right. \\ &\left.\tilde{W}_{l',m'}^{(E)}\tilde{\mathbf{N}}_{l,m}^{+}(k_0,\mathbf{r}')\rho\hat{\rho}\times\left(-i\sqrt{l'(l'+1)}\mathbf{X}_{l',m'}(\vartheta',\phi')\right)\right]dA'\end{aligned} \tag{4.B3}$$

Applying the orthogonality relations of the vector spherical harmonics (71) we can solve the integrals in Eq. (4.B3):

$$\begin{aligned}
&\iint_{A'}\tilde{\mathbf{M}}^{+}_{l,m}(k_0,\mathbf{r}')\cdot\left(-i\sqrt{l'(l'+1)}\mathbf{X}_{l',m'}(\vartheta',\phi')\right)dA' \\
&=-i\sqrt{l'(l'+1)}h_l^{(1)}(k_0a)\iint_{A'}\mathbf{X}_{l,m}(\vartheta',\phi')\cdot\mathbf{X}_{l',m'}(\vartheta',\phi')dA' \\
&=-i\sqrt{l(l+1)}h_l^{(1)}(k_0a)\delta_{l,l'}\delta_{m,m'}
\end{aligned} \tag{4.B4}$$

$$\begin{aligned}
&\iint_{A'}\tilde{\mathbf{M}}^{+}_{l,m}(k_0,\mathbf{r}')\cdot\left[\rho\hat{\rho}\times\left(-i\sqrt{l'(l'+1)}\mathbf{X}_{l',m'}(\vartheta',\phi')\right)\right]dA' \\
&=-i\sqrt{l'(l'+1)}h_l^{(1)}(k_0a)\iint_{A'}\mathbf{X}_{l,m}(\vartheta',\phi')\cdot\left(\rho\hat{\rho}\times\mathbf{X}_{l',m'}(\vartheta',\phi')\right)dA'=0
\end{aligned} \tag{4.B5}$$

$$\begin{aligned}
&\iint_{A'}\tilde{\mathbf{N}}^{+}_{l,m}(k_0,\mathbf{r}')\cdot\left(-i\sqrt{l'(l'+1)}\mathbf{X}_{l',m'}(\vartheta',\phi')\right)dA'= \\
&=-i\sqrt{l'(l'+1)}\iint_{A'}\frac{1}{k_0a}\left.\frac{\partial[\rho h_l^{(1)}(k_0\rho)]}{\partial\rho}\right|_{\rho=a}\left(\hat{\rho}\times\mathbf{X}_{l,m}(\vartheta',\phi')\right)\cdot\mathbf{X}_{l',m'}(\vartheta',\phi')dA'+ \\
&\quad -i\sqrt{l'(l'+1)}\sqrt{l(l+1)}\iint_{A'}\frac{h_l^{(1)}(k_0a)}{k_0a}\mathrm{Y}_l^m(\vartheta',\phi')\hat{\rho}\cdot\mathbf{X}_{l',m'}(\vartheta',\phi')dA'=0
\end{aligned} \tag{4.B6}$$

$$\begin{aligned}
&\iint_{A'}\tilde{\mathbf{N}}^{+}_{l,m}(k_0,\mathbf{r}')\cdot\left[\rho\hat{\rho}\times\left(-i\sqrt{l'(l'+1)}\mathbf{X}_{l',m'}(\vartheta',\phi')\right)\right]dA'= \\
&-i\sqrt{l'(l'+1)}\iint_{A'}\frac{1}{k_0a}\left.\frac{\partial[\rho h_l^{(1)}(k_0\rho)]}{\partial\rho}\right|_{\rho=a}\left(\hat{\rho}\times\mathbf{X}_{l,m}(\vartheta',\phi')\right)\cdot\left(\rho\hat{\rho}\times\mathbf{X}_{l',m'}(\vartheta',\phi')\right)dA'+ \\
&-i\sqrt{l'(l'+1)}\sqrt{l(l+1)}\iint_{A'}\frac{h_l^{(1)}(k_0a)}{k_0a}\mathrm{Y}_l^m(\vartheta',\phi')\hat{\rho}\cdot\left(\rho\hat{\rho}\times\mathbf{X}_{l',m'}(\vartheta',\phi')\right)dA'= \\
&\frac{-i\sqrt{l(l+1)}}{k_0a}\left.\frac{\partial[\rho h_l^{(1)}(k_0\rho)]}{\partial\rho}\right|_{\rho=a}\delta_{l,l'}\delta_{m,m'}
\end{aligned} \tag{4.B7}$$

We can now re-write Eq. (4.B3) with a more compact notation:

$$\mathbf{V}=\begin{pmatrix}V^M_{l,m}\\V^N_{l,m}\end{pmatrix}=\begin{pmatrix}-i\sqrt{l(l+1)}h_l^{(1)}(k_0a)C_l & 0\\ 0 & \left.\dfrac{-i\sqrt{l(l+1)}}{k_0a}\dfrac{\partial[\rho h_l^{(1)}(k_0\rho)]}{\partial\rho}\right|_{\rho=a}D_l\end{pmatrix}\cdot\begin{pmatrix}\tilde{W}^{(M)}_{l,m}\\ \tilde{W}^{(E)}_{l,m}\end{pmatrix}=\mathbf{T}^{\mathrm{T}}\cdot\mathbf{W} \tag{4.B8}$$

Substituting in the expression of the electric field, we find:

$$\mathbf{E}(\mathbf{r})=\omega\mu_0k_0a^2\sum_{l=0}^{+\infty}\sum_{m=-l}^{+l}\left[\tilde{\mathbf{M}}_{l,m}(k_{\mathrm{in}},\mathbf{r})V^M_{l,m}+\tilde{\mathbf{N}}_{l,m}(k_{\mathrm{in}},\mathbf{r})V^N_{l,m}\right] \tag{4.B9}$$

An expression for the magnetic field can be easily derived using Maxwell's equations and the symmetrical relations in Eq. (4.A3):

$$\mathcal{B}(\mathbf{r}) = \frac{i}{\omega}\nabla\times\mathcal{E}(\mathbf{r}) = i\mu_0 k_0 k_{\text{in}} a^2 \sum_{l=0}^{+\infty}\sum_{m=-l}^{+l}\left[\tilde{\mathbf{N}}_{l,m}(k_{\text{in}},\mathbf{r})V_{l,m}^{M} + \tilde{\mathbf{M}}_{l,m}(k_{\text{in}},\mathbf{r})V_{l,m}^{N}\right] \qquad (4.B10)$$

For the calculation of the SNR and the SAR per unit flip angle, electric and magnetic field can be arbitrarily scaled by the same quantity. In order to match the equations of the noise covariance matrix and the sensitivity matrix reported in Ref. (42) for ultimate intrinsic SNR, we divided Eq. (4.B9) and (4.B10) by $k_0 k_{\text{in}} a^2$, obtaining the expressions in Eq. (4.6).

Mode expansion of the electromagnetic field inside the dielectric cylinder

The EM field inside a dielectric cylinder can be calculated similarly and yield the same general expression as in Ref. (110):

$$\begin{aligned}\mathcal{E}(\mathbf{r}) &= -\frac{\omega\mu_0}{8\pi}\sum_{n=-\infty}^{+\infty}\int_{-\infty}^{+\infty}\left[\tilde{\mathbf{M}}_{n,\gamma}(m,\mathbf{r})V_n^{M}(m) + \tilde{\mathbf{N}}_{n,\gamma}(m,\mathbf{r})V_n^{N}(m)\right]dm \\ \mathcal{B}(\mathbf{r}) &= -\frac{ik_{\text{in}}\mu_0}{8\pi}\sum_{n=-\infty}^{+\infty}\int_{-\infty}^{+\infty}\left[\tilde{\mathbf{N}}_{n,\gamma}(m,\mathbf{r})V_n^{M}(m) + \tilde{\mathbf{M}}_{n,\gamma}(m,\mathbf{r})V_n^{N}(m)\right]dm\end{aligned} \qquad (4.B11)$$

As in Eq. (4.B8), $V_n^{M}(m)$ and $V_n^{N}(m)$ are defined as the product of a transformation matrix $\mathbf{T}$ with the expansion weights. The matrix $\mathbf{T}$ is different from Ref. (110), as it accounts for the presence of the conductive shield :

$$\mathbf{T}^{\mathrm{T}} = -j\frac{4\pi^2\rho_c}{\eta^2}\left\{\begin{array}{l} H_n^{(2)'}(\eta\rho_c) - \dfrac{H_n^{(2)'}(\eta,\rho_s)}{J_n'(\eta,\rho_s)}\begin{bmatrix} e_n(m) \\ f_n(m)\end{bmatrix}\begin{bmatrix}\eta m & \eta n/b\end{bmatrix} \\ +H_n^{(2)'}(\eta\rho_c) - \dfrac{H_n^{(2)}(\eta,\rho_s)}{J_n(\eta,\rho_s)}\begin{bmatrix} g_n(m) \\ h_n(m)\end{bmatrix}\begin{bmatrix} nk_0/b & (m/k_0)\left((n/b)^2-\eta^2\right)\end{bmatrix}\end{array}\right\} \qquad (4.B12)$$

Mode expansion of the electromagnetic field at the conductive shield

The EM field at the conductive shield (i.e. for $\rho=\rho_s$, outside the cylinder) can be calculated with $\bar{\mathbf{G}}_o(\mathbf{r},\mathbf{r}') + \bar{\mathbf{G}}_s^{(1)}(\mathbf{r},\mathbf{r}')$, choosing the upper branch of $\bar{\mathbf{G}}_o(\mathbf{r},\mathbf{r}')$ in Eq.

(4.A10) as we are in the case $\rho' < \rho = \rho_s$. Substituting in Eq. (4.1), with the current distribution defined in Eq. (4.8), yields Eq. (4.12), where the matrix **U** is defined as:

$$\begin{aligned}\begin{pmatrix} V_n^A(m) \\ V_n^B(m) \end{pmatrix} &= -j\frac{4\pi^2\rho_c}{\eta^2}\left\{\left(J_n'(\eta\rho_c)\begin{bmatrix}1\\0\end{bmatrix}+\Pi'(\eta\rho_c)\begin{bmatrix}a_n(m)\\b_n(m)\end{bmatrix}\right)\begin{bmatrix}\eta m & \eta n/b\end{bmatrix}\right. \\ &\left.+\left(J_n(\eta\rho_c)\begin{bmatrix}0\\1\end{bmatrix}+\Pi(\eta\rho_c)\begin{bmatrix}c_n(m)\\d_n(m)\end{bmatrix}\right)\begin{bmatrix}nk_0/\rho_c & (m/k_0)\left((n/\rho_c)^2-\eta^2\right)\end{bmatrix}\right\}\begin{pmatrix} W_n^{(M)}(m) \\ W_n^{(E)}(m)\end{pmatrix} \\ &\equiv \mathbf{U}^{\mathrm{T}}\begin{pmatrix} W_n^{(M)}(m) \\ W_n^{(E)}(m)\end{pmatrix}\end{aligned}$$

(4.B13)

The coefficients *a*, *b*, *c*, *d*, *e*, *f*, *g*, *h* are given in Eq. (4.A14) and Π, Π' are given in Eq. (4.A16).

Appendix C

Calculation of signal sensitivity and noise power for the dielectric sphere

The principle of reciprocity (70) allows calculating the receive sensitivity of a coil in terms of the RF magnetic field that would be transmitted at the same position by a unit current flowing around the coil. An expression of the sensitivity matrix is derived in Eq. (4.16) as a function of the matrix **S**:

$$\mathbf{S} = \begin{pmatrix}\mathbf{S}^{(M)} \\ \mathbf{S}^{(E)}\end{pmatrix} = i\mu_0\begin{pmatrix}\tilde{\mathbf{N}}_{\mathrm{x}}(k_{\mathrm{in}},\mathbf{r}) - i\tilde{\mathbf{N}}_{\mathrm{y}}(k_{\mathrm{in}},\mathbf{r}) \\ \tilde{\mathbf{M}}_{\mathrm{x}}(k_{\mathrm{in}},\mathbf{r}) - i\tilde{\mathbf{M}}_{\mathrm{y}}(k_{\mathrm{in}},\mathbf{r})\end{pmatrix} \tag{4.C1}$$

where, from Eq. (4.2):

$$\begin{aligned}\tilde{\mathbf{N}}_{\mathrm{x}}(k_{\mathrm{in}},\mathbf{r}) &= \frac{1}{k_{\mathrm{in}}}\left[\nabla\times j_l(k_{\mathrm{in}}\rho)\mathbf{X}_{l,m}(\theta,\varphi)\right]_{\mathrm{x}} \\ &= -\frac{i}{k_{\mathrm{in}}\rho}\frac{\partial[\rho j_l(k_{\mathrm{in}}\rho)]}{\partial\rho}\left[\hat{\rho}\times\mathbf{X}_{l,m}(\vartheta,\phi)\right]_{\mathrm{x}} + \sqrt{l(l+1)}\frac{j_l(k_{\mathrm{in}}\rho)}{\rho}\mathrm{Y}_l^m(\vartheta,\phi)\left[\hat{\rho}\right]_{\mathrm{x}} \\ \tilde{\mathbf{M}}_{\mathrm{x}}(k_{\mathrm{in}},\mathbf{r}) &= j_l(k_{\mathrm{in}}\rho)\left[\mathbf{X}_{l,m}(\theta,\varphi)\right]_{\mathrm{x}}\end{aligned} \tag{4.C2}$$

$\tilde{\mathbf{N}}_y$ and $\tilde{\mathbf{M}}_y$ are defined analogously, using the y-components. Note that Eq. (4.C2) is identical to Eq. B8 in Ref. (42), derived with a different mode expansion of the EM field.

The power loss in Eq. (4.17), due to thermal noise in the sample with conductivity σ, was derived integrating electric field products over the volume of the sphere:

$$\begin{aligned}\tilde{\mathbf{P}}_L &= \frac{\sigma}{2}\iiint_V \mathbf{E}(\mathbf{r})\cdot\mathbf{E}^*(\mathbf{r})dV \\ &= \frac{\sigma}{2}\left|\frac{\omega\mu_0}{k_{\text{in}}}\right|^2 \iiint_V \sum_{l=0}^{+\infty}\sum_{m=-l}^{+l}\sum_{l'=0}^{+\infty}\sum_{m'=-l'}^{+l'} \left(V_{l,m}^M V_{l,m}^N\right)\begin{pmatrix}\tilde{\mathbf{M}}_{l,m}\\ \tilde{\mathbf{N}}_{l,m}\end{pmatrix}\left(\tilde{\mathbf{M}}_{l',m'}^* \tilde{\mathbf{N}}_{l',m'}^*\right)\begin{pmatrix}V_{l',m'}^M\\ V_{l',m'}^N\end{pmatrix}^* dV\end{aligned} \tag{4.C3}$$

The four integrals can be solved using the orthogonality relations of the vector spherical harmonics (71):

$$\begin{aligned}\iiint_V \tilde{\mathbf{M}}_{l,m}\cdot\tilde{\mathbf{M}}_{l',m'}^* dV &= \iiint_V j_l(k_{\text{in}}\rho)j_{l'}^*(k_{\text{in}}\rho)\mathbf{X}_{l,m}(\vartheta,\phi)\cdot\mathbf{X}_{l',m'}^*(\vartheta,\phi)dV = \\ &= \delta_{l,l'}\delta_{m,m'}\int_0^a \left|j_l(k_{\text{in}}\rho)\right|^2\rho^2 d\rho\end{aligned} \tag{4.C4}$$

$$\begin{aligned}\iiint_V \tilde{\mathbf{N}}_{l,m}\cdot\tilde{\mathbf{N}}_{l',m'}^* dV &= \frac{1}{|k_s|^2}\left\{\iiint_V \frac{1}{\rho^2}\frac{\partial[\rho j_l(k_{\text{in}}\rho)]}{\partial\rho}\frac{\partial[\rho j_{l'}^*(k_{\text{in}}\rho)]}{\partial\rho}\left(\hat{\rho}\times\mathbf{X}_{l,m}(\vartheta,\phi)\right)\cdot\right. \\ &\left.\left(\hat{\rho}\times\mathbf{X}_{l',m'}^*(\vartheta,\phi)\right)dV + l(l+1)\iiint_V \frac{1}{\rho^2}j_l(k_{\text{in}}\rho)j_{l'}^*(k_{\text{in}}\rho)\mathbf{Y}_l^m(\vartheta,\phi)\hat{\rho}\cdot\mathbf{Y}_{l'}^{m'}(\vartheta,\phi)^*\hat{\rho}dV\right\} \\ &= \delta_{l,l'}\delta_{m,m'}\frac{1}{|k_{\text{in}}|^2}\left\{\int_0^a\left[\left|\frac{\partial[\rho j_l(k_{\text{in}}\rho)]}{\partial\rho}\right|^2 + l(l+1)\left|j_l(k_{\text{in}}\rho)\right|^2\right]d\rho\right\}\end{aligned}$$

(4.C5)

$$\iiint_V \tilde{\mathbf{M}}_{l,m}\cdot\tilde{\mathbf{N}}_{l',m'}^* dV = \iiint_V \tilde{\mathbf{N}}_{l,m}\cdot\tilde{\mathbf{M}}_{l',m'}^* dV = 0 \tag{4.C6}$$

Eq. (4.C3) can be re-written as:

$$\tilde{\mathbf{P}}_L = \frac{\sigma}{2}\left|\frac{\omega\mu_0}{k_{\text{in}}}\right|^2 \sum_{l=0}^{+\infty}\sum_{m=-l}^{+l} \mathbf{V}^{\mathrm{T}} \begin{pmatrix} \int_0^a \left|j_l(k_{\text{in}}\rho)\right|^2 \rho^2 d\rho & 0 \\ 0 & \frac{1}{|k_s|^2}\left\{\int_0^a \left[\left|\frac{\partial[\rho j_l(k_{\text{in}}\rho)]}{\partial\rho}\right|^2 + l(l+1)\left|j_l(k_{\text{in}}\rho)\right|^2\right] d\rho\right\} \end{pmatrix} \mathbf{V}^*$$

$$= \sum_{l=0}^{+\infty}\sum_{m=-l}^{+l} \mathbf{V}^{\mathrm{T}} \mathbf{P}_L \mathbf{V}^*$$

(4.C7)

Note that $\mathbf{P}_L$ coincides with the noise matrix derived by Wiesinger at al. using the multipole expansion for the EM field in the sphere (42). The two expressions exactly match if we multiply Eq. [B7] of Ref. (42) by the conductivity of the sample, to correct for a minor typographical error and by 1/2 to account for a different definition of the RMS noise voltage in the SNR equation.

The current distribution on the surface A', at radial distance ρ_c, causes a power loss inversely proportional to the conductivity (σ_c) and thickness (d_c) of the coil material:

$$\begin{aligned} \mathrm{P}_A &= \frac{1}{2\sigma_c d_c}\iint_{A'} \mathbf{K}(\mathbf{r}')\cdot\mathbf{K}^*(\mathbf{r}')dA' \\ &= \frac{1}{2\sigma_c d_c}\iint_{A'} \sum_{l=0}^{+\infty}\sum_{m=-l}^{+l}\sum_{l'=0}^{+\infty}\sum_{m'=-l'}^{+l'} \left(W_{l,m}^{(M)} W_{l,m}^{(E)}\right)\begin{pmatrix}\mathbf{K}_{lm}^{(M)} \\ \mathbf{K}_{lm}^{(E)}\end{pmatrix}\left(\mathbf{K}_{l'm'}^{*(M)} \mathbf{K}_{l'm'}^{*(E)}\right)\begin{pmatrix}W_{l',m'}^{(M)} \\ W_{l',m'}^{(E)}\end{pmatrix}^* dA' \end{aligned} \tag{4.C8}$$

As for Eq. (4.C3), also in this case we can apply the orthogonality relations of the vector spherical harmonics (71) to solve the equation:

$$\begin{aligned} \iint_{A'} \mathbf{K}_{l,m}^{(M)}\cdot\mathbf{K}_{l',m'}^{(M)} dA' &= \sqrt{l(l+1)}\sqrt{l'(l'+1)}\iint_{A'} \mathbf{X}_{l,m}(\vartheta,\phi)\cdot\mathbf{X}_{l',m'}^*(\vartheta,\phi)dA' \\ &= \rho_c^2\delta_{l,l'}\delta_{m,m'}l(l+1) \end{aligned} \tag{4.C9}$$

$$\begin{aligned} \iint_{A'} \mathbf{K}_{l,m}^{(E)}\cdot\mathbf{K}_{l',m'}^{*(E)} dA' &= \sqrt{l(l+1)}\sqrt{l'(l'+1)}\iint_{A'} \left(\rho\hat{\rho}\times\mathbf{X}_{l,m}(\vartheta,\phi)\right)\cdot\left(\rho\hat{\rho}\times\mathbf{X}_{l',m'}^*(\vartheta,\phi)\right)dA' \\ &= \rho_c^2\delta_{l,l'}\delta_{m,m'}l(l+1) \end{aligned} \tag{4.C10}$$

$$\iint_{A'} \mathbf{K}_{l,m}^{(M)}\cdot\mathbf{K}_{l',m'}^{*(E)} dA' = \iint_{A'} \mathbf{K}_{l,m}^{(E)}\cdot\mathbf{K}_{l',m'}^{*(M)} dA' = 0 \tag{4.C11}$$

Substituting in Eq. (4.C8) yields:

$$\mathbf{P}_A = \sum_{l=0}^{+\infty}\sum_{m=-l}^{+l} \mathbf{W}^{\mathrm{T}} \frac{l(l+1)\rho_c^2}{2\sigma_c d_c}\begin{pmatrix}1 & 0\\ 0 & 1\end{pmatrix}\mathbf{W}^{*} = \sum_{l=0}^{+\infty}\sum_{m=-l}^{+l} \mathbf{W}^{\mathrm{T}}\mathbf{P}_A\mathbf{W}^{*} \tag{4.C12}$$

Calculation of signal sensitivity and noise power for the dielectric cylinder

The sensitivity matrix in the case of the cylinder is calculated as:

$$\begin{aligned}
\mathcal{B}_{\mathrm{x}}(\mathbf{r}_0) - i\mathcal{B}_{\mathrm{y}}(\mathbf{r}_0) &= -i\frac{\mu_0 k_{\mathrm{in}}}{8\pi}\sum_{n=-\infty}^{\infty}\int_{-\infty}^{\infty}\left\{\tilde{\mathbf{N}}_{\gamma,n}(m,\mathbf{r})V_n^M(m) + \tilde{\mathbf{M}}_{\gamma,n}(m,\mathbf{r})V_n^N(m)\right\}\cdot\left(\hat{x} - i\hat{y}\right)dm \\
&= -ie^{-i\varphi}\frac{\mu_0 k}{8\pi}\sum_{n=-\infty}^{\infty}\int_{-\infty}^{\infty}\left\{\tilde{\mathbf{N}}_{\gamma,n}(m,\mathbf{r})V_n^M(m) + \tilde{\mathbf{M}}_{\gamma,n}(m,\mathbf{r})V_n^N(m)\right\}\cdot\left(\hat{\rho} - i\hat{\varphi}\right)dm \\
&= -ie^{-i\varphi}\frac{\mu_0 k}{8\pi}\sum_{n=-\infty}^{\infty}\int_{-\infty}^{\infty}\left(\gamma J_n'(\gamma\rho) + \frac{n}{\rho}J_n(\gamma\rho)\right)\left\{i\frac{m}{k}V_n^M(m) + iV_n^N(m)\right\}e^{in\varphi}e^{imz}dm \\
&= \frac{\mu_0}{8\pi}\sum_{n=-\infty}^{\infty}\int_{-\infty}^{\infty}\left(\gamma J_n'(\gamma\rho) + \frac{n}{\rho}J_n(\gamma\rho)\right)\left\{mV_n^M(m) + kV_n^N(m)\right\}e^{i(n-1)\varphi}e^{imz}dm \\
&= \sum_{n=-\infty}^{\infty}\int_{-\infty}^{\infty}\left[V_n^M(m) \quad V_n^N(m)\right]\left(\frac{\mu_0\gamma J_{n-1}(\gamma\rho)e^{i(n-1)\varphi}e^{imz}}{8\pi}\begin{bmatrix}m\\ k\end{bmatrix}\right)dm \\
&= \sum_{n=-\infty}^{\infty}\int_{-\infty}^{\infty}\mathbf{V}^{\mathrm{T}}\mathbf{S}dm = \sum_{n=-\infty}^{\infty}\int_{-\infty}^{\infty}\mathbf{W}^{\mathrm{T}}\mathbf{T}\mathbf{S}dm
\end{aligned} \tag{4.C13}$$

where the unit vectors were transformed in cylindrical coordinates using:

$$\hat{x} - i\hat{y} = e^{-i\varphi}\left(\hat{\rho} - i\hat{\varphi}\right) \tag{4.C14}$$

and the following properties of Bessel functions were used:

$$\begin{aligned}
J_n'(\gamma\rho) &= \frac{1}{2}\left(J_{n-1}(\gamma\rho) - J_{n+1}(\gamma\rho)\right) \\
J_n(\gamma\rho) &= \frac{\gamma\rho}{2n}\left(J_{n-1}(\gamma\rho) + J_{n+1}(\gamma\rho)\right)
\end{aligned} \tag{4.C15}$$

Eq. (4.C13) is equivalent to Eq. (4.16) with:

$$\mathbf{S} = \begin{pmatrix}\mathbf{S}^{(M)}\\ \mathbf{S}^{(E)}\end{pmatrix} = \frac{\mu_0\gamma J_{n-1}(\gamma\rho)e^{i(n-1)\varphi}e^{imz}}{8\pi}\begin{pmatrix}m\\ k\end{pmatrix} \tag{4.C16}$$

This expressions differs from the corresponding expression in (110) in several ways. First, n-1 substituted for n+1. Second, the sign of term $mV_n^M(m)$ in Eq. (4.C13) is reversed. Third, full φ and z dependencies included, as required for parallel imaging which relies upon phase as well as amplitude differences in sensitivities at aliased positions.

The power loss due to thermal noise in the sample is derived in Ref. (110) and reported in Eq. (4.19). The power loss due to the fact that currents circulate in lossy coil conductors is calculated as:

$$\tilde{\mathbf{P}}_A = \frac{1}{2\sigma_c d_c}\iint_{A'}\mathbf{K}(\mathbf{r}')\cdot\mathbf{K}^*(\mathbf{r}')dA'$$

$$= \frac{1}{2\sigma_c d_c}\iint_{A'}dA'\left\{\int_{-\infty}^{+\infty}\int_{-\infty}^{+\infty}\sum_{n=-\infty}^{+\infty}\sum_{n'=-\infty}^{+\infty}\mathbf{W}_n^{\mathrm{T}}(m)\begin{pmatrix}\nabla\times e^{in\varphi}e^{imz}\hat{\rho}\\ \nabla e^{in\varphi}e^{imz}\end{pmatrix}\left(\nabla\times e^{-in'\varphi}e^{-im'z}\hat{\rho}\;\nabla e^{-in'\varphi}e^{-im'z}\right)\mathbf{W}_{n'}^*(m')\right\} \quad \text{(4.C17)}$$

The four integral can be solved separately in cylindrical coordinates with $dA' = \rho_c d\varphi dz$:

$$\int_{-\infty}^{+\infty}\int_{-\infty}^{+\infty}\sum_{n=-\infty}^{+\infty}\sum_{n'=-\infty}^{+\infty}\left\{\iint_{A'}\left(\nabla\times e^{in\varphi}e^{imz}\hat{\rho}\right)\cdot\left(\nabla\times e^{-in'\varphi}e^{-im'z}\hat{\rho}\right)dA'\right\}$$

$$= \int_{-\infty}^{+\infty}\int_{-\infty}^{+\infty}\sum_{n=-\infty}^{+\infty}\sum_{n'=-\infty}^{+\infty}\left\{\iint_{A'}e^{i(n-n')\varphi}e^{i(m-m')z}\left(m^2+\frac{n^2}{\rho_c^2}\right)dA'\right\} \quad \text{(4.C18)}$$

$$= 4\pi^2\rho_c\delta_{nn'}\delta(m-m')\left(m^2+\frac{n^2}{\rho_c^2}\right)$$

$$\int_{-\infty}^{+\infty}\int_{-\infty}^{+\infty}\sum_{n=-\infty}^{+\infty}\sum_{n'=-\infty}^{+\infty}\left\{\iint_{A'}\left(\nabla e^{in\varphi}e^{imz}\right)\cdot\left(\nabla e^{-in'\varphi}e^{-im'z}\right)dA'\right\}$$

$$= \int_{-\infty}^{+\infty}\int_{-\infty}^{+\infty}\sum_{n=-\infty}^{+\infty}\sum_{n'=-\infty}^{+\infty}\left\{\iint_{A'}e^{i(n-n')\varphi}e^{i(m-m')z}\left(m^2+\frac{n^2}{\rho_c^2}\right)dA'\right\} \quad \text{(4.C19)}$$

$$= 4\pi^2\rho_c\delta_{nn'}\delta(m-m')\left(m^2+\frac{n^2}{\rho_c^2}\right)$$

$$\int_{-\infty}^{+\infty}\int_{-\infty}^{+\infty}\sum_{n=-\infty}^{+\infty}\sum_{n'=-\infty}^{+\infty}\left\{\iint_{A'}\left(\nabla\times e^{in\varphi}e^{imz}\hat{\rho}\right)\cdot\left(\nabla e^{-in'\varphi}e^{-im'z}\right)dA'\right\} = 0 \quad \text{(4.C20)}$$

$$\int_{-\infty}^{+\infty}\int_{-\infty}^{+\infty}\sum_{n=-\infty}^{+\infty}\sum_{n'=-\infty}^{+\infty}\left\{\iint_{A'}\left(\nabla e^{in\varphi}e^{imz}\right)\cdot\left(\nabla\times e^{-in'\varphi}e^{-im'z}\hat{\rho}\right)dA'\right\}=0 \tag{4.C21}$$

We can now re-write Eq. (4.C17) as:

$$\begin{aligned}\tilde{\mathbf{P}}_A &= \frac{1}{2\sigma_c d_c}\int_{-\infty}^{+\infty}\sum_{n=-\infty}^{+\infty}\mathbf{W}_n^{\mathrm{T}}(m)\left\{4\pi^2\rho_c\begin{pmatrix} m^2+\dfrac{n^2}{\rho_c^2} & 0 \\ 0 & m^2+\dfrac{n^2}{\rho_c^2}\end{pmatrix}\right\}\mathbf{W}_n^{*}(m) \\ &= \int_{-\infty}^{+\infty}\sum_{n=-\infty}^{+\infty}\mathbf{W}_n^{\mathrm{T}}(m)\mathbf{P}_A\mathbf{W}_n^{*}(m)\end{aligned} \tag{4.C22}$$

with $\mathbf{P}_A$ defined in Eq. (4.23). In the case of the cylinder we modeled an additional power loss due to the induced currents circulating in the conductive shield. This current distribution $\mathbf{K}_S$ is given by:

$$\begin{aligned}\mathbf{K}_S(\mathbf{r}) &= \frac{1}{\mu_0}\mathcal{B}_{\mathrm{out}}(\mathbf{r})\big|_{\rho=\rho_s}\times\hat{\rho} \\ &= -\frac{ik_0}{8\pi}\sum_{n=-\infty}^{+\infty}\int_{-\infty}^{+\infty}\left\{\begin{bmatrix}0\\ \dfrac{\eta^2}{k_0}(H-J)\\ \dfrac{nm}{\rho_s k_0}(H-J)\end{bmatrix}V_n^A(m)+\begin{bmatrix}0\\0\\ \eta(H-J)'\end{bmatrix}V_n^B(m)\right\}e^{in\varphi}e^{imz}dm \\ &= -\frac{ik_0}{8\pi}\sum_{n=-\infty}^{+\infty}\int_{-\infty}^{+\infty}\left\{\begin{bmatrix}0\\ \eta^2\\ \dfrac{nm}{\rho_s}\end{bmatrix}(H-J)V_n^A(m)+\begin{bmatrix}0\\0\\ k_0\eta\end{bmatrix}(H-J)'V_n^B(m)\right\}e^{in\varphi}e^{imz}dm\end{aligned} \tag{4.C23}$$

where:

$$(H-J)=H_n^{(2)}(\eta\rho_s)-\frac{H_n^{(2)'}(\eta,\rho_s)}{J_n'(\eta,\rho_s)}J_n(\eta,\rho_s)$$
$$(H-J)'=H_n^{(2)'}(\eta\rho_s)-\frac{H_n^{(2)}(\eta,\rho_s)}{J_n(\eta,\rho_s)}J_n'(\eta,\rho_s) \tag{4.C24}$$

The corresponding power loss, assuming the conductivity and the thickness of the shield material are σ_S and d_S, respectively, for a shield of length L_S is calculated as:

$$\begin{aligned}\tilde{\mathbf{P}}_S &= \frac{1}{2\sigma_S d_S}\iint_{A'}\mathbf{K}_S(\mathbf{r}')\cdot\mathbf{K}_S^*(\mathbf{r}')dA' = \frac{1}{2\sigma_S d_S}\int_0^{2\pi}\int_{-\infty}^{+\infty}\mathbf{K}_S(\mathbf{r}')\cdot\mathbf{K}_S^*(\mathbf{r}')\rho_S d\varphi dz \\ &= \sum_{n=-\infty}^{+\infty}\int_{-\infty}^{+\infty}\left[V_n^A(m)V_n^B(m)\right]\mathbf{P}_S\begin{bmatrix}V_n^A(m)\\ V_n^B(m)\end{bmatrix}dm\end{aligned} \tag{4.C25}$$

with:

$$\mathbf{P}_S=\frac{\rho_S L_S}{32\sigma_S d_S}D\begin{pmatrix}\left|\eta^2+\frac{nm}{\rho_s}\right|^2 & \frac{nmk_0\eta^*}{\rho_s}\\ \frac{nmk_0\eta}{\rho_s} & |k_0\eta|^2\end{pmatrix}D^{T*} \tag{4.C26}$$

where we have defined D in terms of the quantities in Eq. (4.C24):

$$D=\begin{pmatrix}(H-J) & 0\\ 0 & (H-J)'\end{pmatrix} \tag{4.C27}$$

Appendix D

Calculation of the weighting coefficients for a loop coil along the z-axis

In order to calculate the weights that must be applied to the basis current distribution for the case of a loop coil perpendicular to the z-axis (Figure 4-1), we start by re-writing Eq. (4.38) as:

$$\mathbf{K}(\theta,\varphi)=\sum_{l=0}^{+\infty}\sum_{m=-l}^{+l}W_{l,m}^{(M)}\left(+im\csc\theta\mathrm{Y}_l^m(\theta,\varphi)\hat{\theta}\right.$$
$$\left.-\left[l\cot\theta\mathrm{Y}_l^m(\theta,\varphi)-\csc\theta\sqrt{\frac{2l+1}{2l-1}(l^2-m^2)}\mathrm{Y}_{l-1}^m(\theta,\varphi)\right]\hat{\varphi}\right) \quad (4.D1)$$

This expression must be equivalent to Eq. (4.37), so the θ component must be zero for every l, which means that m = 0 always. We can now compare the simplified Eq. (4.D1) with Eq. (4.37):

$$\sum_{l=0}^{+\infty}W_{l,0}^{(M)}\left[-i\sqrt{l(l+1)}\mathbf{X}_{l,0}(\theta,\varphi)\right]=I\frac{\sin\theta}{\sqrt{d^2+R^2}}\delta\left(\cos\theta-\frac{d}{\sqrt{d^2+R^2}}\right)\hat{\varphi}. \quad (4.D2)$$

Let us multiply both sides by $i\sqrt{l'(l'+1)}\mathbf{X}_{l',0}^*(\theta,\varphi)$ and take the surface integral:

$$\sum_{l=0}^{+\infty}W_{l,0}^{(M)}\sqrt{l(l+1)}\sqrt{l'(l'+1)}\int_0^{\pi}\int_0^{2\pi}\mathbf{X}_{l,0}(\theta,\varphi)\mathbf{X}_{l',0}^*(\theta,\varphi)\left(d^2+R^2\right)\sin\theta d\theta d\varphi$$
$$=\frac{I}{\sqrt{d^2+R^2}}\int_0^{\pi}\int_0^{2\pi}\delta\left(\cos\theta-\frac{d}{\sqrt{d^2+R^2}}\right)\hat{\varphi}\cdot\sqrt{l'(l'+1)}\mathbf{X}_{l',0}^*(\theta,\varphi)\left(d^2+R^2\right)\sin^2\theta d\theta d\varphi$$
(4.D3)

The integral on left-hand side can be solved applying the orthogonality properties of the vector spherical harmonics (71), whereas the solution for the right-hand side can be found integrating by variable substitution. Extracting the $W_{l,0}^{(M)}$ yields the expression in Eq. (4.39).

Calculation of the weighting coefficients for a loop coil rotated away from the z-axis

A loop coil arbitrarily rotated on the surface of the sphere (Figure 4-1) can be seen as a loop coil along the z-axis of a rotated coordinate system (see Eq. (4.40)). The

coordinate rotation which brings the unit vectors and coordinates of the unprimed system into the primed system is defined as follows:

$$\mathbf{R}(\alpha,\beta,0)\begin{Bmatrix}\mathbf{e}_x\\ \mathbf{e}_y\\ \mathbf{e}_z\end{Bmatrix}=\begin{Bmatrix}\mathbf{e}_{x'}\\ \mathbf{e}_{y'}\\ \mathbf{e}_{z'}\end{Bmatrix},\quad \mathbf{R}(\alpha,\beta,0)\begin{Bmatrix}x\\ y\\ z\end{Bmatrix}=\begin{Bmatrix}x'\\ y'\\ z'\end{Bmatrix} \tag{4.D4}$$

The axis of the rotated coil is parallel to $\mathbf{e}_{z'}$, and α and β define the angular position of the center of the rotated coil on the unit sphere. We may set $\gamma=0$ due to the symmetry of the circular loop. We must now express Eq. (4.40) in terms of the original reference coordinate system:

$$\mathbf{X}'_{l,0}(\theta',\varphi')=\frac{-i}{\sqrt{l(l+1)}}\left(\mathbf{r}'\times\nabla'\right)Y_l^0(\theta',\varphi') \tag{4.D5}$$

We may express the cross product in the rotated reference frame in terms of Levi-Civita symbols as follows:

$$\mathbf{r}'\times\nabla'=\begin{vmatrix}\mathbf{e}_{x'} & \mathbf{e}_{y'} & \mathbf{e}_{z'}\\ x' & y' & z'\\ \dfrac{\partial}{\partial x'} & \dfrac{\partial}{\partial y'} & \dfrac{\partial}{\partial z'}\end{vmatrix}=\sum_{ijk}\varepsilon_{ijk}\mathbf{e}_{x'_i}x'_j\frac{\partial}{\partial x'_k} \tag{4.D6}$$

Transforming each term in the sum into the unrotated coordinate frame, we have:

$$\begin{aligned}\mathbf{e}_{x'_i}&=\sum_p\mathbf{R}_{ip}(\alpha,\beta,0)\mathbf{e}_{x_p}\\ x'_j&=\sum_q\mathbf{R}_{jq}(\alpha,\beta,0)x_q\\ \frac{\partial}{\partial x'_k}&=\sum_r\frac{\partial x_r}{\partial x'_k}\frac{\partial}{\partial x_r}=\sum_r\frac{\partial}{\partial x'_k}\left(\sum_s\mathbf{R}^{-1}_{rs}(\alpha,\beta,0)x'_s\right)\frac{\partial}{\partial x_r}\\ &=\sum_r\mathbf{R}^{-1}_{rk}(\alpha,\beta,0)\frac{\partial}{\partial x_r}=\sum_r\mathbf{R}_{kr}(\alpha,\beta,0)\frac{\partial}{\partial x_r}\end{aligned} \tag{4.D7}$$

Therefore,

$$\mathbf{r}'\times\nabla' = \sum_{ijkpqr} \varepsilon_{ijk}\mathbf{R}_{ip}(\alpha,\beta,0)\mathbf{R}_{jq}(\alpha,\beta,0)\mathbf{R}_{kr}(\alpha,\beta,0)\mathbf{e}_{x_p}x_q\frac{\partial}{\partial x_r} \qquad (4.D8)$$

This sum has a total of 162 terms (6 non-vanishing permutations of ε_{ijk} times the 33 terms of the p, q, r sums). However, a large number of these terms vanish by symmetry. For example, all terms with p=q, p=r, or q=r reverse sign on exchange of i, j, or k with multiplication by ε_{ijk}, resulting in cancellation. Similarly, $p\leftrightarrow q$, $p\leftrightarrow r$, or $q\leftrightarrow r$ result in sign changes. In short, we may write:

$$\mathbf{r}'\times\nabla' = \sum_{pqr}\left(\sum_{ijk}\varepsilon_{ijk}\mathbf{R}_{ip}(\alpha,\beta,0)\mathbf{R}_{jq}(\alpha,\beta,0)\mathbf{R}_{kr}(\alpha,\beta,0)\right)\varepsilon_{pqr}\mathbf{e}_{x_p}x_q\frac{\partial}{\partial x_r} \qquad (4.D9)$$

Now, for the combinations of p, q, and r which result in non-vanishing ε_{pqr}, the i, j, k sum in Eq. (4.D9) may be identified with the determinant of the rotation matrix $|\mathbf{R}(\alpha,\beta,0)|$ and proper orthogonal matrices (i.e. rotations) such as this must have unit determinant:

$$\sum_{ijk}\varepsilon_{ijk}\mathbf{R}_{ip}(\alpha,\beta,0)\mathbf{R}_{jq}(\alpha,\beta,0)\mathbf{R}_{kr}(\alpha,\beta,0) = |\mathbf{R}(\alpha,\beta,0)| = 1 \qquad (4.D10)$$

Therefore:

$$\mathbf{r}'\times\nabla' = \sum_{ijk}\varepsilon_{ijk}\mathbf{e}_{x_i'}x_j'\frac{\partial}{\partial x_k'} = \sum_{pqr}\varepsilon_{pqr}\mathbf{e}_{x_p}x_q\frac{\partial}{\partial x_r} = \mathbf{r}\times\nabla \qquad (4.D11)$$

Spherical harmonics in a rotated coordinate system can be expressed in terms of the unrotated reference frame (114):

$$\begin{aligned} Y_l^0(\theta',\varphi') &= Y_l^0\left(\mathbf{R}(\alpha,\beta,0)(\theta,\varphi)\right) = \sum_{m=-l}^{l} D_{m,0}^{l}(\alpha,\beta,0)Y_l^m(\theta,\varphi) \\ &= \sqrt{\frac{4\pi}{2l+1}}\sum_{m=-l}^{l} Y_l^{m*}(\beta,\alpha)Y_l^m(\theta,\varphi) \end{aligned} \qquad (4.D12)$$

Substituting Eq. (4.D11) and (4.D12) in Eq. (4.D5), from Eq. (4.40) we obtain the weights for the rotated loop coil in Eq. (4.43).

Calculation of the weighting coefficients for cylindrical window coils

Current density distribution for an ideal cylindrical window coil (Figure 4-2) centered at $\varphi = 0$ and $z = 0$ with angular aperture $2\varphi_0$ and axial length 2d carrying current I on each leg is:

$$\mathbf{K}^{window}(\varphi, z) = I \begin{Bmatrix} \big(\delta(z+d) - \delta(z-d)\big)\big(\theta(\varphi-\varphi_0) - \theta(\varphi+\varphi_0)\big)\hat{\varphi} \\ +\frac{1}{b}\big(\delta(\varphi-\varphi_0) - \delta(\varphi+\varphi_0)\big)\big(\theta(z-d) - \theta(z+d)\big)\hat{z} \end{Bmatrix} \quad (4.D13)$$

Here $\theta(\varphi - \varphi_0)$ is the step function with a positive step from 0 to 1 at $\varphi = \varphi_0$. The factor of 1/b in the z component arises from the requirement of uniform current around the loop:

$$\int \mathbf{J}^{\text{window}} \cdot \left(\rho d\varphi d\rho \hat{z}\right) = b \int \mathbf{K}^{\text{window}} \cdot \hat{z} d\varphi = I = \int \mathbf{K}^{\text{window}} \cdot \hat{\varphi} dz = \int \mathbf{J}^{\text{window}} \cdot \left(dz d\rho \hat{\varphi}\right).$$

(4.D14)

Using the Fourier transformation properties of the delta function and the step function, we have:

$$\begin{aligned} \mathbf{K}^{\text{window}}(\varphi, z) &= I \sum_{n=-\infty}^{\infty} \int_{-\infty}^{\infty} \begin{Bmatrix} \frac{\sin(n\varphi_0)}{n} e^{in\varphi}\left(e^{imd} - e^{-imd}\right)e^{imz}\hat{\varphi} \\ +\frac{1}{b}\left(e^{-in\varphi_0} - e^{in\varphi_0}\right)e^{in\varphi}\frac{\sin(md)}{m}e^{imz}\hat{z} \end{Bmatrix} dm \\ &= \sum_{n=-\infty}^{\infty} \int_{-\infty}^{\infty} \left(2I\frac{\sin(n\varphi_0)}{n}\frac{\sin(md)}{m}\right) e^{in\varphi}e^{imz}\left\{im\hat{\varphi} - \frac{in}{b}\hat{z}\right\} dm \end{aligned} \quad (4.D15)$$

This expression must be equivalent to the magnetic-dipole component of the current distribution in Eq. (4.8) for $\rho = b$:

$$\mathbf{K}(\varphi, z) = \sum_{n=-\infty}^{+\infty} \int_{-\infty}^{+\infty} W_n^{(M)}(m) \nabla \times e^{in\varphi} e^{imz} \hat{\rho} dm = \sum_{n=-\infty}^{+\infty} \int_{-\infty}^{+\infty} W_n^{(M)}(m) \left\{im\hat{\varphi} - \frac{in}{b}\hat{z}\right\} e^{in\varphi} e^{imz} dm$$

(4.D16)

Comparing the last two equations we find an expression for the weighting coefficients:

$$W_n^{window,(M)}(m) = 2I \frac{\sin(n\varphi_0)}{n} \frac{\sin(md)}{m} \quad (4.D17)$$

The effects of translation or rotation of the coil on the cylindrical surface (i.e. moving the coil center to $\varphi = \Delta\varphi_\gamma$ and $z = \Delta z_\gamma$, where γ is the coil index) may be accounted for by taking $\varphi \to \varphi - \Delta\varphi_\gamma$ and $z \to z - \Delta z_\gamma$ in the preceding derivation, resulting in the general expression of Eq. (4.45) for the current mode weights of a cylindrical window coil arbitrarily positioned on the cylindrical surface.

Chapter 5

General Conclusions and Future Work

5.1 Conclusions

The performance of RF coil arrays will shape the future of MRI. The benefits of high field MRI can be fully exploited only with the implementation of parallel imaging and parallel transmission techniques, which depend heavily upon the quality of the coils used. As the operating frequency of and the number of available channels for MR systems increases, coil engineers will be presented with new design challenges and the role of computer simulations will become ever more important to avoid construction of expensive prototypes. The performance of any coil array is strictly constrained by the behavior of electromagnetic fields within the sample, but the knowledge of such limitations can be exploited to improve existing coil designs and to develop novel transmitters, or receivers, that operate close to the optimum performance.

In this dissertation we studied the performance of RF coil arrays, both in MR reception and in MR transmission. We developed a comprehensive theoretical framework which allows calculation of ultimate intrinsic SNR and SAR in the case of spherical and cylindrical samples. We showed that both maximum SNR and minimum SAR can be approached with a finite number of coils, if ideal current patterns resulting in the best possible performance are used as a target for coil design. We proposed a method to evaluate the absolute performance of a coil, using ultimate intrinsic SNR as a

reference. Our method provides useful information for coil engineers, as a supplement to or perhaps an eventual replacement for the common practice of comparing coils among each other to assess their quality. It was found that at high magnetic field strengths, due to shortening of the RF wavelength, parallel transmission become very effective in reducing SAR while simultaneously maintaining the homogeneity of the excitation. This work provides new insights on the potential uses of coil arrays, and it can serve as a guide for future implementations.

5.2 Future research directions

In this work we described for the first time ideal current patterns associated with optimal SNR and SAR performance. These ideal patterns provide physical insight about desirable coil behavior, but the questions "What is the best transmitter?" and "What is the best receiver?" are only partially answered. In parallel imaging and parallel transmission, ideal current patterns are optimized at each voxel position and each time period, respectively. Although this may be sufficient to maximize the performance for particular applications, future research work will focus on searching for composite current patterns that bring the overall performance of a coil close to the optimum for a range of applications. A possible approach would be to parameterize design specifications and employ genetic algorithms to find the optimal combination. However, before investing resources in that direction, it will be important to validate experimentally the results of the simulations. As it is easier to measure SNR than SAR, the first tests should be aimed at proving the practical utility of ideal current patterns in the receive case. We saw in chapter 4 that, for particular voxel locations, these patterns have circular shape and are localized in small areas, so it would be instructive to see how much of the ultimate SNR can be achieved if we build loop coils that replicate the optimal current distribution.

It will be also important to verify the generality of the results presented in this thesis when heterogeneous samples are used. One way of doing that is to replicate some of the calculations of optimal SNR done for the case of few-element arrays, modeling exactly the same coil geometries with, say, FDTD techniques and using realistic tissue

models. Another possibility is to model previously derived ideal current patterns as conductor distributions in finite element or FDTD methods, to see if the general trends in SNR and SAR we observe in homogeneous samples are confirmed in the case of heterogeneous samples.

One early application of ideal current patterns for improved coil design would be for the case of RF shimming. In RF shimming all coils share a common pulse waveform, and therefore there is a single configuration of the optimal current distribution that we need to reproduce. Furthermore, in RF shimming achievable excitations are dictated strongly by coil design (as opposed to the case of fully parallel transmission, which has a larger number of degrees of freedom), and therefore RF shimming represents an appealing starting point for optimization.

Though Cartesian k-space trajectories were used in this thesis for the study of both reception and excitation behavior, our semi analytical simulation framework can be extended in a straightforward manner to accommodate arbitrary k-space trajectories. This would be particularly useful in the case of transmission, as Cartesian EPI trajectories are not routinely used for parallel excitation due to their long duration. EPI trajectories were used in this thesis because they simplify the implementation of accelerated parallel excitations and they are a convenient choice for the study of SAR behavior as a function of acceleration.

Shortening of the RF pulse duration in parallel excitation is compensated by use of higher current amplitudes and therefore larger amounts of RF energy are expected to be transferred to the patient during accelerated excitations. Despite this, our results show that at high frequencies the growth of ultimate SAR with respect to the degree of acceleration flattens out. This result suggests similarities to the improvements in geometry factor observed at high field for parallel reception. In the transmit case as well as in the receive case, the shortening of wavelength may improve the performance for accelerated tasks. It will be interesting to verify this hypothesis in the case of finite coil configurations, both in simulations and experimentally.

It is our hope that in this work we have begun to address some of the questions facing modern designers and users of RF coil arrays in MRI. These basic questions will undoubtedly continue to motivate multifaceted work in times to come, and we look forward to the answers which may emerge.

References

1. Lauterbur PC. Image formation by induced local interactions: examples employing nuclear magnetic resonance. Nature 1973;242:190-191.
2. Mansfield P. Multi-planar image formation using NMR spin echoes. J Phys C: Solid State Phys 1977;10:L55-L58.
3. Mansfield P, Maudsley AA. Medical imaging by NMR. Br J Radiol 1977;50(591):188-194.
4. Lauterbur PC. Progress in n.m.r. zeugmatography imaging. Philos Trans R Soc Lond B Biol Sci 1980;289(1037):483-487.
5. Christoforidis GA, Bourekas EC, Baujan M, Abduljalil AM, Kangarlu A, Spigos DG, Chakeres DW, Robitaille PM. High resolution MRI of the deep brain vascular anatomy at 8 Tesla: susceptibility-based enhancement of the venous structures. J Comput Assist Tomogr 1999;23(6):857-866.
6. Robitaille PM, Abduljalil AM, Kangarlu A. Ultra high resolution imaging of the human head at 8 tesla: 2K x 2K for Y2K. J Comput Assist Tomogr 2000;24(1):2-8.
7. Novak V, Abduljalil A, Kangarlu A, Slivka A, Bourekas E, Novak P, Chakeres D, Robitaille PM. Intracranial ossifications and microangiopathy at 8 Tesla MRI. Magn Reson Imaging 2001;19(8):1133-1137.
8. Yacoub E, Shmuel A, Pfeuffer J, Van De Moortele PF, Adriany G, Andersen P, Vaughan JT, Merkle H, Ugurbil K, Hu X. Imaging brain function in humans at 7 Tesla. Magn Reson Med 2001;45(4):588-594.
9. Golman K, in 't Zandt R, Thaning M. Real-time metabolic imaging. Proc Natl Acad Sci U S A 2006;103(30):11270-11275. Epub 12006 Jul 11212.
10. Kim D, Chun BG, Kim YK, Lee YH, Park CS, Jeon I, Cheong C, Hwang TS, Chung H, Gwag BJ, Hong KS, Song J. In vivo tracking of human mesenchymal stem cells in experimental stroke. Cell Transplant 2008;16(10):1007-1012.

11. Sun JH, Teng GJ, Ju SH, Ma ZL, Mai XL, Ma M. MR tracking of magnetically labeled mesenchymal stem cells in rat kidneys with acute renal failure. Cell Transplant 2008;17(3):279-290.

12. Kauczor H, Surkau R, Roberts T. MRI using hyperpolarized noble gases. Eur Radiol 1998;8(5):820-827.

13. Bhattacharya P, Harris K, Lin AP, Mansson M, Norton VA, Perman WH, Weitekamp DP, Ross BD. Ultra-fast three dimensional imaging of hyperpolarized 13C in vivo. Magma 2005;18(5):245-256. Epub 2005 Nov 2023.

14. Roemer PB, Edelstein WA, Hayes CE, Souza SP, Mueller OM. The NMR phased array. Magn Reson Med 1990;16(2):192-225.

15. Sodickson DK, Manning WJ. Simultaneous acquisition of spatial harmonics (SMASH): fast imaging with radiofrequency coil arrays. Magn Reson Med 1997;38(4):591-603.

16. Pruessmann KP, Weiger M, Scheidegger MB, Boesiger P. SENSE: sensitivity encoding for fast MRI. Magn Reson Med 1999;42(5):952-962.

17. Griswold MA, Jakob PM, Heidemann RM, Nittka M, Jellus V, Wang J, Kiefer B, Haase A. Generalized autocalibrating partially parallel acquisitions (GRAPPA). Magn Reson Med 2002;47(6):1202-1210.

18. van der Meulen P, Groen JP, Cuppen JJ. Very fast MR imaging by field echoes and small angle excitation. Magn Reson Imaging 1985;3(3):297-299.

19. Frahm J, Haase A, Matthaei D. Rapid NMR imaging of dynamic processes using the FLASH technique. Magn Reson Med 1986;3(2):321-327.

20. Hennig J, Nauerth A, Friedburg H. RARE imaging: a fast imaging method for clinical MR. Magn Reson Med 1986;3(6):823-833.

21. Carlson JW. An algorithm for NMR imaging reconstruction based on multiple RF receiver coils. J Magn Reson 1987;74:376-380.

22. Hutchinson M, Raff U. Fast MRI data acquisition using multiple detectors. Magn Reson Med 1988;6(1):87-91.

23. Kwiat D, Einav S, Navon G. A decoupled coil detector array for fast image acquisition in magnetic resonance imaging. Med Phys 1991;18(2):251-265.

24. Carlson JW, Minemura T. Imaging time reduction through multiple receiver coil data acquisition and image reconstruction. Magn Reson Med 1993;29(5):681-687.

25. Ra JB, Rim CY. Fast imaging using subencoding data sets from multiple detectors. Magn Reson Med 1993;30(1):142-145.

26. Sodickson DK, McKenzie CA. A generalized approach to parallel magnetic resonance imaging. Med Phys 2001;28(8):1629-1643.

27. Sodickson DK. Tailored SMASH image reconstructions for robust in vivo parallel MR imaging. Magn Reson Med 2000;44(2):243-251.

28. McKenzie CA, Ohliger MA, Yeh EN, Price MD, Sodickson DK. Coil-by-coil image reconstruction with SMASH. Magn Reson Med 2001;46(3):619-623.

29. Griswold MA, Jakob PM, Nittka M, Goldfarb JW, Haase A. Partially parallel imaging with localized sensitivities (PILS). Magn Reson Med 2000;44(4):602-609.

30. Kyriakos WE, Panych LP, Kacher DF, Westin CF, Bao SM, Mulkern RV, Jolesz FA. Sensitivity profiles from an array of coils for encoding and reconstruction in parallel (SPACE RIP). Magn Reson Med 2000;44(2):301-308.

31. Lee RF, Westgate CR, Weiss RG, Bottomley PA. An analytical SMASH procedure (ASP) for sensitivity-encoded MRI. Magn Reson Med 2000;43(5):716-725.

32. Bydder M, Larkman DJ, Hajnal JV. Generalized SMASH imaging. Magn Reson Med 2002;47(1):160-170.

33. Yeh EN, McKenzie CA, Ohliger MA, Sodickson DK. Parallel magnetic resonance imaging with adaptive radius in k-space (PARS): constrained image reconstruction using k-space locality in radiofrequency coil encoded data. Magn Reson Med 2005;53(6):1383-1392.

34. Sodickson DK, McKenzie CA, Li W, Wolff S, Manning WJ, Edelman RR. Contrast-enhanced 3D MR angiography with simultaneous acquisition of spatial harmonics: A pilot study. Radiology 2000;217(1):284-289.

35. Golay X, Brown SJ, Itoh R, Melhem ER. Time-resolved contrast-enhanced carotid MR angiography using sensitivity encoding (SENSE). AJNR Am J Neuroradiol 2001;22(8):1615-1619.

36. Ohno Y, Kawamitsu H, Higashino T, Takenaka D, Watanabe H, van Cauteren M, Fujii M, Hatabu H, Sugimura K. Time-resolved contrast-enhanced pulmonary MR angiography using sensitivity encoding (SENSE). J Magn Reson Imaging 2003;17(3):330-336.

37. Plein S, Radjenovic A, Ridgway JP, Barmby D, Greenwood JP, Ball SG, Sivananthan MU. Coronary artery disease: myocardial perfusion MR imaging with sensitivity encoding versus conventional angiography. Radiology 2005;235(2):423-430.

38. Weiger M, Pruessmann KP, Boesiger P. Cardiac real-time imaging using SENSE. SENSitivity Encoding scheme. Magn Reson Med 2000;43(2):177-184.

39. McKenzie CA, Lim D, Ransil BJ, Morrin M, Pedrosa I, Yeh EN, Sodickson DK, Rofsky NM. Shortening MR image acquisition time for volumetric interpolated breath-hold examination with a recently developed parallel imaging reconstruction technique: clinical feasibility. Radiology 2004;230(2):589-594. Epub 2003 Dec 2029.

40. Vogt FM, Antoch G, Hunold P, Maderwald S, Ladd ME, Debatin JF, Ruehm SG. Parallel acquisition techniques for accelerated volumetric interpolated breath-hold examination magnetic resonance imaging of the upper abdomen: assessment of image quality and lesion conspicuity. J Magn Reson Imaging 2005;21(4):376-382.

41. Ohliger MA, Grant AK, Sodickson DK. Ultimate intrinsic signal-to-noise ratio for parallel MRI: electromagnetic field considerations. Magn Reson Med 2003;50(5):1018-1030.

42. Wiesinger F, Boesiger P, Pruessmann KP. Electrodynamics and ultimate SNR in parallel MR imaging. Magn Reson Med 2004;52(2):376-390.

43. Zhu Y, Hardy CJ, Sodickson DK, Giaquinto RO, Dumoulin CL, Kenwood G, Niendorf T, Lejay H, McKenzie CA, Ohliger MA, Rofsky NM. Highly parallel volumetric imaging with a 32-element RF coil array. Magn Reson Med 2004;52(4):869-877.

44. Warner R, Pittard S, Feenan PJ, Goldi F, Abduljalil AM, Robitaille PM. Design and manufacture of the world's first whole body MRI magnet operating at field strength above 7.0 tesla: initial findings. Proceedings of the International society magnetic resonance in medicine. 1998. p 254.

45. Hoult DI, Richards RE. The Signal-to-Noise ratio of the nuclear magnetic resonance experiment. Journal of Magnetic Resonance 1976;24:71-85.

46. Barfuss H, Fischer H, Hentschel D, Ladebeck R, Vetter J. Whole-body MR imaging and spectroscopy with a 4-T system. Radiology 1988;169(3):811-816.

47. Bomsdorf H, Helzel T, Kunz D, Roschmann P, Tschendel O, Wieland J. Spectroscopy and imaging with a 4 tesla whole-body MR system. NMR Biomed 1988;1(3):151-158.

48. Barfuss H, Fischer H, Hentschel D, Ladebeck R, Oppelt A, Wittig R, Duerr W, Oppelt R. In vivo magnetic resonance imaging and spectroscopy of humans with a 4 T whole-body magnet. NMR Biomed 1990;3(1):31-45.

49. Bomsdorf H, Roschmann P, Wieland J. Sensitivity enhancement in whole-body natural abundance 13C spectroscopy using 13C/1H double-resonance techniques at 4 tesla. Magn Reson Med 1991;22(1):10-22.

50. Vaughan JT, Hetherington HP, Otu JO, Pan JW, Pohost GM. High frequency volume coils for clinical NMR imaging and spectroscopy. Magn Reson Med 1994;32(2):206-218.

51. Ogawa S, Tank DW, Menon R, Ellermann JM, Kim SG, Merkle H, Ugurbil K. Intrinsic signal changes accompanying sensory stimulation: functional brain mapping with magnetic resonance imaging. Proc Natl Acad Sci U S A 1992;89(13):5951-5955.

52. Robitaille PM, Warner R, Jagadeesh J, Abduljalil AM, Kangarlu A, Burgess RE, Yu Y, Yang L, Zhu H, Jiang Z, Bailey RE, Chung W, Somawiharja Y,

Feynan P, Rayner DL. Design and assembly of an 8 tesla whole-body MR scanner. J Comput Assist Tomogr 1999;23(6):808-820.

53. Atkinson IC, Renteria L, Burd H, Pliskin NH, Thulborn KR. Safety of human MRI at static fields above the FDA 8 T guideline: sodium imaging at 9.4 T does not affect vital signs or cognitive ability. J Magn Reson Imaging 2007;26(5):1222-1227.

54. Neurospin. http://www-dsv.cea.fr/neurospin/.

55. Hoult DI, Phil D. Sensitivity and power deposition in a high-field imaging experiment. J Magn Reson Imaging 2000;12(1):46-67.

56. Vaughan JT; The General Hospital Corporation, assignee. RF coil for imaging system patent 6,633,161. 2003.

57. Vaughan JT, Adriany G, Snyder CJ, Tian J, Thiel T, Bolinger L, Liu H, DelaBarre L, Ugurbil K. Efficient high-frequency body coil for high-field MRI. Magn Reson Med 2004;52(4):851-859.

58. Katscher U, Bornert P, Leussler C, van den Brink JS. Transmit SENSE. Magn Reson Med 2003;49(1):144-150.

59. Zhu Y. Parallel excitation with an array of transmit coils. Magn Reson Med 2004;51(4):775-784.

60. Wiesinger F, De Zanche N, Pruessmann KP. Approaching ultimate SNR with finite coil arrays. Proceedings of the 13th Annual Meeting ISMRM, Miami Beach, USA. 2005; p 672.

61. Wiggins GC, Potthast A, Triantafyllou C, Lin F, Benner T, Wiggins CJ, Wald L. A 96-channel MRI system with 23- and 90-channel phase array head coils at 1.5 Tesla. Proceedings of the 13th Annual Meeting ISMRM, Miami Beach, USA. 2005; p 671.

62. Schmitt M, Potthast A, Sosnovik DE, Polimeni JR, Wiggins GC, Triantafyllou C, Wald LL. A 128-channel receive-only cardiac coil for highly accelerated cardiac MRI at 3 Tesla. Magn Reson Med 2008;59(6):1431-1439.

63. Katscher U, Rohrs J, Bornert P. Basic considerations on the impact of the coil array on the performance of Transmit SENSE. Magma 2005;18(2):81-88. Epub 2005 Feb 2011.

64. Zhu Y. RF power deposition and "g-factor" in parallel transmit. Proceedings of the 14th Annual Meeting ISMRM, Seattle, USA. 2006; p 599.

65. Weiger M, Pruessmann KP, Leussler C, Roschmann P, Boesiger P. Specific coil design for SENSE: a six-element cardiac array. Magn Reson Med 2001;45(3):495-504.

66. de Zwart JA, Ledden PJ, Kellman P, van Gelderen P, Duyn JH. Design of a SENSE-optimized high-sensitivity MRI receive coil for brain imaging. Magn Reson Med 2002;47(6):1218-1227.

67. Ocali O, Atalar E. Ultimate intrinsic signal-to-noise ratio in MRI. Magn Reson Med 1998;39(3):462-473.

68. Lattanzi R, Grant AK, Ohliger MA, Sodickson DK. Measuring practical coil array performance with respect to ultimate intrinsic SNR: a tool for array design and assessment. Proceedings of the 14th Annual Meeting ISMRM, Seattle, USA. 2006; p 424.

69. Edelstein WA, Bottomley PA, Pfeifer LM. A signal-to-noise calibration procedure for NMR imaging systems. Med Phys 1984;11(2):180-185.

70. Hoult DI. The principle of reciprocity in signal strength calculations - a mathematical guide. Concepts in Magnetic Resonance 2000;12(4):173-187.

71. Jackson JD. Classical Electrodynamics: John Wiley & Sons; 1999.

72. Hayes CE, Roemer PB. Noise correlations in data simultaneously acquired from multiple surface coil arrays. Magn Reson Med 1990;16(2):181-191.

73. Tai CT. Dyadic Green Functions in Electromagnetic Theory: Institute of Electrical & Electronics Engineers; 1994.

74. Lattanzi R, Sodickson DK. Dyadic Green's functions for electrodynamic calculations of ideal current patterns for optimal SNR and SAR. Proceedings of the 16th Annual Meeting ISMRM, Toronto, Canada. 2008; p 78.

75. Wiggins GC, Triantafyllou C, Potthast A, Reykowski A, Nittka M, Wald LL. 32-channel 3 Tesla receive-only phased-array head coil with soccer-ball element geometry. Magn Reson Med 2006;56(1):216-223.

76. Tropp J. Image brightening in samples of high dielectric constant. J Magn Reson 2004;167(1):12-24.

77. Van de Moortele PF, Akgun C, Adriany G, Moeller S, Ritter J, Collins CM, Smith MB, Vaughan JT, Ugurbil K. B(1) destructive interferences and spatial phase patterns at 7 T with a head transceiver array coil. Magn Reson Med 2005;54(6):1503-1518.

78. Kellman P, McVeigh ER. Image reconstruction in SNR units: a general method for SNR measurement. Magn Reson Med 2005;54(6):1439-1447.

79. Henkelman RM. Measurement of signal intensities in the presence of noise in MR images. Med Phys 1985;12(2):232-233.

80. Constantinides CD, Atalar E, McVeigh ER. Signal-to-noise measurements in magnitude images from NMR phased arrays. Magn Reson Med 1997;38(5):852-857.

81. Gudbjartsson H, Patz S. The Rician distribution of noisy MRI data. Magn Reson Med 1995;34(6):910-914.

82. Miller CKS, Daywitt WC, Arthur MG. Noise standards, measurements, and receiver noise definitions. Proceedings of the IEEE 1967;55(6):865-877.

83. Yau D, Crozier S. A genetic algorithm/method of moments approach to the optimization of an RF coil for MRI applications - theoretical considerations. Progress in Electromagnetics Research (PIER) 2003;39:177-192.

84. Matschl V, Reykowski A, Jahns K, Hergt M, Fischer H. 48 channel body/spine matrix coils for 3 Tesla. Proceedings of the 13th Annual Meeting ISMRM, Miami Beach, USA. 2005; p 952.

85. Jin J, Chen J. On the SAR and field inhomogeneity of birdcage coils loaded with the human head. Magn Reson Med 1997;38(6):953-963.

86. Alsop DC, Connick TJ, Mizsei G. A spiral volume coil for improved RF field homogeneity at high static magnetic field strength. Magn Reson Med 1998;40(1):49-54.

87. Kangarlu A, Ibrahim TS, Shellock FG. Effects of coil dimensions and field polarization on RF heating inside a head phantom. Magn Reson Imaging 2005;23(1):53-60.

88. Ibrahim TS, Lee R, Baertlein BA, Abduljalil AM, Zhu H, Robitaille PM. Effect of RF coil excitation on field inhomogeneity at ultra high fields: a field optimized TEM resonator. Magn Reson Imaging 2001;19(10):1339-1347.

89. Mao W, Smith MB, Collins CM. Exploring the limits of RF shimming for high-field MRI of the human head. Magn Reson Med 2006;56(4):918-922.

90. Van den Berg CA, van den Bergen B, Van de Kamer JB, Raaymakers BW, Kroeze H, Bartels LW, Lagendijk JJ. Simultaneous B1 + homogenization and specific absorption rate hotspot suppression using a magnetic resonance phased array transmit coil. Magn Reson Med 2007;57(3):577-586.

91. Hennig J, Weigel M, Scheffler K. Multiecho sequences with variable refocusing flip angles: optimization of signal behavior using smooth transitions between pseudo steady states (TRAPS). Magn Reson Med 2003;49(3):527-535.

92. Hargreaves BA, Cunningham CH, Nishimura DG, Conolly SM. Variable-rate selective excitation for rapid MRI sequences. Magn Reson Med 2004;52(3):590-597.

93. Hennig J, Scheffler K. Hyperechoes. Magn Reson Med 2001;46(1):6-12.

94. Thesen S, Krueger G, Mueller E. Compensation of dielectric resonance effects by means of composite excitation pulses. Proceedings of the 11th Annual Meeting ISMRM, Toronto, Canada. 2003; p 715.

95. Collins CM, Wang Z, Mao W, Fang J, Liu W, Smith MB. Array-optimized composite pulse for excellent whole-brain homogeneity in high-field MRI. Magn Reson Med 2007;57(3):470-474.

96. Pauly J, Nishimura DG, Macovski A. A k-space analysis of small-tip-angle excitation. J Magn Reson 1989;81:43-56.

97. Saekho S, Yip CY, Noll DC, Boada FE, Stenger VA. Fast-kz three-dimensional tailored radiofrequency pulse for reduced B1 inhomogeneity. Magn Reson Med 2006;55(4):719-724.

98. Setsompop K, Wald LL, Alagappan V, Gagoski B, Hebrank F, Fontius U, Schmitt F, Adalsteinsson E. Parallel RF transmission with eight channels at 3 Tesla. Magn Reson Med 2006;56(5):1163-1171.

99. Keltner JR, Carlson JW, Roos MS, Wong ST, Wong TL, Budinger TF. Electromagnetic fields of surface coil in vivo NMR at high frequencies. Magn Reson Med 1991;22(2):467-480.

100. Wiesinger F. Parallel magnetic resonance imaging: potential and limitations at high fields. Ph. D. Thesis. Zurich: Swiss Federal Institute of Technology; 2005.

101. Collins CM, Smith MB. Signal-to-noise ratio and absorbed power as functions of main magnetic field strength, and definition of "90 degrees " RF pulse for the head in the birdcage coil. Magn Reson Med 2001;45(4):684-691.

102. Ibrahim TS, Tang L. Insight into RF power requirements and B1 field homogeneity for human MRI via rigorous FDTD approach. J Magn Reson Imaging 2007;25(6):1235-1247.

103. Vaughan JT, Garwood M, Collins CM, Liu W, DelaBarre L, Adriany G, Andersen P, Merkle H, Goebel R, Smith MB, Ugurbil K. 7T vs. 4T: RF power, homogeneity, and signal-to-noise comparison in head images. Magn Reson Med 2001;46(1):24-30.

104. Zhang Z, Yip CY, Grissom W, Noll DC, Boada FE, Stenger VA. Reduction of transmitter B1 inhomogeneity with transmit SENSE slice-select pulses. Magn Reson Med 2007;57(5):842-847.

105. Setsompop K, Wald LL, Alagappan V, Gagoski BA, Adalsteinsson E. Magnitude least squares optimization for parallel radio frequency excitation design demonstrated at 7 Tesla with eight channels. Magn Reson Med 2008;59(4):908-915.

106. Ohliger MA, Ledden P, McKenzie CA, Sodickson DK. Effects of inductive coupling on parallel MR image reconstructions. Magn Reson Med 2004;52(3):628-639.

107. Collins CM, Smith MB. Calculations of B(1) distribution, SNR, and SAR for a surface coil adjacent to an anatomically-accurate human body model. Magn Reson Med 2001;45(4):692-699.

108. Ibrahim TS, Mitchell C, Schmalbrock P, Lee R, Chakeres DW. Electromagnetic perspective on the operation of RF coils at 1.5-11.7 Tesla. Magn Reson Med 2005;54(3):683-690.

109. Lattanzi R, Grant AK, Sodickson DK, Zhu Y. Electrodynamic constraints on minimum SAR in parallel excitation. Proceedings of the 15th Annual Meeting ISMRM, Berlin, Germany. 2007; p 675.

110. Schnell W, Renz W, Vester M, Ermert H. Ultimate signal-to-noise-ratio of surface and body antennas for magnetic resonance imaging. IEEE Transactions on Antennas and Propagation 2000;48(3):418-428.

111. Lattanzi R, Grant AK, Sodickson DK. Approaching ultimate SNR and ideal current patterns with finite surface coil arrays on a dielectric cylinder. Proceedings of the 16th Annual Meeting ISMRM, Toronto, Canada. 2008; p 1074.

112. Lattanzi R, Sodickson DK, Grant AK, Zhu Y. Electrodynamic constraints on homogeneity and RF power deposition in multiple coil excitations. Proceedings of the 16th Annual Meeting ISMRM, Toronto, Canada. 2008; p 614.

113. Vesselle H, Collin RE. The signal-to-noise ratio of nuclear magnetic resonance surfacecoils and application to a lossy dielectric cylinder model. I. Theory. IEEE Trans Biomed Eng 1995;42(5):497-506.

114. Rose ME. Elementary Theory of Angular Momentum: J. Wiley and Sons; 1963.